New Approximations in Vibroimpact Problems

by

Arindam Bhattacharjee

DEPARTMENT OF MECHANICAL ENGINEERING

INDIAN INSTITUTE OF TECHNOLOGY KANPUR

August 23, 2019

New Approximations in Vibroimpact Problems

A Thesis Submitted
in Partial Fulfillment of the Requirements
for the Degree of

DOCTOR OF PHILOSOPHY

by

Arindam Bhattacharjee

DEPARTMENT OF MECHANICAL ENGINEERING
INDIAN INSTITUTE OF TECHNOLOGY KANPUR

August 23, 2019

Declaration

This is to certify that the thesis titled "New Approximations in Vibroimpact Problems" has been authored by me. It presents the research conducted by me under the supervision of Prof. Anindya Chatterjee. To the best of my knowledge, it is an original work, both in terms of research content and narrative, and has not been submitted elsewhere, in part or in full, for a degree. Further, due credit has been attributed to the relevant state-of-the-art and collaborations (if any) with appropriate citations and acknowledgements, in line with established norms and practices.

Signature Arindam Bhattacharjee

Name Arindam Bhattacharjee

Programme: PhD
Department: Mechanical Engineering
Indian Institute of Technology Kanpur
Kanpur 208016

August 2019

Certificate

It is certified that the work contained in the thesis titled "**New Approximations in Vibroimpact Problems**" by Arindam Bhattacharjee has been carried out under my supervision and that this work has not been submitted elsewhere for a degree.

Anindya Chatterjee

Dr. Anindya Chatterjee
Professor
Department of Mechanical Engineering
Indian Institute of Technology Kanpur
Kanpur - 208 016

August 2019

SYNOPSIS

This thesis studies collisions between a compact body and a slender flexible body. In such collisions, the multiple, intermittent, vibration-induced subimpacts at a single contact location result in a complex overall contact interaction and complicated system dynamics. We model approximately a few aspects thereof, using new approaches developed herein.

In the first problem studied in this thesis, we study impact of a Hertzian ball on an *infinitely* long Euler-Bernoulli beam, an idealized problem in wave-dominated impacts. The system equations of motion are nonlinear and include a fractional derivative. A single dimensionless number characterizes the complete contact behavior, which varies from single contact with separation, to multiple contacts with eventual sustained contact, to a single sustained contact. A detailed numerical description of the full range of contact behaviors is given. Further, we present a semi-analytical solution valid until the first separation, and a separate asymptotic solution for the ball's large-time motion in the sustained contact regime.

We subsequently consider collisions involving a *finite*-length Euler-Bernoulli beam, wherein modal expansion can be used to represent the beam's response. We study finite-beam impacts from both detailed simulation and approximate modeling viewpoints.

In the second problem studied in this thesis, we consider impact of a Hertzian ball on a finite beam. We study the interplay between dissipation and modal truncation in convergence of the net restitution or the impactor's (ball's) rebound velocity. A modal expansion for the beam response and a force-compression constitutive relation for the contact results in a system of ODEs, which we numerically solve. We observe that with subimpacts, and Hertzian contact, many modes are needed before convergence occurs; that including contact dissipation, either viscous or hysteretic, has only a slight effect; and that a little modal damping speeds up convergence of the net restitution value.

Following the above study of convergence with small modal damping, we find numerically the restitution values and the number of subimpacts for ball-beam impacts as above, with different ball masses, different contact locations, and four different beams. The impact-contact interaction is rich. A few qualitative trends are seen in the restitution, which we subsequently attempt to approximate using a simpler algebraic net-impulse model.

In an algebraic or net-impulse approach to impact modeling, we map pre-impact states to post-impact states without solving differential equations. Such an approach is seldom used for vibroimpacts with subimpacts. The main contribution of this thesis is a new quadratic program based approach to model restitution in such vibroimpact problems. In the new approach, we minimize post-impact kinetic energy subject to the basic linear inequalities that govern contact, like nonnegative normal impulse and non-interpenetration of bodies, along with a crucial "outward" or rebound-enhancing inequality. We refer to this approach as Energy Minimization under Outward Constraints (EMOC). Impossibilities like interpenetration or kinetic energy increases are never predicted by the EMOC approach. A good choice of an outward inequality is a key requirement of the approach. Such a choice for vibroimpact problems is proposed, which incorporates modal information, impactor mass, and contact location.

For validation purposes, we apply and fit the EMOC approach to the earlier numerically obtained restitution values for balls hitting the different beams. We obtain good results with a small number of fitted parameters. Subsequently, the experimentally obtained outcomes of bars dropped on an immovable surface at different angles of inclination, as reported by Stoianovici and Hurmuzlu (in 1996), are also modeled using the EMOC approach. The match obtained for both the cases shows that the EMOC approach is potentially useful for rapid or large-scale simulation with reasonable accuracy and without unduly heavy computational load. No comparable modeling approach exists in the vibroimpact literature.

ACKNOWLEDGEMENTS

I express here my sincere gratitude to my advisor Dr. A. Chatterjee for his help, numerous discussions, encouragement and teaching over a long period encompassing my masters and PhD study. I am indebted to him for assisting and enabling me to explore and study diverse technical disciplines and skills, and in sufficient depth. I am thankful for the fruitful learning experience I had under his guidance as well as the more direct contributions of time, research ideas and his involvement in writing papers. I owe him thanks for helping me better understand many aspects in solid body collisions and rate-independent hysteresis, and mechanics and approximate methods in general.

I am thankful to my thesis committee member Dr. P. Wahi for his useful comments and suggestions. I express my gratitude to my comprehensive committee members, Dr. C. S. Upadhyay and Dr. S. S. Gupta. I thank all my course instructors, and especially Dr. P. M. Dixit and Dr. I. Sharma. I am grateful for the technical help that I received from Dr. A. K. Mohanty at IISc Bangalore, Dr. K. Shah at IISER Bhopal and Dr. S. Rakshit at IIT Madras.

I am thankful to the Government of India for my PhD funding. I also thank IIT Kanpur and my department for travel support to an international conference. I thank all others in the Mechanical Engineering Department whose help I received during my PhD stay.

I express my heartfelt thanks to all my labmates, both PhD and masters students, and all my friends for their support, companionship and all the fun we had during my stay. I thank Nishant Goyal for his hospitality and assistance in Bangalore, Sankalp for discussions and Bidhayak for his help in FEM.

Finally, I want to express my sincere thanks to my parents and sister for their unlimited support throughout my study and my life in general.

Contents

List of Figures

List of Tables

Chapter 1

Introduction

This thesis studies vibration-dominated impacts in solid bodies.

Impacts between solid bodies have been studied extensively in the past; see for example the early classic text by Goldsmith [1], recent books [2, 3, 4], mauscripts and review articles [5, 6, 7].

Impact involves short violent contact between two or more solid bodies. Such interactions excite significant vibrations in many cases. There exists an extensive body of literature on collisions and their modeling, involving both rigid bodies [3, 8, 9, 10, 11] and flexible bodies [6, 12, 13, 14]. There are many articles that study the more complex phenomenon of simultaneous and multiple impacts, e.g., [15, 16, 17, 18, 19], though impact-induced vibrations are not explicitly modeled therein.

Impulsive impact interactions in solid bodies are complicated. In the literature on vibration-dominated impact, aspects focused on have included waves and vibrations [20, 21, 22, 23, 24], energy losses through viscous dissipation [25, 26, 27] and plastic deformation [23, 28], the related idea of a coefficient of restitution [6, 14, 29], contact detection (in experiments and in numerical soluitons) [19, 30, 31, 32, 33, 34], impact oscillators [35, 36] and some others. In the above, articles [20, 21, 22, 24] include fundamental studies wherein one body has waves that radiate to infinity. In these papers, the effort has been on detailed and accurate modeling of the mechanics. Application of a coefficient of restitution has been discussed in the context of simulations in [6, 37, 38], and the equivalence of such a restitution model with a local contact-dissipation model has been studied in [13]. Articles [19, 30, 31] report experimental studies that have helped establish the complexity of multiple contacts at a given location, through contact detection.

Generally speaking, impact modeling can be categorized broadly into incremental and algebraic formulations. Incremental models solve evolution equations, while algebraic models directly map pre-impact to predicted post-impact states. These two categories, incremental and algebraic, are sometimes called continuous and instantaneous respectively (e.g., [10, 39]); or compliant and rigid respectively [40]. Some authors distinguish between locally deformable or penetrable bodies, versus "truly" rigid bodies [41], with the same modeling implications.

In incremental models, differential equations are used to describe the evolving dynamics of the system *during* contact. The deformation may be modeled in detail, using either ODEs or PDEs. Such treatments include models based on the finite element method (e.g. [32, 39]), or with modal expansions for one or more colliding bodies (e.g., early but limited treatments in [1] and a more detailed computational study in [42]). Such deformation-based models may also be simplified using the assumption that the colliding bodies are essentially rigid, with contact being mediated by a localized, massless, and possibly nonlinear as well as dissipative compliance (e.g., [25, 28, 43, 44, 45]). A final class of incremental models changes the independent variable from time to accumulated normal impulse, and solves differential equations governing the evolution of velocities in the colliding bodies (e.g., see the classical treatment in [46], and also [17, 47, 48, 49]). Compliant contact models are suitable for longer-time global dynamics [50] or contact events with somewhat longer durations [51]. We also note that compliant contact models seem suitable for examining the transmission of impulsive loads in linkages with clearances [52].

In contrast to incremental models, in algebraic or net-impulse models only pre- and post-impact velocities along with the contact impulse(s) are considered and temporal details are not simulated: see e.g., [2, 18, 40, 53, 54, 55]. Algebraic models are simpler, quicker, comparatively inaccurate, and sometimes aim only to predict some useful quantities while avoiding impossibilities and physically non-intuitive outcomes.

The rest of this thesis is organized as follows. The description below also presents the specific problems studied here, and briefly highlights new results and contributions.

In chapter 2, we study impact of a Hertzian ball on an *infinitely* long Euler-Bernoulli beam. The impact interaction obeys two nonlinear differential equations with a fractional order derivative. The contact dynamics exhibits multiple behavior regimes that are completely characterized by a single dimensionless parameter. Apart from detailed numerical results characterizing the complete system, we provide new approximate solutions for two regimes of the various contact behaviors. The work presented in this chapter has been published in [24].

Subsequently we consider impacts involving a *finite* beam, where a modal expansion solution can be attempted. In chapter 3, we numerically study impact between ball and a simply-supported beam. We present a systematic study of the convergence of the ball's rebound velocity, or net restitution, with the number of beam modes retained and with various dissipation mechanisms. With pure Hertzian contact (no dissipation) and with contact dissipation, the convergence is rather slow. However, light modal damping regularizes the interaction and convergence of restitution is achieved with relatively fewer modes. The work presented in this chapter has been published in [56].

In chapter 4, we compute restitution values for impacts of balls on different beams, for different impactor masses and impact locations. A few qualitative trends in the variation of the restitution are observed. The detailed results of chapter 4 motivate our novel modeling effort of the next three chapters.

Chapters 5 through 7 present the main academic contribution of this thesis, namely, a new quadratic program based net-impulse model for restitution outcomes in vibration-dominated impacts. The model greatly extends the work in [18], wherein simultaneous impacts in rigid bodies was modeled, with no accounting of vibrations. In chapter 5, we present relevant background related to algebraic modeling of collisions which leads to the quadratic program approach. Chapter 6 presents the modeling approach, which we call Energy Minimization under Outward Constraints (EMOC). In brief, the model minimizes post-impact kinetic energy of the system subject to new "outward" or rebound enhancing linear inequalities together with other basic constraints (e.g., nonnegative normal impulse and nonnegative post-impact normal velocities). Physical impossibilities are never predicted. The model has three free parameters. The outward constraint is the key innovation of this approach.

The proposed outward inequality incorporates modal information, impactor mass, and contact location. Chapter 7 presents a parameterization of the model, and the match against the numerically obtained restitution values from chapter 4. A reasonably good match is seen over a range of ball masses and impact locations. It is emphasized that the new approach is algebraic, i.e. it does not involve solution of ODEs and is comparatively much quicker.

Chapter 8 applies the EMOC model to a completely different problem, namely the experimentally obtained restitution values for tilted rods dropped on immovable surface, as presented in [19]. The EMOC model works for this system when the axial modes are *not* included in the falling rod's dynamics, and only bending modes are retained. The reason is uncovered and explained. Overall, with bending modes, a good match is obtained, again with no ODE solution.

Chapter 9 presents some final discussion and concludes the thesis.

Chapter 2

Transverse impact of a Hertzian body on an infinite beam

The work presented in this thesis begins with a study of the transverse impact of a Hertzian body (a ball) with an *infinitely* long initially stationary Euler-Bernoulli beam. The material in this chapter has been published in [24].

2.1 Introduction

Impact between a compact body and an *infinitely* large slender body constitutes a special limiting case, provides insights into observed behavior even for impacts with large but finite-sized objects, and presents an academic problem that is interesting in its own right. This chapter presents a study of such an impact.

A particular problem of historical interest within this category is the impact of a Hertzian sphere with a large thin *plate*, which is analytically simpler than impact with a beam. Raman [57] carried out experiments for a sphere striking an extended thin plate, while Zener [22] did the analysis assuming an infinite plate and obtained a good match with Raman's experiments. Zener showed that the impulse response of a point on an infinite plate is $y = P\alpha$, where y is the displacement of the point where an instantaneous impulse P acts, and α is a constant dependent on plate parameters. This impulse response, $y = P\alpha$, is

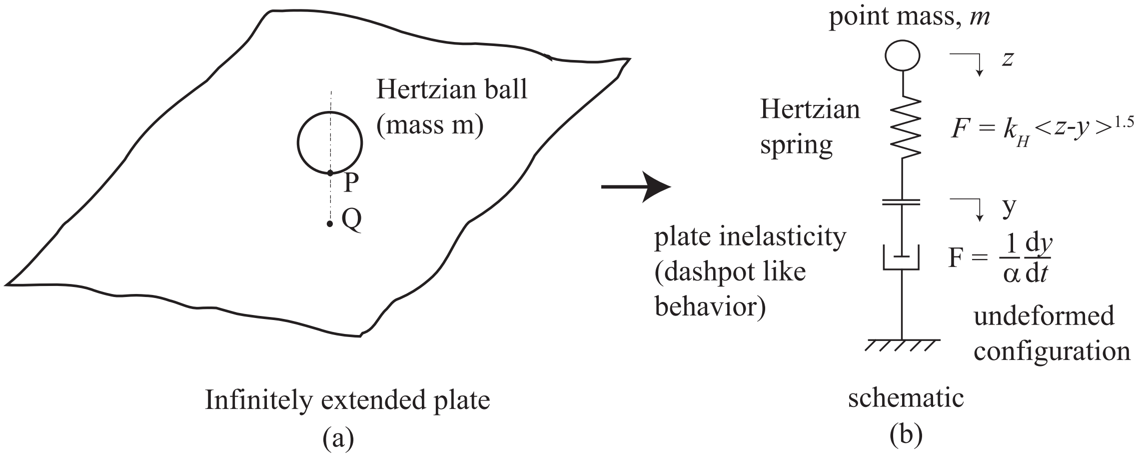

Figure 2.1: (a) A Hertzian sphere striking a thin infinite plate, and (b) its dynamic equivalent. The impulse response of the plate is a constant, same as that for a dashpot; y and z denote the displacements of the plate's contact point and the sphere's center respectively.

coincidentally the same as that of a single dashpot. Thus, the lateral impact of a Hertzian sphere with a large plate is mathematically the same as that of a point mass falling on a dashpot with a mediating Hertzian spring in between (see Fig. 2.1).

In this chapter we consider impact between a compact Hertzian object and an infinite beam, which is more complicated than the contact between a ball and plate, as mentioned above. Schwieger [58], following [1, 59], noted that elastic central impact behavior on a sufficiently long beam is independent of both the beam's boundary conditions as well as its length. Along the lines of Zener [22], Schwieger [58, 60] then obtained the relation for the short-time deflection of a finitely long Euler-Bernoulli beam under impact loading (an approximate solution); an extra factor of 2 was corrected in the later paper. The same impulse response function for an infinite beam (an exact solution) was obtained in [61, 62] using the Fourier transform, and in [63, 64] directly in the time domain. The key point is that a beam's impulse response is proportional to $\sqrt{t}$. Schwieger [58] also presented some experiments with single contact phases.

More recently, Yigit & Christoforou [23] presented a general numerical study of the impact of a mass on a composite beam and plate with a *linearized* contact stiffness. These authors proposed two nondimensional numbers using which the overall contact behavior might be characterized into different regimes, identifying single contact at two extremes, with passing remarks on the intermediate regime where multiple impact events are possible.

2.2 Problem formulation and initial simulations

In this chapter, we present significant progress beyond [23, 58, 60]. In particular, we present a detailed study of the lateral impact of a compact Hertzian body with an infinitely long Euler-Bernoulli beam, characterizing the full range of possible contact dynamic behaviors, from impacts with a single contact phase followed by separation, through impacts with more than one contact phase followed by sustained contact, to impacts with no separation at all.

We now turn to equations of motion.

2.2.1 Equations of motion

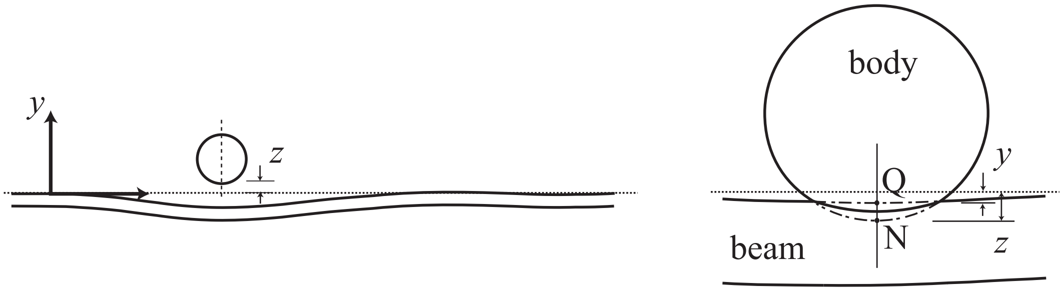

Figure 2.2: (a) Transverse impact of a compact body on an infinite Euler-Bernoulli beam. The displacement of the beam and the body are referred to as $y(t)$ and $z(t)$ respectively. (b) The body-beam contact. The solid lines show the actual configuration at contact. N is the notional contact point on the undeformed body. Q is the notional contact point on the beam. The distance from N to Q is the compression (positive in the sense shown); and a contact force exists when the compression is positive.

The equations we use are similar to those in [58, 60].

See Fig. 2.2. A solid body of mass m strikes a horizontal initially stationary beam. Hertz contact is assumed. The beam has uniform mass per unit length $\overline{m}$ and flexural rigidity EI. The displacement (upwards) of the beam's contact point is taken as $y(t)$. The distance (upwards) of the notional point of contact of the body from the beam's notional undeformed surface is taken as $z(t)$ (see Fig. 2.2). The body strikes the beam with a velocity of $\dot{z}_0 < 0$. The body has negligible internal vibration. Gravity is neglected.

The displacement (y) of the point on an initially stationary infinite beam where an instantaneous impulse (P) acts at time $t = 0$ is given by

$$y = P\overline{C}\sqrt{t}, \tag{2.1}$$

where

$$\overline{C} = \frac{[EI]^{-1/4}[\overline{m}]^{-3/4}}{\sqrt{2\pi}}, \tag{2.2}$$

where in turn EI and $\overline{m}$ denote the flexural rigidity and the mass per unit length of the beam respectively (see [63, 64]). Using the above impulse response, it is easy to show that the motion of the beam's contact point obeys the equation[1]

$$\mathrm{D}^{\frac{3}{2}} y = -\overline{C}\,\Gamma\left(\tfrac{3}{2}\right) f, \tag{2.3}$$

where $\mathrm{D}^{\frac{3}{2}}$ represents a fractional order derivative (see also Appendix A.1), $\Gamma(1.5) = \dfrac{\sqrt{\pi}}{2}$, and f is the time varying contact force. Also, $y(0) = 0$, and $\dot{y}(0) = 0$. Simultaneously, the motion of the impacting body obeys

$$m\ddot{z} = f. \tag{2.4}$$

It remains to specify f. Let ξ be the local compression at the contact location (see Fig. 2.2(b)), i.e., $\xi = y - z$. Then, for Hertzian contact,

$$f = k_H \left\langle \xi \right\rangle^{\frac{3}{2}}, \tag{2.5}$$

---

[1] Assume zero initial conditions. The Laplace transform of Eq. (2.1) with $P = 1$ (unit impulse) gives the impulse response function $Y(s) = \overline{C}\dfrac{\Gamma(\frac{3}{2})}{s^{\frac{3}{2}}}$. With a continuous downward acting contact force $-f(t)$ on the beam, we have $Y(s) = -\dfrac{\overline{C}\,\Gamma(\frac{3}{2})}{s^{\frac{3}{2}}}F(s)$, where $F(s)$ is the Laplace transform of $f(t)$, which is the Laplace transform of Eq. (2.3).

where the angle brackets denote

$$\langle \xi \rangle = \begin{cases} \xi & \xi \geq 0, \\ 0 & \xi < 0, \end{cases} \tag{2.6}$$

and k_H is the Hertz contact stiffness.

For contact between two spheres having the same radius R and of the same material (Young's modulus E and Poisson's ratio ν), $k_H = \dfrac{\sqrt{2}E\sqrt{R}}{3\,(1-\nu^2)}$ (see [65]). In our case, taking the upper surface of the beam to be flat and the local radius of the impacting body to be R, and considering the body and the beam to be of the same material, we have $k_H = \dfrac{2E\sqrt{R}}{3\,(1-\nu^2)}$. However, we treat k_H as a free parameter because mass is a global property of the impacting body while k_H is a local property[2].

Note also that the general f of Eqs. (2.3) and (2.4) has been replaced with an explicit function of ξ in Eq. (2.5). Thus,

$$\begin{aligned} \mathrm{D}^{\frac{3}{2}} y &= -\overline{C}\,\Gamma(\tfrac{3}{2}) k_H \langle \xi \rangle^{\frac{3}{2}}, \\ m\ddot{z} &= k_H \langle \xi \rangle^{\frac{3}{2}}, \qquad y(0) = 0,\ \dot{y} = 0,\ z(0) = z,\ \dot{z}(0) = -v. \end{aligned} \tag{2.7}$$

Thus, Eqs. (2.7) together govern the motion for the body and the beam's contact point.

2.2.2 Nondimensionalization

Equations (2.7) involve four dimensional parameters, namely $\overline{C}$, k_H, m and v, where $v = -\dot{z}_0$ (impact velocity). The system behavior therefore depends on one non-dimensional number, S, which we choose to be

$$S = \overline{C}^{10} k_H^2 m^8 v. \tag{2.8}$$

---

[2] For a hemispherical impactor instead of a spherical one, k_H would remain the same while the mass would be halved. Localized changes in curvature can change k_H without changing the mass.

S governs separations versus sustained contact regimes. It governs contact dynamics, not severity of contact stresses. The possibility of plastic yielding upon severe impact needs separate analysis, not considered here. Both large and small S are possible for stress-wise gentle impacts (see Table 2.1). The nondimensional number λ used in [58] is $S^{\frac{1}{10}}$, but we prefer Eq. (2.8) because it is proportional to velocity.

For simple conversion and comparison of dimensional versus nondimensional results, we define the following dimensional groups of parameters:

$$\text{units of time}: \quad \hat{T} = \overline{C}^2 m^2, \tag{2.9}$$

$$\text{units of force}: \quad \hat{F} = \frac{v}{\overline{C}^2 m}, \tag{2.10}$$

$$\text{units of length}: \quad \hat{D} = \left(\frac{\hat{F}}{k_H}\right)^{\frac{2}{3}}. \tag{2.11}$$

The above three quantities, namely $\hat{T}$, $\hat{F}$ and $\hat{D}$ will be used to scale dimensional quantities. Other physical quantities for similar scaling purposes will be defined in terms of Eqs. (2.9) through (2.11). For example, we will use

$$\text{units of velocity}: \quad \hat{V} = \frac{\hat{D}}{\hat{T}}, \tag{2.12}$$

$$\text{units of mass}: \quad \hat{M} = \frac{\hat{T}^2 \hat{F}}{\hat{D}}, \tag{2.13}$$

and so on.

Now it will be possible to compare two different dimensional calculations with the same S as follows. In the first calculation, suppose a parameter set consisting of $\overline{C}_1$, k_{H_1}, m_1 and v_1 is used to compute a force f_1 at some time t_1. In the second calculation, suppose $\overline{C}_2$, k_{H_2}, m_2 and v_2 are used to compute a force f_2 at some time t_2. It is crucial that

$$S_1 = \overline{C}_1^{10} k_{H_1}^2 m_1^8 v_1 = \overline{C}_2^{10} k_{H_2}^2 m_2^8 v_2 = S_2.$$

The dimensional quantities of Eqs. (2.9) through (2.13) need not have the same numerical values for the two calculations. In other words, to compare f_1 at time t_1 against f_2 at time t_2, we allow the force and time quantities

$$\frac{v_1}{\overline{C}_1^2 m_1} \neq \frac{v_2}{\overline{C}_2^2 m_2}, \text{ i.e., } \hat{F}_1 \neq \hat{F}_2$$

and

$$\overline{C}_1^2 m_1^2 \neq \overline{C}_2^2 m_2^2, \text{ i.e., } \hat{T}_1 \neq \hat{T}_2$$

in general. Nevertheless, since $S_1 = S_2$, we are assured that

$$\text{if} \quad \frac{t_1}{\hat{T}_1} = \frac{t_2}{\hat{T}_2} = t_{\text{nd}}, \quad \text{then} \quad \frac{f_1}{\hat{F}_1} = \frac{f_2}{\hat{F}_2} = f_{\text{nd}}.$$

In other words, the variation of $f/\hat{F}$ against $t/\hat{T}$ depends on S but not on individual parameter values. The "nd" subscripts denote nondimensional quantities. A numerical example is given, for completeness, in Appendix A.2.

The above method of using dimensional analysis helps us to use a simplifying trick. In some calculations that are in principle *dimensional*, we may choose numerical parameters such that relevant quantities from among Eqs. (2.9) through (2.11) have convenient numerical values, such as unity, even with S being simultaneously assigned any desired value, so that the *nondimensionalized* quantities of interest have the same numerical values as the dimensional quantities[3]. We will use this trick a few times in this chapter, and point it out when we do so. There is no physical insight lost, and the presentation becomes slightly simpler if we use this approach.

2.2.3 Range of physical parameters

A few examples to indicate the physical range of system parameters may be helpful.

For simplicity we assume a steel sphere of radius R striking a steel beam of square cross section $b \times b$. For steel, we assume Young's modulus $E = 200$ GPa, Poisson's ratio $\nu = 0.3$

---

[3] Assigning S implies one equation. Assigning specific values to Eqs. (2.9) through (2.11) gives three more equations. Taking logarithms, we solve 4 linear equations to obtain 4 parameter values.

and density $\rho = 7800$ kg/m^2. Some examples are given in Table 2.1.

The last two rows show that large or small S does not necessarily indicate large or small stresses, respectively. Severity of stresses would have to be checked in other dimensional calculations if needed. In this chapter we assume that stresses are small enough for the Hertzian contact and elastic beam analyses to hold.

Table 2.1: Representative system parameters. First three columns are in SI units.

b	R	v	S	comment
0.03	0.02	0.2	4.05×10^{-6}	
0.03	0.03	0.1	0.0512	
0.028	0.033	0.5	15.556	
0.02	0.027	0.4	371.05	
0.015	0.04	1.55×10^{-6}	3.54×10^4	large S, small stresses
0.05	0.03	10000	0.0146	small S, large stresses

2.2.4 Numerical solution strategy

We now consider numerical solutions of Eqs. (2.7). Several numerical methods have been proposed for solving fractional order differential equations: see, e.g., [66, 67, 68, 69]. Of these, [69] offers a simple recipe, and we adopt it here (for details, see Appendix A.1).

Some parameter choices may lead to high/low contact forces or very long/short times of contact. Whenever needed, we restate the problem in numerically convenient but physically equivalent terms by changing parameter values while holding S constant. An example are given in Appendix A.2.

2.2.5 Contributions

The main contribution of this study is a complete characterization of the dynamic contact behavior of the Hertzian-body and infinite-beam system.

To motivate development of the same, we present a few initial numerical simulations to highlight the different regimes of behavior (see Fig. 2.3); detailed solutions will be developed and presented in sections 2.3-2.5. For present purposes, all quantities in Fig. 2.3 can be

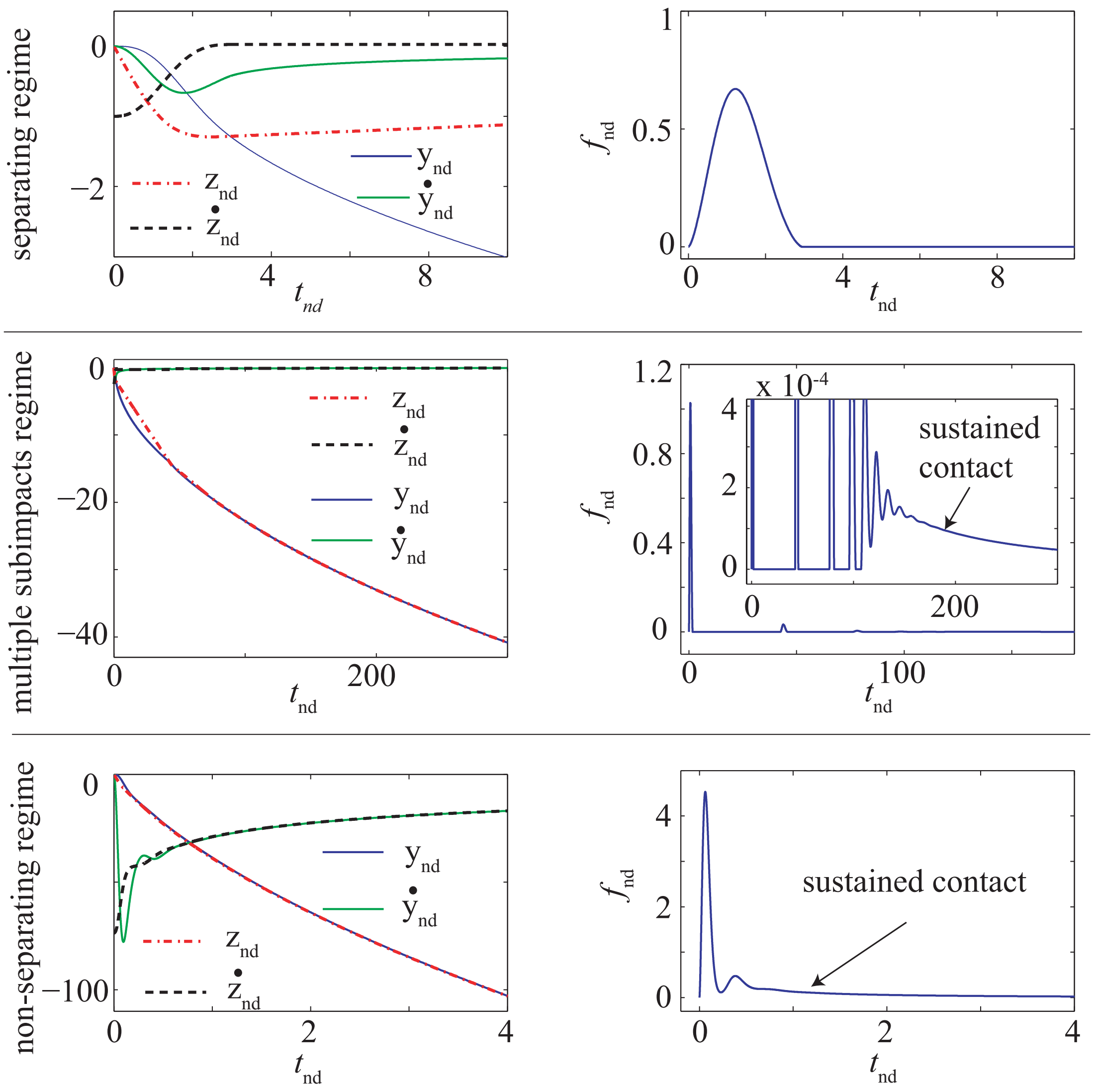

Figure 2.3: Motion variables on the left, contact forces on the right. Examples for low, moderate and high S depicted in the top, middle, and bottom rows respectively. Top: $S = 1$, middle: $S = 15$, bottom: $S = 4 \times 10^5$. All quantities shown are dimensionless, following section 2.2.2.

viewed as nondimensional because, as explained in subsection 2.2.2 above, the relevant quantities of Eqs. (2.9) through (2.11) were chosen to have numerical values of unity while assigning the desired value to S (see footnote 3).

In Fig. 2.3, the left hand-side plots show motion variables, while the right hand-side plots show the corresponding contact forces, both plotted against time. Three qualitatively different regimes are seen for increasing S. In the low S-regime shown in the figure, there

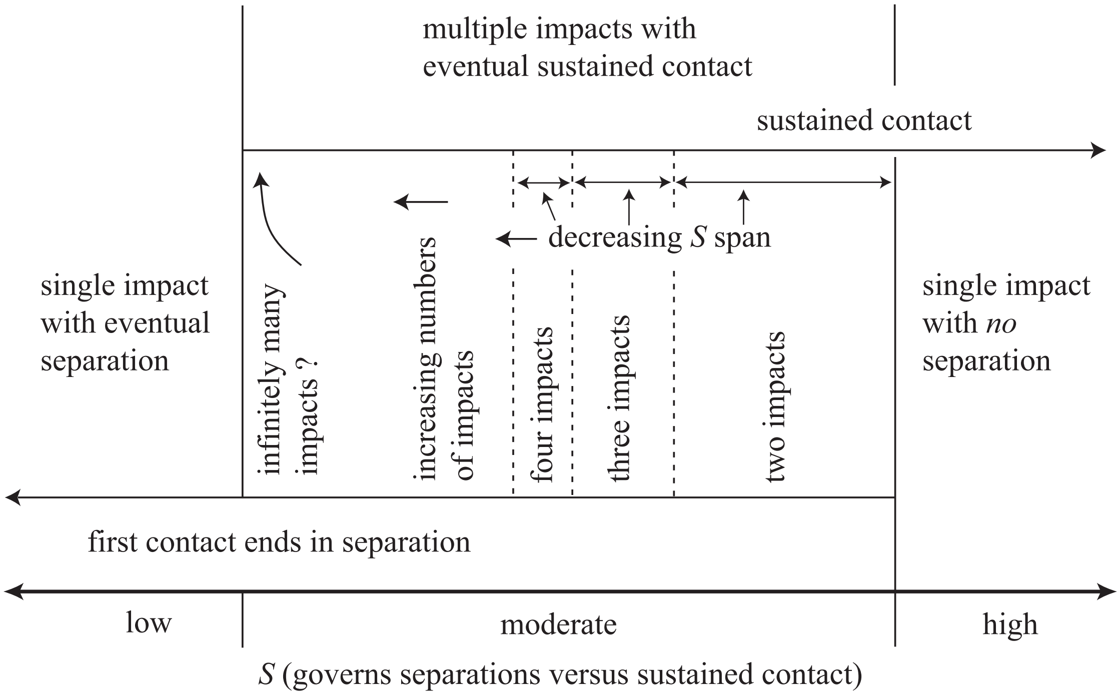

Figure 2.4: Schematic diagram of possible contact behaviors.

is a single contact phase followed by eventual separation. In the moderate S plot, there are four distinct separations before eventual sustained contact. In the high S plot, the body never separates from the beam. During final sustained contact, the contact force f shows decaying oscillations due to the nature of the fractional derivative, and because energy gets carried away from the contact point in the form of waves in the beam, although there is no dissipation in the global system.

A schematic diagram showing the different regimes is given in Fig. 2.4; no such complete picture of the contact dynamics of this system was available before.

The transition from a single contact to infinitely many contacts is due to the neglect of gravity in the impact model. With gravity, every rebounding ball would eventually fall back on the beam, again and again, no matter how high the intervening rebound. Since we ignore gravity, if the rebound velocity of the ball after first impact is *upwards*, then no other contacts occur. However, it is possible for the ball's velocity to be *downwards* at the end of the first contact phase, with the beam's contact point traveling downwards faster than the ball. In such cases, the ball's velocity stays constant while the beam slows down, and another contact phase must unavoidably occur.

With the above motivation, we first develop a semi-analytical solution using a Galerkin procedure, for low to moderate S impacts, valid for the first contact phase. Next, we develop a new asymptotic approximation for the long-term behavior in moderate to high S impacts, wherein the final state is sustained contact. Interestingly, the asymptotic behavior depends on the impact velocity but not on the number of contacts and separations preceding final sustained contact. Finally, we present detailed numerical simulations over a large range of S, and show that the two approximations for the two regimes (S small, and S large) have overlapping ranges of validity.

2.3 Semi-analytical approximation for the first contact phase

We now develop a semi-analytical solution for the body and beam-contact-point's motion during the first contact phase until separation, with the understanding that contact may or may not occur again.

We will present a dimensional calculation for convenience. We will be interested in different amounts of rebound (hence, different restitution values), which will require different S values, and so prior nondimensionalization is not convenient. Instead, because we will use a Galerkin approximation, taking the contact duration uniformly to be equal to unity makes the calculations less clumsy. For this reason, we will tackle the problem as an *inverse problem*, where the dimensional quantities $\overline{C} = 1$, $k_H = 1$, time duration $t_d = 1$, initial impact velocity v is specified, and the impactor mass m is determined as part of the solution.

We emphasize that once the inverse problem is solved, then $\overline{C} = 1$, $k_H = 1$, v (specified) and m (solved for) have all been determined, and subsequently nondimensionalization can proceed along the lines of section 2.2.2 if so desired (see, e.g., Fig. 2.6).

We first expand the contact force f in a series of orthogonal basis functions $\phi_k(t)$, defined for $0 \leq t \leq 1$, as in

$$f = \sum_{1}^{N} a_k \phi_k, \tag{2.14}$$

where the a_k are to be determined. To choose the ϕ_k, we note that the Hertzian force is very small for small compression, and so the contact force does not increase linearly from zero, and does not fall linearly to zero. While a fractional power such as $t^{1.5}$ might seem appealing, for analytical convenience we treat the initial force as t^2 and the force just before separation as $(t_d - t)^2 = (1-t)^2$. In the rest of this section, we will simply write 1 in place of the contact duration t_d.

Accordingly, we begin with

$$\psi_k = t^2(1-t)^2 \cdot t^{k-1}, \quad k = 1, \cdots, N,$$

where we have obtained good results with $N = 6$. We then use Gram-Schmidt orthogonalization in Maple to obtain mutually orthogonal basis functions ϕ_k from ψ_k, given by

$$\begin{aligned}
\phi_1 &= t^2(1-t)^2 \cdot 3\sqrt{70}, && (2.15)\\
\phi_2 &= t^2\,(t-1)^2 \cdot 3\,(2t-1)\,\sqrt{770}, && (2.16)\\
\phi_3 &= t^2\,(t-1)^2 \cdot 3\left(22t^2 - 22t + 5\right)\sqrt{182}, && (2.17)\\
\phi_4 &= t^2\,(t-1)^2 \cdot 3\,(2t-1)\left(26t^2 - 26t + 5\right)\sqrt{770}, && (2.18)\\
\phi_5 &= t^2\,(t-1)^2 \cdot 3\left(130t^4 - 260t^3 + 182t^2 - 52t + 5\right)\sqrt{2618}, && (2.19)\\
\phi_6 &= t^2\,(t-1)^2 \cdot 3\,(2t-1)\left(34t^4 - 68t^3 + 46t^2 - 12t + 1\right)\sqrt{190190}. && (2.20)
\end{aligned}$$

Figure 2.5 plots the above ϕ_is againt time.

The contact force f in Eq. (2.14) is defined using Eqs. (2.15) through (2.20). The displacement of the contact point on the beam, by Eq. (2.1), is (using $\overline{C} = 1$)

$$y = -\int_0^t f(\tau)\sqrt{t-\tau}\,\mathrm{d}\tau. \tag{2.21}$$

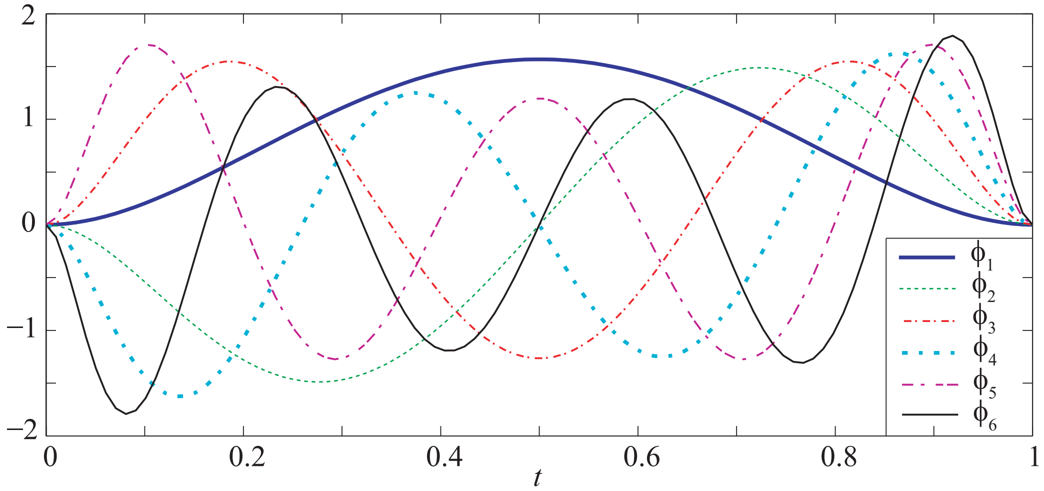

Figure 2.5: The orthogonal basis functions ϕ_i, $i = 1 \ldots 6$.

By Eq. (2.4),

$$\dot{z} = \dot{z}_0 + \frac{1}{m} \int_0^t f(\tau) \mathrm{d}\tau, \tag{2.22}$$

which is then integrated again to obtain z. Note that in Eqs. (2.21) and (2.22), the unknown parameters a_k appear linearly. However, the Hertzian contact spring is nonlinear, and so a residual $r(t)$ is defined as (using $k_H = 1$)

$$r(t) = f^2 - (y - z)^3, \tag{2.23}$$

in which the unknown parameters a_k appear nonlinearly.

In the above, $\dot{z}_0$ is an input; and the parameter m and coefficients a_k are to be solved for. We need $N + 1$ equations. Impending separation defines the first equation,

$$(y - z)|_{t=1} = 0. \tag{2.24}$$

We obtain another N equations by making the residual orthogonal to ϕ_k,

$$\int_0^1 r(t)\, \phi_k \, \mathrm{d}t = 0, \quad k = 1, 2, \cdots, N. \tag{2.25}$$

Equations (2.24) and (2.25) are nonlinear, and must be solved numerically for m and the a_k. These equations also have some unphysical solutions wherein $f < 0$ during the contact interval; we discard such solutions.

In Eq. 2.23, since the contact force f is squared, negative values are in principle allowed in solutions of the system of equations. It may be noted that we never enforced the $f \geq 0$ constraint during numerical solution. In some solutions $f < 0$ values are mathematically obtained but of course these are physically impossible. In numerical simulations, we always plot f, and ensure that $f \geq 0$. Any solution where f turns out to be less than zero is discarded for being non-physical.

However, once we identify the physically valid solution of interest for a gentle impact, we can obtain other solutions by numerical continuation, i.e., increasing $v = -\dot{z}_0$ in small steps and using the previous solution as an initial guess for each new value of $\dot{z}_0$. We have obtained our solutions in this way, using the Newton-Raphson method with numerically estimated Jacobians.

We now present results obtained from this semi-analytical approximation. Although our full numerical solutions will be presented in section 2.5, some numerical results are presented in Fig. 2.6 to show that the semi-analytical approximation and full numerics agree essentially completely, validating both.

An aspect of Fig. 2.6(b) should now be discussed. This issue was briefly mentioned in section 2.2.5 as well.

At the end of the first contact phase, the impacting body has some velocity v_f (measured positive upwards). The impact had occurred with an approach velocity v (measured positive downward). The nondimensional ratio $\frac{v_f}{v}$ is a function of S alone. In the first contact phase, a net impulse has acted on the beam, whose contact point keeps moving downwards, proportionally to $\sqrt{t}$ for large t. The impactor's post-impact displacement is like $v_f t$ for large t (because gravity is ignored). It follows that $v_f \geq 0$ implies no subsequent contacts; while $v_f < 0$ implies a subsequent contact, possibly after a very long time as $v_f \to 0^-$, because $t \gg \sqrt{t}$ for large t. In other words, the transition from a single contact to more

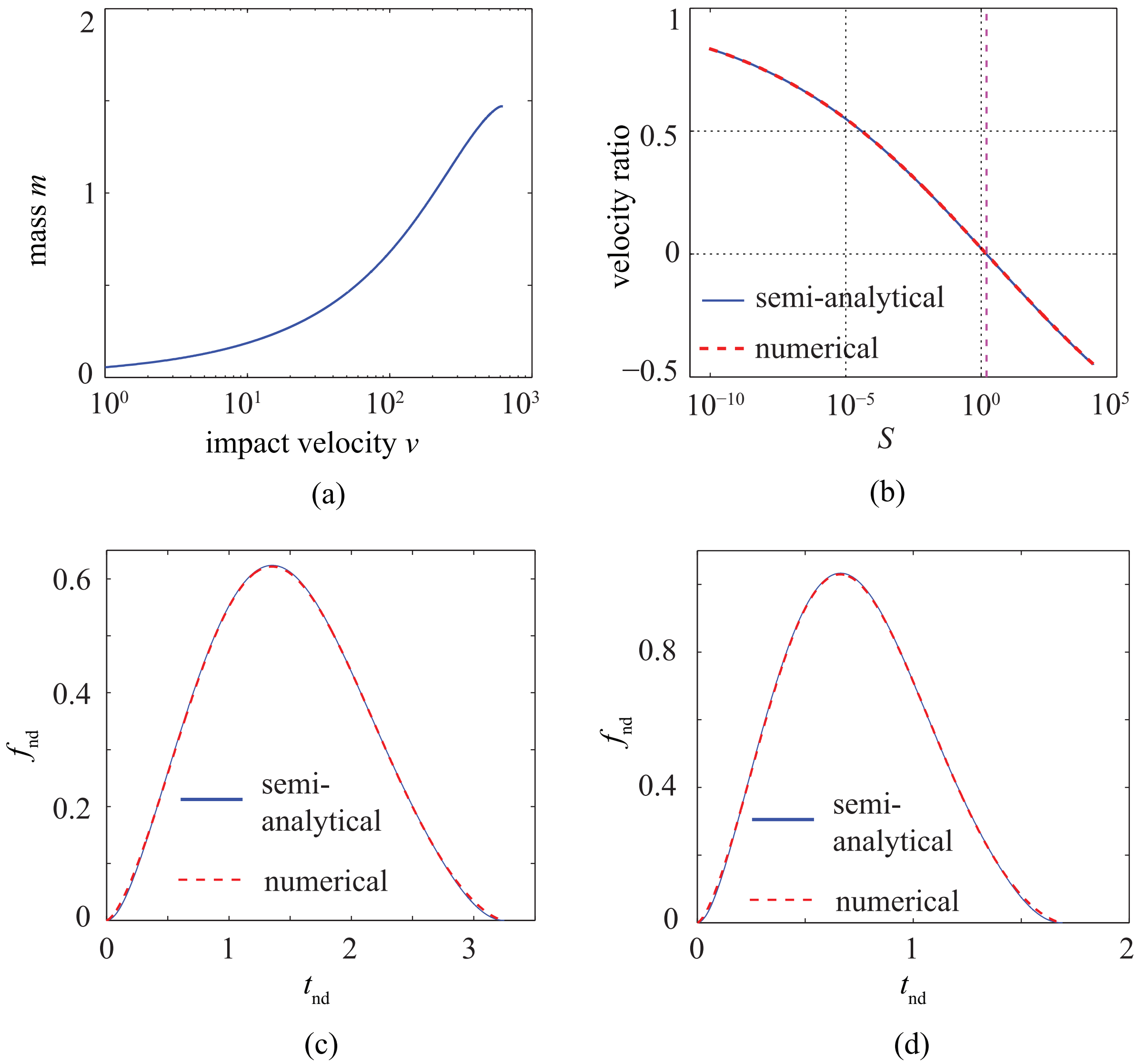

Figure 2.6: Approximate solution for the first contact phase. $\overline{C} = 1$, $k_H = 1$ in all cases. (a) Approximated m against specified v. (b) Ratio of impactor velocity at separation to initial velocity v against S. Two near-identical solutions are shown: one is the semi-analytical approximation, and one is the full numerical solution with the obtained value of m. For even larger S, the approximation eventually deteriorates. Contact force against time is plotted for two cases in the next two subplots: (c) $v = 70$, $m = 0.555$ and (d) $v = 125$, $m = 0.769$. Each subplot, (c) and (d), contains two near-identical nondimensionalized solutions: one semi-analytical and one full-numerical with the same S.

than one contact occurs with the second contact occurring after an infinite time. We observe for future reference that this transition point, i.e., $\dfrac{v_f}{v} = 0$ is at $S \approx 1.56$. As $S \to 1.56^+$, the time interval between subsequent impacts increases without bounded.

By direct observation of the match with full numerics in Fig. 2.6(b), we conclude that the semi-analytical approximation with $N = 6$ is good for $0 < S \lesssim 1.2 \times 10^4$.

We now turn to an asymptotic description of the long-time behavior of the system during final sustained contact, which occurs for large enough S.

2.4 Long-time asymptotics of sustained contact

The equations of motion are

$$\ddot{z} = \frac{k_H}{m} \left(y - z\right)^{\frac{3}{2}}, \tag{2.26}$$

$$y = -\overline{C} k_H \int_0^t \sqrt{t - \tau} \left(y\left(\tau\right) - z\left(\tau\right)\right)^{\frac{3}{2}} \mathrm{d}\tau. \tag{2.27}$$

An initial observation will simplify progress. The largest possible impulse transmitted to the beam equals the momentum of the impacting mass, $m\dot{z}_0$, since there is sustained contact by assumption. For this impulse, the beam motion is roughly $\overline{C} m \dot{z}_0 \sqrt{t}$. Thus, the dominant terms in both y and z are

$$y \sim z \sim \overline{C} m \dot{z}_0 \sqrt{t}. \tag{2.28}$$

Note above that the corresponding velocity goes to zero as $t \to \infty$, and the acceleration goes to zero as well. This means the contact force goes to zero, too. The rest of this section is concerned with correction terms to the above leading order asymptotic behavior.

We integrate Eq. (2.26) to obtain

$$\dot{z}(t) - \dot{z}_0 = \frac{k_H}{m} \int_0^t \left(y - z\right)^{\frac{3}{2}} \mathrm{d}\tau. \tag{2.29}$$

From Eq. (2.27) through integration by parts, inserting Eq. (2.29), we obtain

$$y = \overline{C} k_H \left(-\frac{m}{k_H} \sqrt{t - \tau} \left(\dot{z} - \dot{z}_0\right) \Big|_0^t - \frac{m}{2k_H} \int_0^t \frac{\left(\dot{z} - \dot{z}_0\right)}{\sqrt{t - \tau}} \mathrm{d}\tau \right),$$

where the first term on the right hand side is zero. Thus,

$$y = \frac{\overline{C}m}{2}\int_0^t \frac{\dot{z}_0}{\sqrt{t-\tau}}\mathrm{d}\tau - \frac{\overline{C}m}{2}\int_0^t \frac{\dot{z}}{\sqrt{t-\tau}}\mathrm{d}\tau, \tag{2.30}$$

where the first term is directly $\overline{C}m\dot{z}_0\sqrt{t}$ (recall Eq. (2.28)). We now define a new variable ζ by

$$z = \overline{C}m\dot{z}_0\sqrt{t} + z_\infty + \zeta, \tag{2.31}$$

such that z_∞ is a constant to be determined, and $\zeta \to 0$ as $t \to \infty$. In fact, we will tentatively assume that $\zeta = \mathcal{O}\left(\frac{1}{\sqrt{t}}\right)$ as $t \to \infty$. Equation (2.31) is not a series approximation, however. It represents a change of variables and is exact.

Since $z(0) = 0$, it follows that

$$\zeta(0) = -z_\infty. \tag{2.32}$$

Subtracting Eq. (2.31) from Eq. (2.30) we obtain

$$y - z = -\frac{\overline{C}m}{2}\int_0^t \frac{\dot{z}}{\sqrt{t-\tau}}\mathrm{d}\tau - z_\infty - \zeta. \tag{2.33}$$

From Eqs. (2.26) and (2.31),

$$(y-z)^{\frac{3}{2}} = \frac{m}{k_H}\ddot{z} = \frac{m}{k_H}\left(-\frac{\overline{C}m\dot{z}_0}{4t^{\frac{3}{2}}} + \ddot{\zeta}\right). \tag{2.34}$$

Substituting the right hand side of Eq. (2.34) into the left hand side of Eq. (2.33),

$$\left(-\frac{\overline{C}m^2\dot{z}_0}{4k_H t^{\frac{3}{2}}} + \frac{m}{k_H}\ddot{\zeta}\right)^{\frac{2}{3}} = -\frac{\overline{C}m}{2}\int_0^t \frac{\dot{z}}{\sqrt{t-\tau}}\mathrm{d}\tau - z_\infty - \zeta. \tag{2.35}$$

The left hand side of Eq. (2.35) is exactly $y - z$, and so it is clear that for large t,

$$y - z = \left(-\frac{\overline{C}m^2\dot{z}_0}{4k_H t^{\frac{3}{2}}} + \frac{m}{k_H}\ddot{\zeta}\right)^{\frac{2}{3}} \sim \left(-\frac{\overline{C}m^2\dot{z}_0}{4k_H}\right)^{\frac{2}{3}}\frac{1}{t}, \tag{2.36}$$

and on the right hand side $\zeta \to 0$ as well. Substituting Eq. (2.31) into what remains and dropping the asymptotically smaller contribution in the integral from $\dot{\zeta}$, we obtain

$$z_\infty = -\frac{\overline{C}^2 m^2}{4}\int_0^t \frac{\dot{z}_0}{\sqrt{\tau(t-\tau)}}\mathrm{d}\tau = -\overline{C}^2 m^2 \frac{\dot{z}_0 \pi}{4}. \tag{2.37}$$

What remains in Eq. (2.35) is (still with no approximation)

$$\left(-\frac{\overline{C}m^2\dot{z}_0}{4k_H t^{\frac{3}{2}}} + \frac{m}{k_H}\ddot{\zeta}\right)^{\frac{2}{3}} = -\frac{\overline{C}m}{2}\int_0^t \frac{\dot{\zeta}}{\sqrt{t-\tau}}\mathrm{d}\tau - \zeta. \tag{2.38}$$

For large t, the left hand side is $\mathcal{O}\left(\frac{1}{t}\right)$ as discussed above, while ζ on the right hand side is by assumption $\mathcal{O}\left(\frac{1}{\sqrt{t}}\right)$. Accordingly, we can now drop the left hand side and concentrate on the right hand side alone.

Considering the integral on the right hand side of Eq. (2.38), we write

$$\frac{\overline{C}m}{2}\int_0^t \frac{\dot{\zeta}}{\sqrt{t-\tau}}\mathrm{d}\tau = \overline{C}m\left(\frac{1}{2}\int_0^A \frac{\dot{\zeta}}{\sqrt{t-\tau}}\mathrm{d}\tau + \frac{1}{2}\int_A^t \frac{\dot{\zeta}}{\sqrt{t-\tau}}\mathrm{d}\tau\right), \tag{2.39}$$

where we have split the integral at some intermediate point A. To proceed further, we assume A is large enough such that for $t \geq A$,

$$\zeta \sim \frac{\eta}{\sqrt{t}} + \text{ smaller terms} \tag{2.40}$$

for some η that is yet to be determined. In other words, we choose A large enough that the eventual asymptotic behavior is established; and then we hold A constant. Subsequently considering $t \gg A$, we treat A as being of $\mathcal{O}(1)$ compared to t. With such splitting of the integral, we quickly obtain from Eq. (2.39) (temporarily keeping the factor of $\overline{C}m$ aside),

$$\frac{1}{2}\int_0^t \frac{\dot{\zeta}}{\sqrt{t-\tau}}\mathrm{d}\tau = \left.\frac{\zeta}{2\sqrt{t-\tau}}\right|_0^A - \frac{1}{4}\int_0^A \frac{\zeta}{(t-\tau)^{\frac{3}{2}}}\mathrm{d}\tau - \frac{1}{4}\int_A^t \frac{\eta}{\tau^{\frac{3}{2}}\sqrt{t-\tau}}\mathrm{d}\tau + \text{ smaller terms.} \tag{2.41}$$

Consider the first term on the right hand side of Eq. (2.41). It is (recall Eqs. (2.32) and

(2.37))

$$\frac{\zeta(A)}{2\sqrt{t-A}} - \frac{\zeta(0)}{2\sqrt{t}} = -\frac{\overline{C}^2 m^2 \dot{z}_0 \pi}{8\sqrt{t}} + \frac{\zeta(A)}{2\sqrt{t}} + \text{ smaller terms} \tag{2.42}$$

because A is fixed and $t \to \infty$. Now consider the second term on the right hand side of Eq. (2.41). It can be bounded easily as follows:

$$\left| \frac{1}{4} \int_0^A \frac{\zeta}{(t-\tau)^{\frac{3}{2}}} \mathrm{d}\tau \right| \leq \frac{|\zeta_{\max}|}{4} \int_0^A \frac{1}{(t-\tau)^{\frac{3}{2}}} \mathrm{d}\tau < \frac{|\zeta_{\max}|}{4} \frac{A}{(t-A)^{\frac{3}{2}}} = \mathcal{O}\left(\frac{1}{t^{\frac{3}{2}}}\right) \ll \frac{1}{\sqrt{t}},$$

so this term can be dropped. The third term on the right hand side of Eq. (2.41) can be evaluated in closed form. It is

$$-\frac{1}{4} \int_A^t \frac{\eta}{\tau^{\frac{3}{2}} \sqrt{t-\tau}} \mathrm{d}\tau = -\frac{\eta}{2} \frac{\sqrt{t-A}}{\sqrt{A}\, t} = -\frac{\eta}{2\sqrt{At}} + \text{ smaller terms.} \tag{2.43}$$

Finally collecting the $\mathcal{O}\left(\frac{1}{\sqrt{t}}\right)$ terms from Eqs. (2.42) and (2.43) and inserting them into Eq. (2.41), we obtain

$$\frac{\overline{C}m}{2} \int_0^t \frac{\dot{\zeta}}{\sqrt{t-\tau}} \mathrm{d}\tau = \overline{C}m \left(-\frac{\overline{C}^2 m^2 \dot{z}_0 \pi}{8} + \frac{\zeta(A)}{2} - \frac{\eta}{2\sqrt{A}} \right) \frac{1}{\sqrt{t}} + \text{ smaller terms.}$$

Inserting the above into Eq. (2.38), and recalling that the left hand side thereof is $\mathcal{O}\left(\frac{1}{t}\right)$, we finally have (noting explicitly the t-dependence of ζ on the left hand side)

$$\zeta(t) = -\overline{C}m \left(-\frac{\overline{C}^2 m^2 \dot{z}_0 \pi}{8} + \frac{\zeta(A)}{2} - \frac{\eta}{2\sqrt{A}} \right) \frac{1}{\sqrt{t}} + \text{ smaller terms.} \tag{2.44}$$

The above approximation should hold for *any* large-enough A, and so it does: from Eq. (2.40) we use

$$\zeta(A) \sim \frac{\eta}{\sqrt{A}},$$

giving us the required cancellation in Eq. (2.44). We are left with

$$\zeta(t) = \frac{\overline{C}^3 m^3 \dot{z}_0 \pi}{8\sqrt{t}} + \cdots \tag{2.45}$$

Finally, from Eqs. (2.31), (2.37), and (2.45),

$$z = \dot{z}_0\sqrt{t}\left(\overline{C}m\right) - \frac{\dot{z}_0\pi}{4}\left(\overline{C}m\right)^2 + \frac{\dot{z}_0\pi}{8\sqrt{t}}\left(\overline{C}m\right)^3 + \cdots . \tag{2.46}$$

Let z_{nd}, $\dot{z}_{\mathrm{nd}}$ and t_{nd} denote the dimensionless quantities for length, velocity and time respectively. We rewrite $z = \hat{D}\times z_{\mathrm{nd}}$, $\dot{z} = \hat{V}\times\dot{z}_{\mathrm{nd}}$, and $t = \hat{T}\times t_{\mathrm{nd}}$ in Eq. (2.46), where $\hat{T}$, $\hat{D}$ and $\hat{V}$ are given by Eqs. (2.9), (2.11), and (2.12) respectively. Then, the nondimensionalized solution for the impacting body's motion under sustained contact is

$$z_{\mathrm{nd}} = \dot{z}_{\mathrm{nd}_0}\sqrt{t_{\mathrm{nd}}} - \frac{\dot{z}_{\mathrm{nd}_0}\pi}{4} + \frac{\dot{z}_{\mathrm{nd}_0}\pi}{8\sqrt{t_{\mathrm{nd}}}} + \cdots . \tag{2.47}$$

$\dot{z}_{\mathrm{nd}_0} = \dfrac{\dot{z}_0}{\hat{V}}$ is the nondimensionalized initial velocity.

The above approximation depends only on eventual sustained contact, and is unaffected by the number of separations that precede it.

Figure 2.7 compares asymptotic (Eq. (2.47)) and numerical solutions for two impacts; technical details of numerics will follow in section 2.5. Two rather different impact severities are considered: $S = 15$, with 4 separations; and $S = 1\times10^5$, with no separations. All quantities represented are dimensionless. The match is excellent, for both displacement (z_{nd}) and separation ($y_{\mathrm{nd}} - z_{\mathrm{nd}}$). In particular, it is seen that the long term asymptotic behavior is indeed independent of the number of separations preceding sustained contact.

The above glimpses of excellent agreement between semi-analytical and asymptotic approximations for small and large S, respectively, give us an assurance that our numerical solutions in the next section will be reliable. We now proceed to a fully numerical investigation of the equations of motion, Eqs. (2.7), over the full range of S.

2.5 Full numerical solution of fractional order system

Finally, we turn to detailed numerical solutions spanning the entire range of behaviors of this impact system.

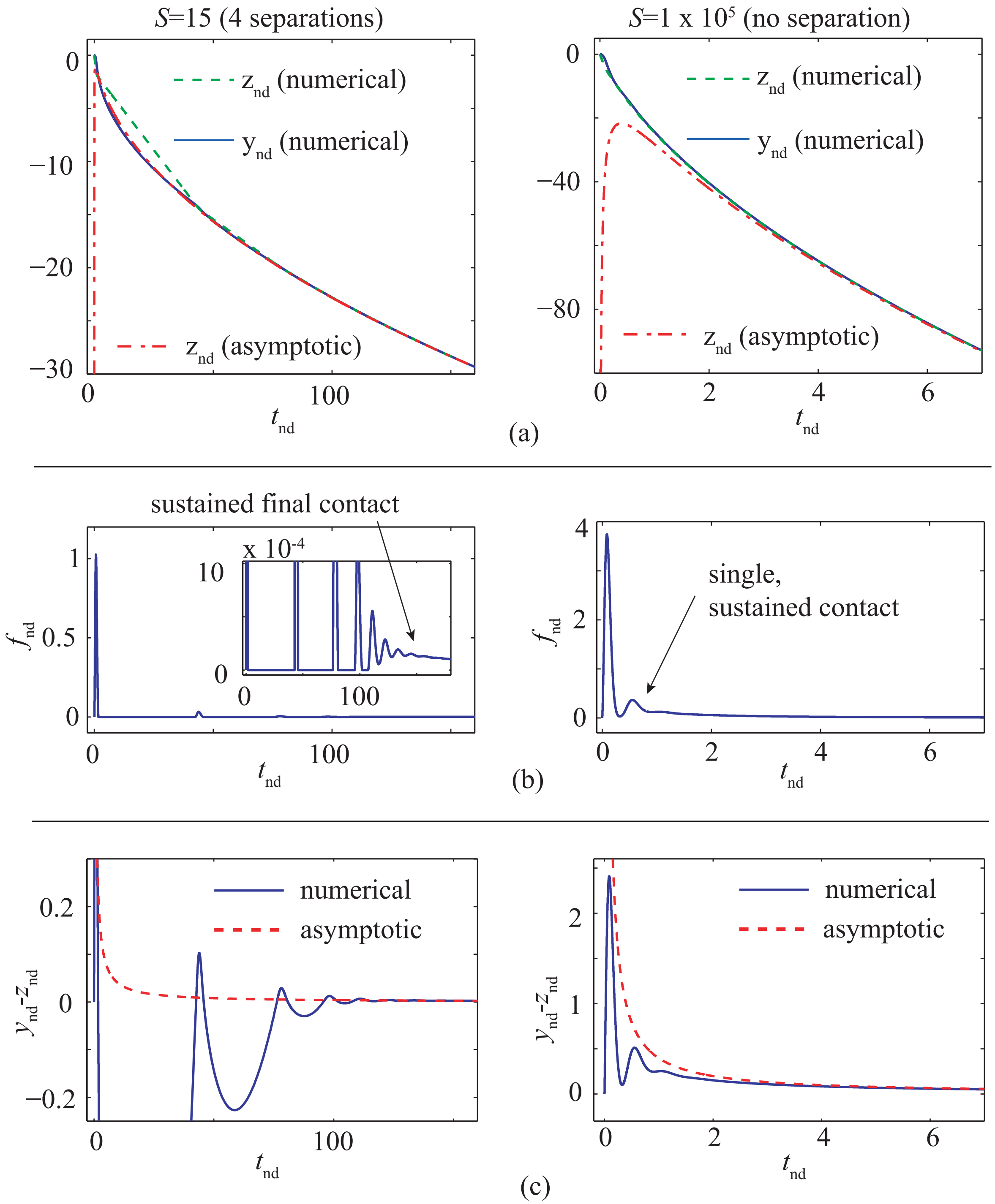

Figure 2.7: Asymptotic and numerical solutions for z_{nd} where sustained contact occurs; y_{nd} solutions are also shown, from numerics, to emphasize separations preceding sustained contact. Left: $S = 15$ (4 separations). Right: $S = 1 \times 10^5$ (no separations). (a) z_{nd} against t_{nd}. (b) contact force history (numerical only). Note the multiple separations on the left side. (c) $y_{\mathrm{nd}} - z_{\mathrm{nd}}$, both asymptotic and numerical. All quantities are dimensionless.

The numerical scheme we use is a recipe given by Das and Chatterjee [69], outlined for completeness in Appendix A.1 (and some comments on numerical accuracy are given there as well). Matlab's stiff ODE solver "ode15s" is used to numerically integrate the equations of motion, with error tolerances "abstol" and "reltol" set to 10^{-11}.

Initial conditions are taken to be $\mathbf{a} = 0$ (see A.1); $y = 0$ and $\dot{y} = 0$ (initially stationary beam); $z = 0$ (first moment of contact) and impact velocity $\dot{z} = -v$.

In our simulations, we vary S from 10^{-10} to 10^5. Since there are four dimensional parameters but only one nondimensional number, we have some freedom in selecting values for dimensional parameters (recall footnote 3). Using Eq. (2.8), we write

$$10\,\log \overline{C} + 2\,\log k_H + 8\,\log m + \log v = \log(S), \tag{2.48}$$

where the right hand side contains the desired value of S, and the parameters on the left hand side are to be determined.

We usually choose $\hat{T} = 1$, $\hat{F} = 1$ and $\hat{D} = 1$. Equations (2.9) and (2.10) then lead to

$$\begin{aligned} 2\,\log \overline{C} + 2\,\log m &= 0, && (2.49) \\ -2\,\log \overline{C} - \log m + \log v &= 0, && (2.50) \end{aligned}$$

and Eq. (2.11) leads to

$$\log k_H = 0. \tag{2.51}$$

Equations (2.48) through (2.51) are easy to solve, and yield parameter values for use in simulations for any desired S.

A direct consequence, following section 2.2.2, is that since $\hat{T} = 1$, $\hat{F} = 1$, and $\hat{D} = 1$, all other dimensional quantities of interest have unit values as well, and consequently all computed quantities we show below have the same numerical values as the corresponding nondimensionalized quantities.

Results from the entire set of simulations are depicted in Fig. 2.8, which summarizes the

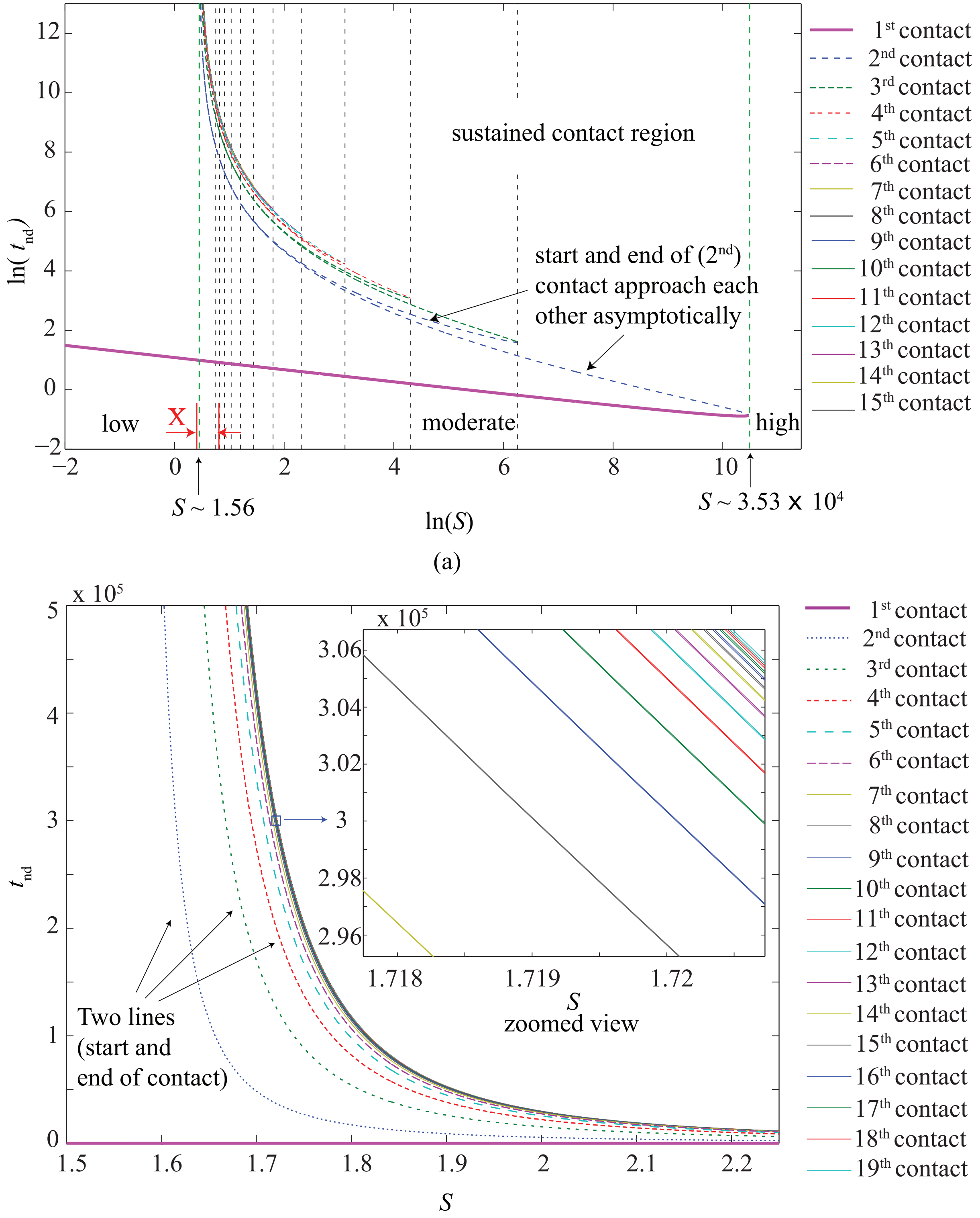

(a)

(b)

Figure 2.8: Time durations (dimensionless) of various contact phases in impacts for different S. See text for details.

numerical contribution of this work. Both subfigures show contact initiation and separation times against S. The upper subfigure uses a logarithmic scale for time, while the lower one uses a linear scale. The complete simulation run takes about 10 hours on an ordinary desktop computer.

In Fig. 2.8, see the upper subfigure first. Contact is initiated at time $t_{\mathrm{nd}} = 0$ in all cases. The time of first separation is shown using a thick magenta curve. That curve turns around at $S \approx 3.53 \times 10^4$, and for still larger S there is never any separation. For $S \lesssim 1.56$, the end of the first contact phase denotes the end of the impact interaction, with the impacting body rebounding away from the beam. For $S \gtrsim 1.56$, first separation occurs with the impacting body still moving toward the beam, and so contact must recur. For S between about 1.56 and 3.53×10^4, first separation is followed by a second contact. The time of initiation of the second contact phase is shown with a blue dashed curve with a vertical asymptote at $S \approx 1.56$.

Looking further, we note that for S between about 1.56 and 5.22×10^2, the end of the second contact phase is followed by a third contact. For a still smaller range of S, there are four contacts, and then five contacts, and then six, and so on, for increasingly smaller ranges of S. We have numerically tracked the first 18 separations, as shown more clearly in the lower subfigure, which is a zoomed portion of the upper one (see the bold red "X"), but drawn on a linear vertical scale. The lower subfigure also has an inset which shows a zoomed portion of itself, indicated by a small rectangle ($t_{\mathrm{nd}} \approx 3$ and $S \approx 1.72$).

As far as we were able to determine numerically, all the above contact-time curves approach the same vertical asymptote at $S \approx 1.56$. Observe that the time durations depicted in these curves range from about $t_{\mathrm{nd}} = 0.5$ to $t_{\mathrm{nd}} \approx 5 \times 10^5$, i.e., they span 6 orders of magnitude and up to 19 different contact events. With standard double precision arithmetic and a nonlinear fractional order system to solve, we were unable to confidently pursue these curves further. However, a reasonably detailed and clear picture has emerged from the accuracy we were able to muster[4].

---

[4] Actually, for $1.559 < S < 1.8$, simulation times were very long and different scalings from those obtained from Eqs. (2.48) through (2.51) were used. The idea used was to scale the initial maximum force to higher

For easier viewing in Fig. 2.8, successive pairs of curves, denoting the start and end of a contact phase, have been colored the same. At larger times, because the contact durations stay relatively much smaller, these curves visually seem to coalesce, although in fact they remain distinct. In the upper subfigure, it is seen clearly that beyond $S \approx 1.56$, increasing S is accompanied by fewer separations. The turning points for the different curves, indicating the disappearance of the first separation (at 3.53×10^4), and then the disappearance of the second separation (at 5.22×10^2), etc., are listed below, starting from the right and going sequentially until the 12th separation, followed by the limit close to 1.56 as discussed above:

> 3.528×10^4, 5.219×10^2, 74.391, 22.403, 10.185, 6.030, 4.238, 3.328, 2.808, 2.485, 2.271, 2.121, $\cdots$ 1.559.

The above numerically obtained series concludes our numerical study.

2.6 Concluding remarks

We have studied the lateral impact of a compact Hertzian body with an infinitely long Euler-Bernoulli beam. The motion of the beam's contact point is given by a fractional-order equation, and contact with the colliding body is mediated by a nonlinear spring. Solution for the body and beam-contact-point's coupled equations of motion are obtained numerically using the recipe of [69].

The contact dynamics depends on four system variables, reducible to a single non-dimensional number S. For low S there is a single impact followed by separation. For moderate S, there are one or more separations followed by eventual sustained contact. For still higher S, there are no separations. For S very slightly above about 1.559, the number of separations before eventual sustained contact can be large.

Beyond the numerical picture obtained as above, a semi-analytical approximation for the first contact phase for low and moderate S impacts, and an asymptotic solution for

---

values, because contact force magnitudes dropped rapidly with subsequent contacts. For uniformity, final results were nondimensionalized.

the long-term behavior in sustained contact for relatively high S impacts, have also been developed. Both show excellent agreement with numerics.

Studies of impacts between solid bodies have often qualitatively distinguished between two main types of impacts: those that cause significant global deformations, wave effects, and vibrations during the impact; and those in which deformations are strongly localized near the contact region (see, e.g., discussion in [10]). In the first kind of impact, i.e., with non-localized deformations and waves, an academically interesting and practically somewhat useful idealization is the impact between a compact body and a large and flexible object like a plate or a beam. Of these idealized problems, the sphere-and-plate impact is simpler and was worked out several decades ago. The impact problem between a compact Hertzian body and an infinitely long Euler-Bernoulli beam, on the other hand, had not been satisfactorily studied until now, in part because of its nonlinearity coupled with a fractional derivative, and in part because good analytical progress was difficult. In this study, due to a few fortuitous insights, we have managed to obtain some new understanding of the contact dynamics of this system, for the first time, and at a level of detail not available before.

Chapter 3

Finite-beam impact: Interplay between dissipation and modal truncation in convergence of restitution

In this chapter, we study the impact of a Hertzian sphere or a ball on a *finite*-length Euler-Bernoulli beam. For simplicity, the beam is taken as uniform and simply supported. The impact location is varied. The goal is to understand the nature of convergence of impact solutions obtained using modal expansions for the beam. The material in this chapter has been published in [56].

3.1 Introduction

The dynamics of flexible bodies undergoing collisional contact is difficult to model reliably and accurately. Ahn and Stewart [70] discuss, on an abstract mathematical footing, the complications in elastodynamic impact without viscosity. It is qualitatively anticipated that the presence of dissipation can regularize impact interactions, although many sub-impacts may still occur within a single macroscopic impact interaction (e.g., if a ball is dropped on a beam, contact may be rapidly made and broken several times before the ball shows its final macroscopic net upward rebound).

In engineering applications and simulations, *modal expansions* are frequently used. It is either tacitly or explicitly assumed that with sufficiently many modes, and with reasonable dissipation, the final results obtained will be both physically accurate as well as insensitive to modeling approximations. Behind such assumed convergence, systematic study is necessary. Such a study, for the case of a single instantaneous impulsive impact (corresponding to one sub-impact in our detailed simulations later) was conducted in [37] with various sets of assumed-mode expansions for a rotating beam. The same instantaneous impulse approximation along with a coefficient of restitution for each sub-impact has been used in modeling by Yigit *et al.* [12].

However, a detailed study of convergence in an actual vibration-dominated impact simulation, with many modes active and with many sub-impacts within the single macroscopic impact, with and without dissipation, and with every sub-impact resolved in time using Hertzian or similar compliant contact, has not been presented in the literature.

It is the aim of this work to address this gap in the study of modal expansions for vibration-dominated impact. To this end, we take up for study the frictionless and purely transverse impact of a Hertzian ball with an Euler-Bernoulli beam of square cross section. We assume for simplicity and clarity that the beam has ideal pinned ends, so that the mode shapes have a simple analytical form.

In this chapter we study this ball-beam impact system through detailed numerical simulations, modeling the contact in detail, resolving all the sub-impacts within each macroscopic impact, and examining many different cases as follows.

First, the system is simulated with no dissipation whatsoever. Hertzian contact is assumed between the ball and the beam. The restitution observed (along with other collision details) varies even with many modes retained (more than 60), but on average shows a decreasing trend with increasing numbers of modes. There is also a significant dependence on the location of contact. These phenomena have been noted qualitatively, in passing, and/or through small numbers of modes, in other work as well [12, 13, 26]. We emphasize that this initial aspect of our study is more systematic and detailed than any previous study we are aware of; and we proceed further in our search for meaningfully converged behavior.

Next, we note that stresses are largest in the contact region, and so dissipation in the contact may need to be incorporated. Since there is a large body of literature that shows material dissipation to be rate independent, we examine both (a) a convenient viscous dashpot model, as well as (b) a rate-independent hysteretic damping mechanism in the contact region. Interestingly, contact dissipation fails to make outcomes less scattered in both cases.

Finally, we introduce a fixed and small amount of modal damping in all retained modes ($\zeta = 0.02$ or two percent damping). In this case, we find the most interesting results of all. When only a few modes are retained, there is no change in outcomes. Yet, with large numbers of retained modes, there is convergence in the observed net restitution and other collision details. A simple physical and intuitive explanation for this observed behavior also emerges from a study of the details of the collisions.

For the particular ball-beam (pinned-pinned) system under study, we find that with modal damping on the order of 0.02 and about 25 or more modes retained, the variability in the restitution gets reasonably small and convergence in a loose sense is obtained.

One of the smaller issues studied through the above simulations is the role of the contact point location, which is known to be significant. For example, there is a marked difference between a contact location at $2/5$ of the length (a simple rational value) and a contact location at $(\sqrt{5}-1)/2$ (an irrational value), with the latter location showing richer, or more variable, behavior even with many modes retained. However, with modal damping, a reasonable behavior with increasing numbers of modes, suggesting convergence for practical purposes, is obtained in both cases.

In subsequent subsections, we first describe the physical system studied, and present equations of motion in the absence of damping. Then we present simulation details and results for the dissipation-free case. Subsequently, we provide brief details of various dissipation models incorporated, and numerical strategies used as appropriate. Finally, we present our results and a concluding discussion.

We end this introduction with a quick review of the relevant literature. In flexible body impacts, contact has been modeled at different levels, like including the net impulse-momentum balance along with coefficients of friction and restitution [6, 23], and the continuous or incremental contact approach like Hertzian contact [13, 14], among others. Dissipation in impacts (for rigid and flexible body impacts) has been modeled variously as well. Direct lumped dissipation modeling through a coefficient of restitution is simplest and perhaps commonest. Friction [11, 53] or viscous effects [25, 71] or plastic deformation at the contact [28, 72, 23], and modal dissipation in the vibrating body [13, 14, 73] have also been used. There are, in various papers, brief mentions or discussions of the possible effects of higher modes of vibration on sub-impacts, the effects of modal or structural damping on restitution, and similar topics (see e.g., [13, 14, 19]). However, as emphasized above, a clear and detailed study on the convergence of restitution or other aspects of the impact dynamics, with increasing numbers of retained modes and the role of dissipation therein, is lacking in the literature. In particular, we will offer below a simple and clear understanding of the interplay between dissipation and modal truncation in ball-beam impact.

3.2 Basic equations of motion *via* modal expansion

We present the equations of motion for the transverse impact of a sphere on a pinned-pinned Euler-Bernoulli beam. See Fig. 3.1.

The beam has uniformly distributed mass $\overline{m}$, length l, and flexural rigidity EI. The sphere has mass m.

The sphere hits the beam at a distance b from one of its ends. All displacements are small. The displacement (upwards) of the beam is taken as usual to be $y(x,t)$. The distance (upwards) of the notional point of contact of the sphere from the beam's notional undeformed surface is taken as $z_b(t)$ (see Fig. 3.1). The sphere collides with the elastic beam with a velocity of $\dot{z}_b(t)$. The sphere has negligible internal vibration, and behaves

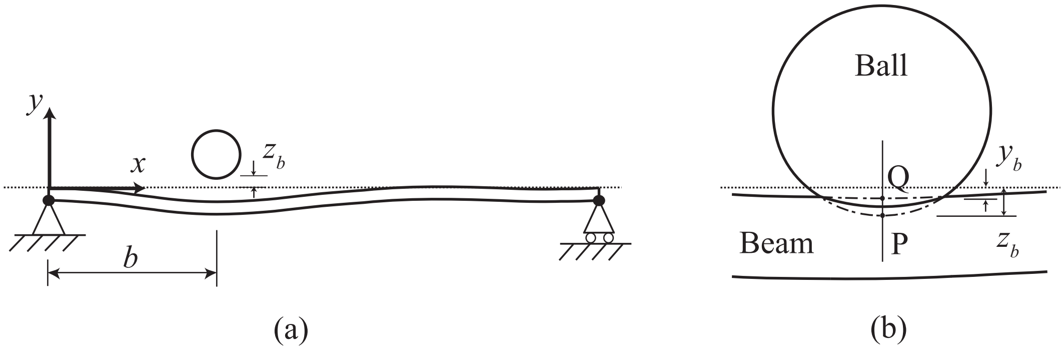

Figure 3.1: (a) Transverse impact of a Hertzian ball on a pinned-pinned Euler-Bernoulli beam at a distance b away from the end. The displacement of the beam and the ball are referred to as $y(x,t)$ and $z_b(t)$ respectively. (b) The ball-beam contact. The unbroken lines show the actual configuration at contact. P is the notional contact point on the undeformed ball (i.e., the ball without localized contact deformation). Q is the notional contact point where the ball hits the beam. The distance from P to Q is the compression (positive in the sense shown); and a contact force exists when the compression is positive.

like a rigid sphere that interacts with the beam through a tiny massless compliant element. We neglect gravity (see section 3.3.2 for discussion).

We use the Lagrangian formulation to obtain the equations of motion during impact. The beam's potential energy and kinetic energy are

$$PE = \frac{EI}{2}\int_0^l \left(y''\left(x,t\right)\right)^2 dx, \qquad KE = \frac{\overline{m}}{2}\int_0^l \left(\dot{y}\left(x,t\right)\right)^2 dx, \tag{3.1}$$

where $y'(x,t)$ and $\dot{y}(x,t)$ denote partial derivatives with respect to x and t respectively.

We discretize the beam's transverse displacement as

$$y(x,t) = \sum_{n=1}^{N} a_n(t)\phi_n(x), \tag{3.2}$$

where $\phi_n(x)$ is the nth mode shape corresponding to the generalized coordinate $a_n(t)$. We now have the beam's potential and kinetic energy as

$$PE = \frac{EI}{2}\int_0^l \left(\sum_{n=1}^{N} a_n(t)\phi_n''(x)\right)^2 dx = \frac{\mathbf{a}^T\mathbf{K}\mathbf{a}}{2}, \tag{3.3}$$

where $K_{ij} = EI \int_0^l \phi_i'' \phi_j'' dx$, and

$$KE = \frac{\overline{m}}{2} \int_0^l \left(\sum_{n=1}^{N} \dot{a}_n(t) \phi_n(x) \right)^2 dx = \frac{\dot{\mathbf{a}}^T \mathbf{M} \dot{\mathbf{a}}}{2}, \tag{3.4}$$

where $M_{ij} = \overline{m} \int_0^l \phi_i \phi_j dx$. In the above, $\mathbf{a}$ is a vector of the generalized coordinates $\{a_n\}$. $\mathbf{M}$ and $\mathbf{K}$ are the mass and stiffness matrices respectively. The mode shapes (pinned-pinned) are

$$\phi_n(x) = \sin\left(\frac{n\pi x}{l}\right), \;\; n = 1, 2, \ldots N. \tag{3.5}$$

The orthogonality of $\phi_n(x)$ results in diagonal mass ($\mathbf{M}$) and stiffness ($\mathbf{K}$) matrices.

There remains one more degree of freedom, namely $z_b(t)$, the displacement of the ball. The ball's potential and kinetic energy are

$$\begin{aligned} PE &= 0, \qquad\qquad \text{(because gravity is neglected)} \\ KE &= \frac{1}{2} m \left(\dot{z}_b\left(t\right)\right)^2. \end{aligned} \tag{3.6}$$

Thus, for N assumed modes, the system has $N+1$ degrees of freedom.

The contact force is included here as a non-conservative force F that acts upwards on the ball and downwards on the beam. The virtual work done on the beam for a virtual displacement of $\delta y|_{x=b}$ is

$$\delta W_{beam} = -F \delta y|_{x=b} = -F \sum_{n=1}^{N} \phi_n(b) \delta a_n. \tag{3.7}$$

The virtual work done for a virtual displacement δz_b of the ball is

$$\delta W_{ball} = F \delta z_b. \tag{3.8}$$

The corresponding generalized forces for the individual degrees of freedom are obtained routinely.

The equations of motion obtained are:

$$\begin{aligned} \frac{\overline{m}}{2}\ddot{a}_n + \frac{EIn^4\pi^4}{2l^4}a_n &= -F\phi_n(b), && (3.9) \\ m\ddot{z}_b &= F, && (3.10) \end{aligned}$$

representing N and 1 equations respectively. We now discuss various choices of F.

3.2.1 Contact force model

Let ξ be the local compression at the contact location (see Fig. 3.1(b)), i.e.,

$$\xi = \sum_{n=1}^{N} a_n\phi_n(b) - z_b, \qquad \dot{\xi} = \sum_{n=1}^{N} \dot{a}_n\phi_n(b) - \dot{z}_b. \tag{3.11}$$

We now consider various contact models.

Hertzian contact

In Hertzian contact, F is

$$F = k_H \langle \xi \rangle^{1.5}, \tag{3.12}$$

where the angle brackets denote

$$\langle \xi \rangle = \begin{cases} \xi & \xi \geq 0, \\ 0 & \xi < 0. \end{cases} \tag{3.13}$$

In Eq. 3.12, K_h is the Hertzian contact stiffness given by [1]

$$k_H = \frac{2E\sqrt{R}}{3\left(1-\nu^2\right)}, \tag{3.14}$$

where R is the radius of the ball, the beam surface has been taken as flat, and both ball and beam are assumed to be made of the same material.

Viscous contact dissipation

Viscous losses are considered at the impact location by some other authors (see [12, 25] and references therein). Here, when we incorporate such viscous dissipation, F will be taken as

$$F = k_H \left\langle \xi \right\rangle^{1.5} (1 + c\,\dot{\xi}), \tag{3.15}$$

where c is a numerically-small constant. We assume, and will check, that the numerical value of $|c\,\dot{\xi}| < 1$ at all times, so that $F = 0$ only when $\xi = 0$.

Hysteretic contact dissipation

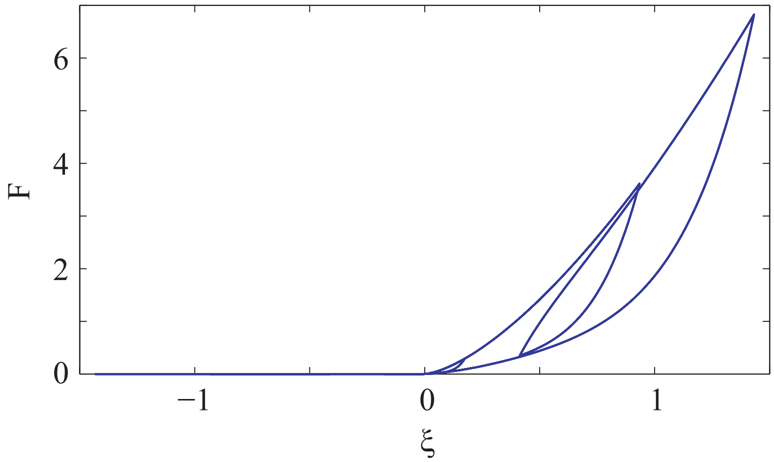

Figure 3.2: F-ξ hysteresis loops seen for input $\xi = \sin(2\pi t) + 0.5\sin(8\pi t)$, see Eqs. 3.16 and 3.17. Parameters used here are $k_H = 1, \overline{K} = 4, \theta_m = 1.6$, $\beta = 1.4$, $\epsilon = 1 \times 10^{-4}$.

Many materials exhibit rate-independent dissipation [74]. We will consider rate-independent *contact* dissipation. To that end, as an empirical rate-independent hysteretic damping model that retains the flavor of Hertz contact, we will slightly modify a formula proposed in [75]. Specifically, we will take the contact force F to be

$$F = k_H \left\langle \xi \right\rangle^{1.5} (1 + \theta), \tag{3.16}$$

where θ is an internal variable governed by

$$\dot{\theta} = \frac{\overline{K}\left(\theta_m + \beta\,\mathrm{sign}(\xi\,\dot{\xi}) - \theta\right)\langle\xi\rangle}{|\xi| + \epsilon}|\dot{\xi}|, \tag{3.17}$$

where in turn $\overline{K}, \theta_m, \beta > 0$ are model parameters, and ϵ is a tiny regularization parameter used to handle the singularity at $\xi = 0$.

During numerical simulation, the value of θ varies between $\theta_m \pm \beta$. A typical hysteretic response on F-ξ axes, obtained with this model, is shown Fig. 3.2. The input used is $\xi = \sin(2\pi t) + 0.5\sin(8\pi t)$. As seen in the figure, $F = 0$ only when $\xi \leq 0$, unlike some simpler models wherein upon unloading we obtain $F = 0$ with $\xi > 0$ (e.g., [28] and others). Equations 3.16 and 3.17 have the advantage of reasonably modeling minor loops under complex loading and unloading. This feature is attractive for impacts with several sub-impacts and vibrations therein, with no significant permanent indentation.

Modal damping

Finally, we consider modal damping in the beam. In the equations of motion, Eq. 3.9 is replaced with

$$\ddot{a}_n + 2\zeta\omega_n\dot{a}_n + \omega_n^2 a_n = -\frac{2F}{\overline{m}}\,\phi_n(b), \qquad n = 1\ldots N, \tag{3.18}$$

with $\omega_n = \sqrt{\frac{EI}{\overline{m}}}\frac{\pi^2 n^2}{l^2}$ and $\zeta = 0.02$ (say) for all modes. Contact remains Hertzian (recall Eq. 3.12).

3.3 Numerical study of convergence

We now present results of detailed numerical simulations of the ball-beam impact for the different contact force models mentioned in section 3.2.1 above.

3.3.1 Parameter choices and procedural aspects

In our simulations, both the sphere and the beam are assumed to be of the same material ($E = 2 \times 10^{11}$ Pa or 200 GPa, $\nu = 0.3$, $\rho = 7800$ Kg/m^3). The beam has a square cross-section with sides taken as 0.011323 m and length 1 m. The square section makes the contact surface flat and the Hertz contact stiffness expression simpler. The sphere has a diameter of 0.03 m and consequently mass 0.11027 Kg, unless otherwise noted. The ball and the beam cross section have comparable dimensions (are of the same order of magnitude). The ball hits the beam with a velocity of 1 m/s unless otherwise noted.

The equations are integrated numerically using Matlab's stiff ode solver "ode15s", with error tolerances "abstol" and "reltol" set to 10^{-11}. We take the initial conditions to be $a_n = 0, \dot{a}_n = 0$ for all n (the beam is at rest when the ball first strikes); $z_b = 0$ (first moment of contact); and impact velocity $\dot{z}_b = -1$ unless otherwise noted. The impact duration and displacements are small, but the error tolerances used are sufficiently tight for reliable results (we verified that changing the tolerances did not change the obtained answer). Matlab's ode solver `ode15s` uses adaptive step sizing to estimate and control the error. A typical solution computed by Matlab had step sizes ranging from below 1×10^{-8} to well below 1×10^{-6} with 60 modes retained (when the highest natural frequency retained was under 1×10^{5} Hz). The first natural frequency was close to 26 Hz (time period as 0.0385 second), and the 60$^{\text{th}}$ natural frequency is thus $60^2 \times 26 \approx 93600$ Hz (time period is 1.0684×10^{-5} second).

Numerical integration was continued until we were sure that the ball-beam interaction is over, which we checked by ensuring that z_b (the ball position) was sufficiently high (such as 0.02 m, or sometimes smaller values as suggested by visual assessment of results). We define the coefficient of restitution (e) as

$$e = -\frac{\dot{z}_{\text{separation}}}{\dot{z}_{\text{impact}}}, \tag{3.19}$$

where $\dot{z}_{\text{separation}}$ and $\dot{z}_{\text{impact}}$ denote the ball's rebound and approach velocity respectively.

Beam vibration velocities at the instant of separation will be damped out soon, and will not be seen in overall large motions of the system.

We commonly observed multiple sub-impacts within single macroscopic impacts. Event detection in Matlab was used for all simulations with hysteretic dissipation in the contact, wherein several sequential partial simulations were then patched together for the full solution. For all other (non-hysteretic) cases the stiff solver was able to adaptively handle the smooth (Hertzian power law of 1.5) transitions between contact and separation, and event detection was found to be unnecessary; in such cases a single simulation command was most convenient.

It is known that the restitution varies with the point of impact [76]. We therefore considered impact at two locations, at $b = 0.4$ (a rational number) and $b = (\sqrt{5} - 1)/2 = 0.618034\cdots$[1]. Note that, by symmetry, $b = 0.4$ is the same as $b = 0.6$ (because the beam length is unity); and thus the two b's are effectively only slightly apart.

Simulation results follow.

3.3.2 Hertzian contact

We begin with dissipation-free, pure Hertzian contact (Eq. 3.12), which for our chosen parameters gives

$$k_H = 1.7945 \times 10^{10}\ \mathrm{N/m^{1.5}}. \tag{3.20}$$

For understanding, Fig. 3.3 shows the detailed system response during the entire collision interaction with $N = 25$ modes and for impact location $b = 0.4$. The upper figure shows motion quantities and the lower figures shows the contact force. The middle figure shows the contact force against time, whereas the bottom figure shows the same on a magnified time scale. We see several sub-impacts of comparatively brief durations within the total macroscopic impact. At $t = 0$, the beam is at rest, while the ball just touches the beam with a velocity of -1 m/s. Contact occurs when $\xi = y_b - z_b \geq 0$, i.e., whenever the

---

[1] The number $\dfrac{\sqrt{5}-1}{2} = 0.618033$ is considered to be "highly" irrational; see [77]. For this choice of b, we can anticipate that almost all modes will be significantly excited.

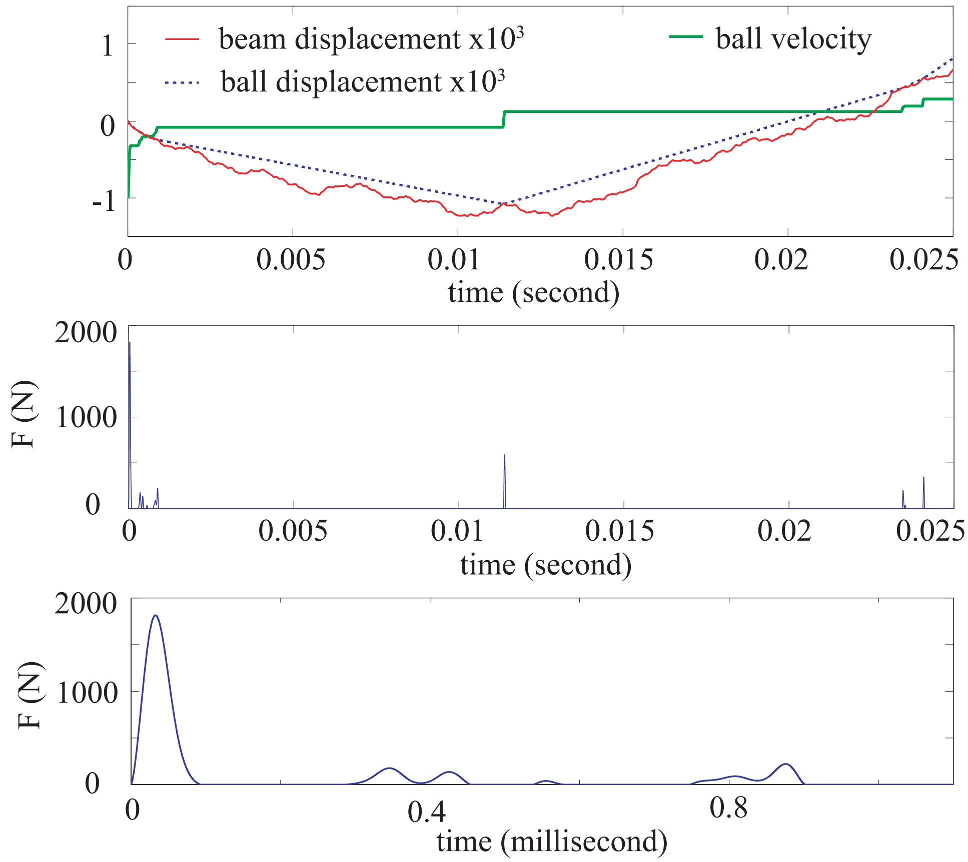

Figure 3.3: Impact with Hertzian contact with $N = 25$ modes and $b = 0.4$. The top figure shows the ball and beam motions during impact, using SI units but with displacements scaled up by a factor of 1000. In other words, the velocity scale is m/s and the displacement scale is mm. The middle figure shows F in Newtons. The bottom figure shows details of F on a magnified time scale.

blue line (z_b) touches or goes below the red line (y_b). During contact, F shows spikes and the ball's velocity changes relatively rapidly. In between sub-impacts, the ball moves with a constant velocity because gravity is neglected. The beam's lower mode coordinates have comparatively larger magnitudes, and dominate its displacement; however, higher mode coordinates contribute significantly to velocities, and the displacement curve is not very smooth. Some sub-impacts occur after a relatively long gap without contact (see the later spikes in F plot), suggesting the possibility of somewhat complicated behavior; such complexities will be seen below.

See Fig. 3.4. The ball's rebound velocity or restitution (top) and the number of sub-

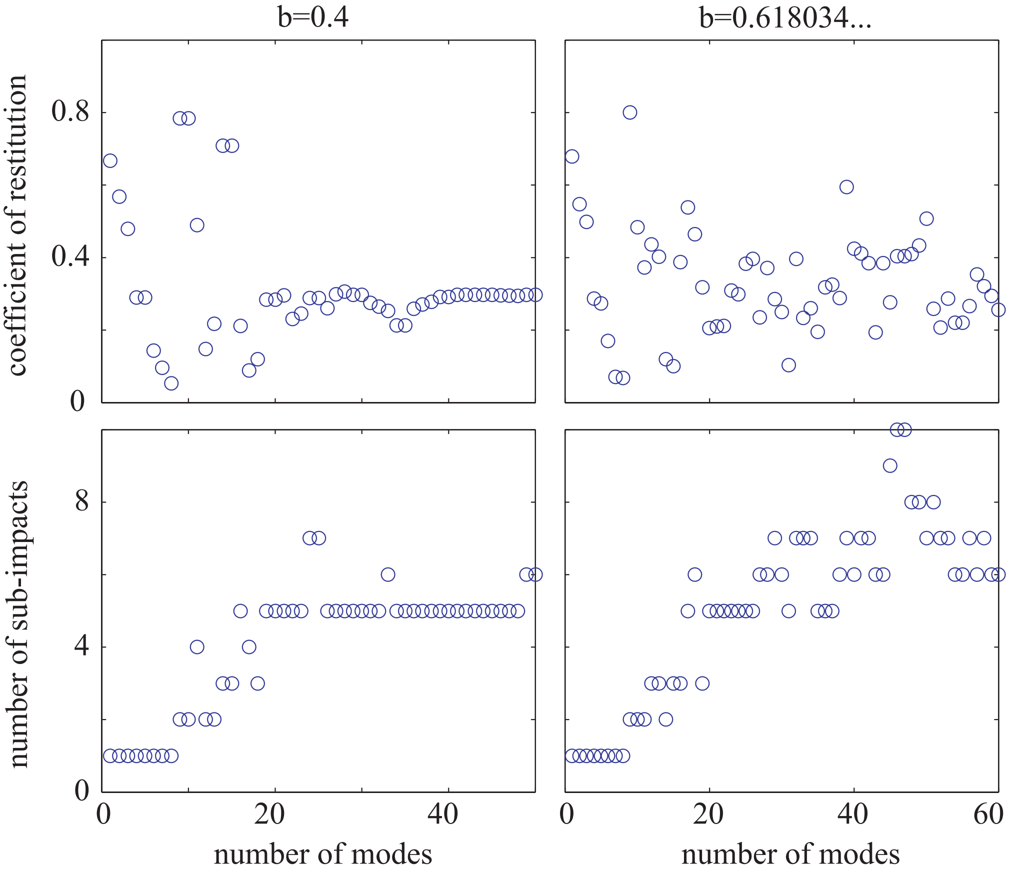

Figure 3.4: Hertz contact, see Eq. 3.12 for F. Two impact locations are considered, left: $b = 0.4$, and right: $b = (\sqrt{5} - 1)/2$. Top: net restitution, and bottom: number of sub-impacts, both against number of modes retained (N). For $b = 0.4$, mode numbers 5, 10, 15, $\cdots$, are not excited at all. For this reason, it serves as a check to note that results for $N = 4$ and 5 are identical; results for 9 and 10 are identical; and likewise 14 and 15, 19 and 20 etc. For $b = 0.618034\cdots$, no such simple check is available.

impacts (bottom) are shown against the number of modes retained, for $b = 0.4$ (left) and $b = (\sqrt{5} - 1)/2$ (right). The axes scales (divisions) are the same along the rows and the columns for the subplots. For few modes retained, say $N < 8$, the response is similar for both b's. However, as N increases, many sub-impacts occur and results for the two b's differ significantly. In particular, for the irrational choice of b, convergence is very slow. Note that, by symmetry, $b = 0.4$ is identical to $b = 0.6$, which is not much different from $b = 0.618034\cdots$; the difference in outcomes is presumably because the latter location is irrational, and so all modes (including the fifth, tenth, etc.) are excited.

Since the mode shapes for the simply supported case are of the form $\sin(n\pi x)$, for $x = b = 0.4$ we find that $\sin(0.4n\pi) = 0$ whenever $0.4n$ is an integer, i.e., $n = 5, 10, 15, \cdots$. These modes are therefore not excited in the impact. Consequently, results for $N = 4$ and 5 are identical, as are results pairwise identical for $N = (9, 10), (14, 15), (19, 20), \cdots$. This equivalence is indeed seen in the left subplots, and serves as an elementary check on the numerical results.

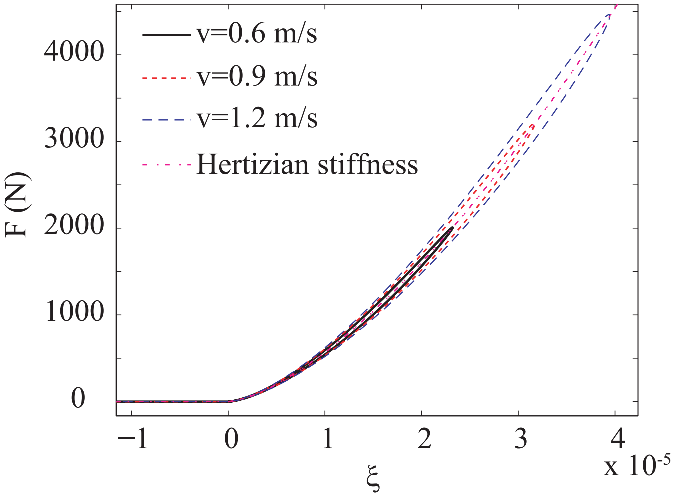

Figure 3.5: Impact with $N = 0$. The viscous contact force F is plotted against ξ for ball impact velocities of 1.2 m/s, 0.9 m/s, and 0.6 m/s. The loops are rounded at the ends.

We now comment briefly on the neglect of gravity in our simulations. The contact force magnitudes are of the order of a few hundred Newtons (see Fig. 3), while the ball weight is on the order of 1 N. Gravity would merely make the straight line portions of Fig. 3.3 (top) very slightly curved. Alternatively, if the beam was vertical and the ball motion was horizontal, then using the formula $s = \frac{1}{2}gt^2$ and a net time of 0.025 seconds, we see that the vertical travel of the ball would be about 3 mm, which is small compared to the beam length. All in all, these small effects would not change our main conclusion about modal truncation.

We will use pure Hertzian contact as a reference case below, as we consider various forms of dissipation in the impact.

3.3.3 Viscous contact dissipation

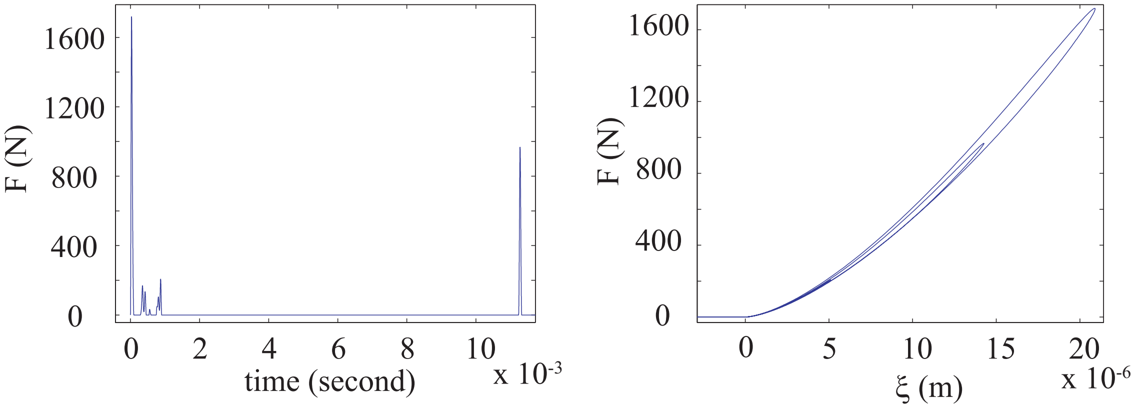

Figure 3.6: Impact with $N = 27$ modes. Left: F vs. t, right: F vs. ξ. The F vs. ξ loops indicate dissipation of energy.

Here, viscous contact dissipation is considered: see Eq. 3.15. To choose c, we separately simulated the impact of the ball while artificially holding the beam fixed ($N = 0$). By $N = 0$ we mean that *no* beam modes are retained, i.e. $\xi = -z_b$ and $\dot{\xi} = -\dot{z}_b$ (see Eq. 3.11). We found that $c = 0.08$ gave a rebound of about 0.95 m/s for an impact velocity of 1 m/s. We used this same c value in our numerical study of convergence with increasing N.

Figure 3.5 shows the viscous dissipation force with ξ during such an impact for three different ball velocities. There is a single contact in each case. The loops are rounded at the ends. Fig. 3.6 shows the F vs. ξ loops for impact velocity 1 m/s, $N = 27$ and $b = 0.4$. Multiple sub-impacts occur.

Results are given in Fig. 3.7, which is displayed using the same scheme as in Fig. 3.4. Red crosses denote the dissipative contact, while blue circles denote the original nondissipative Hertzian case. It is seen that small contact dissipation has no significant effect in speeding up convergence with increasing N, although *on average* there is some indication of lower rebound.

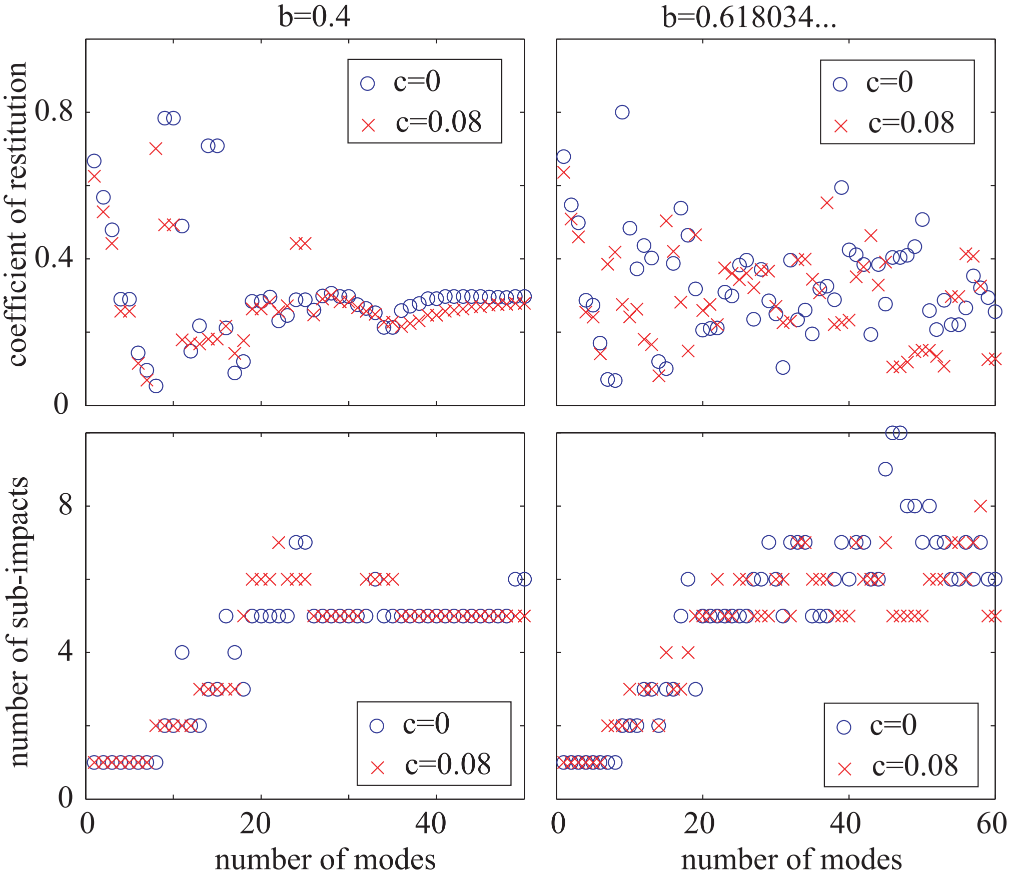

Figure 3.7: With and without viscous contact dissipation, see Eqs. 3.12 and 3.15. Two locations, left: $b = 0.4$, and right: $b = (\sqrt{5} - 1)/2$. Top: net restitution, and bottom: number of sub-impacts, both against N.

3.3.4 Hysteretic contact dissipation

Here, rate-independent hysteretic dissipation is considered in the contact: see Eqs. 3.16 and 3.17. Recall that an additional differential equation is included for the evolution of the internal variable θ,

$$\dot{\theta} = \frac{\overline{K}\left(\theta_m + \beta\,\mathrm{sign}(\xi\,\dot{\xi}) - \theta\right)\langle\xi\rangle}{|\xi| + \epsilon}|\dot{\xi}|.$$

Using both Matlab's event detection as well as "ode15s", with error tolerances of 1×10^{-11} and parameter $\epsilon = 5 \times 10^{-8}$, the simulation worked well[2].

---

[2] Additionally, at the start of each sub-impact, it is numerically best (as indicated by the small-ϵ limit, not discussed here to save space) to take $\theta = \theta_m + \beta$ as the initial value of θ. All other dynamic (modal and ball) coordinates are obtained from numerical integration through the non-contact phase.

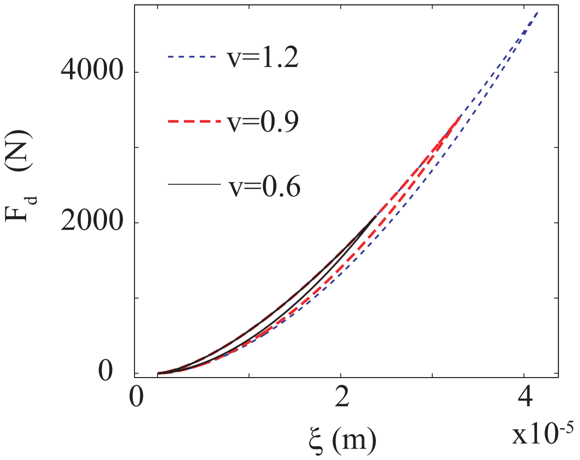

Figure 3.8: Impact with $N = 0$. Parameters used are $\theta_m = 1.6$, $\beta = 1.4$, $\overline{K} = 0.4$, $\epsilon = 5 \times 10^{-8}$, see Eqs. 3.16 and 3.17. The hysteretic force F is plotted against compression for ball impact velocities of 1.2 m/s, 0.9 m/s, and 0.6 m/s. The restitution values obtained are close to 0.95 in each case, decreasing very slightly with increasing impact velocity.

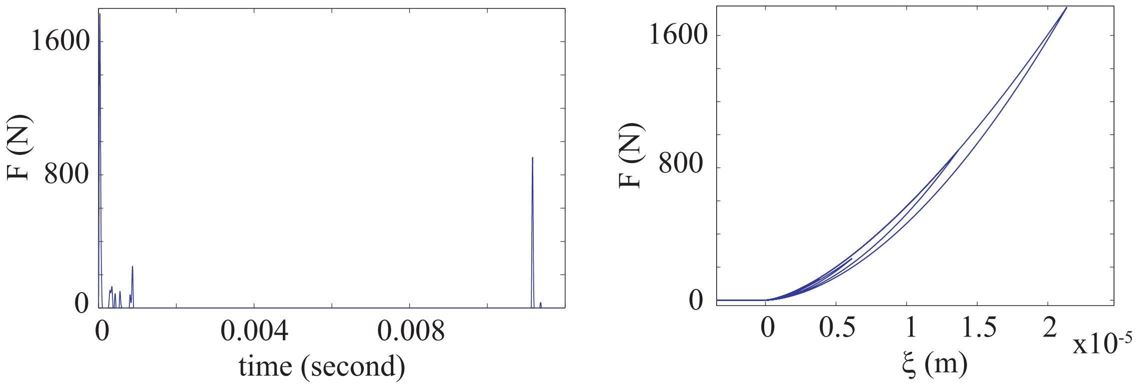

Figure 3.9: Impact with $N = 27$ modes. Left: the hysteretic contact force against time, right: hysteresis loops in the contact force, including minor loops.

As we did for the viscous contact case, we first artificially fix the beam ($N = 0$, *no* beam modes are retained), and choose the hysteresis model parameters to obtain a restitution of about 0.95 when the impact velocity is 1 m/s. Figure 3.8 shows the hysteretic force with ξ during such an impact for three different ball velocities. There is a single contact in each case and the hysteresis loops are plotted on the same scale for comparison. The parameters used are $\theta_m = 1.6$, $\beta = 1.4$, $\overline{K} = 0.4$, and $\epsilon = 5 \times 10^{-8}$, along with an adjusted K_h as explained below.

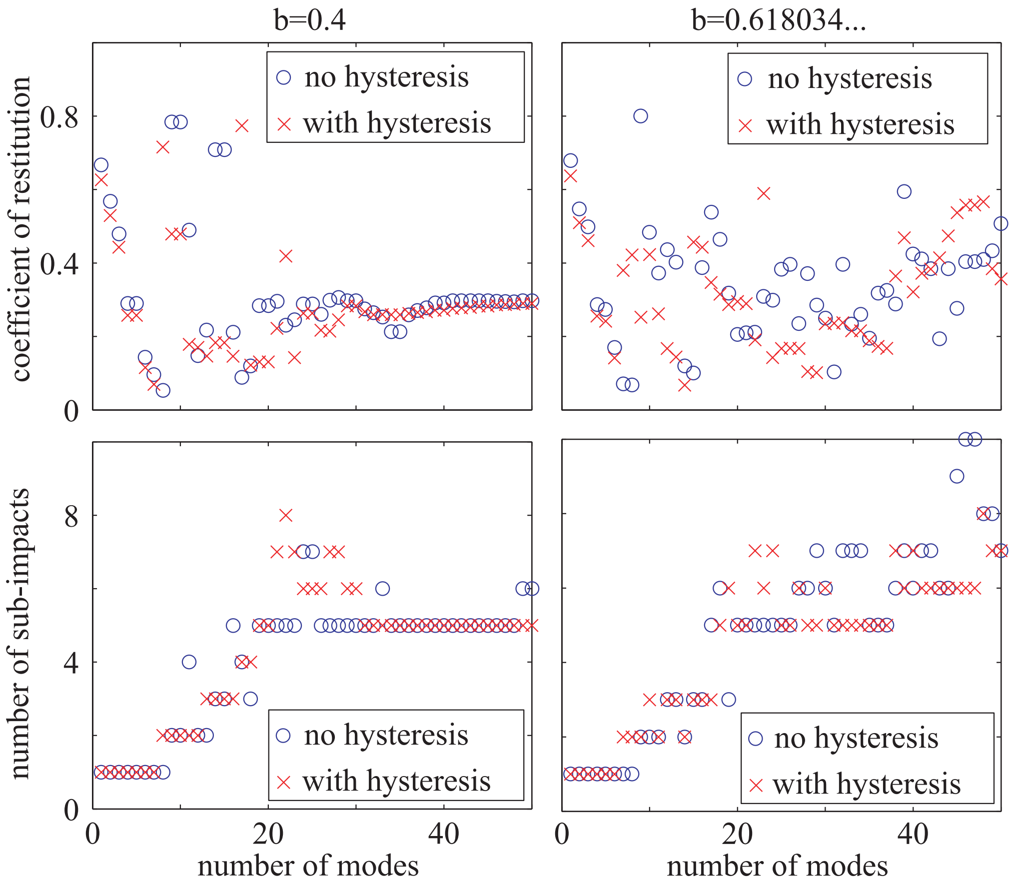

Figure 3.10: See section 3.3.4. Impact with rate-independent contact dissipation (red crosses) and without (blue circles). Left: $b = 0.4$, and right: $b = (\sqrt{5}-1)/2$. Top: restitution, and bottom: number of sub-impacts, against N.

Recall that the hysteretic force F_d is given in our model by

$$F_d = F_0(1+\theta),$$

where F_0 is the Hertzian contact force. Since on the rising curve we have $\theta = \theta_m + \beta = 3$, the stiffness K_h used in the hysteretic simulation was taken to be one-fourth of the original Hertzian stiffness of Eq. 3.20. As a result, F_d will be exactly equal to the Hertzian contact force F_0 during the initial compression phase of contact. While unloading, a hysteresis loop will be formed, with $F_d = 0$ for $\xi \leq 0$.

The restitution values obtained for this artificial case of $N = 0$ decreased slightly with increasing impact velocity, but were very close to 0.95 for all three cases.

Next, results of a simulation with impact velocity 1 m/s, with the above hysteresis model parameters, and with $N = 27$, are shown in Fig. 3.9. Multiple sub-impacts occur, as seen in earlier examples. The hysteretic force F_d shows many rate-reversals, including some that occur within a single sub-impact. The suitability of the hysteresis model for the present type of impact is thus demonstrated.

The results of a convergence study with increasing N, for the case with a hysteretic contact force are given in Fig. 3.10. It is seen there that convergence with increasing N is *not* improved with hysteretic dissipation in the contact.

3.3.5 Modal damping

Finally, we consider modal damping for the beam vibrations: see Eq. 3.18. The contact is now purely dissipationless Hertzian. A uniform damping ratio of $\zeta = 0.02$ is assumed for all the beam modes. The equations for the beam's modal coordinates now are

$$\mathbf{M}\ddot{\mathbf{a}} + \mathbf{C}\dot{\mathbf{a}} + \mathbf{K}\mathbf{a} = -F\{\phi(b)\},$$

where $\mathbf{C}$ is a diagonal matrix whose n^{th} diagonal element is $\zeta\omega_n$, where in turn $\omega_n^2 = \frac{EIn^4\pi^4}{\overline{m}l^4}$.

Results are shown in Fig. 3.11. It is clear that, at least for some purposes like approximately predicting the outcomes of such impacts for engineering simulations, a significant reduction in variability occurs by $N \approx 25$ for both b values. Thus, even a relatively light modal damping (such as 0.02) has a strong regularizing effect on the impact, and speeds up convergence with increasing N.

In the next section, we study this improved convergence in greater detail.

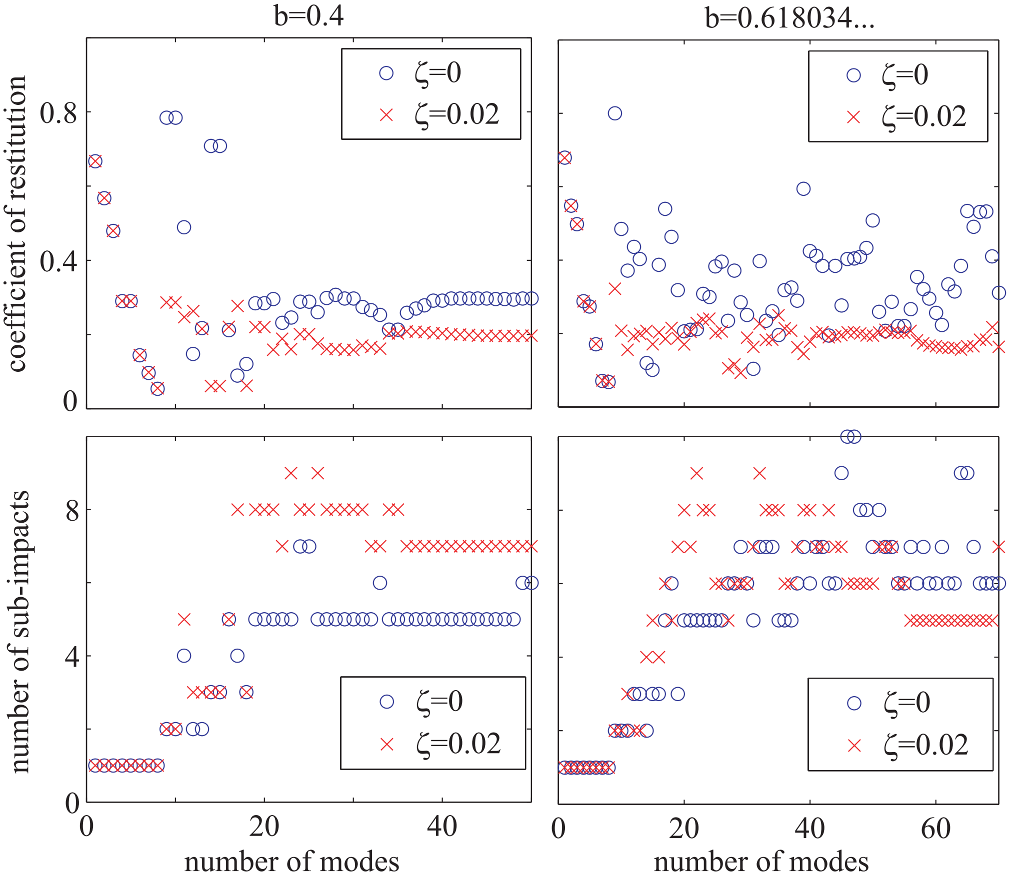

Figure 3.11: With modal damping (red crosses) and without (blue circles). Left: $b = 0.4$, and right: $b = (\sqrt{5} - 1)/2$. Top: restitution, and bottom: number of sub-impacts, against N. Convergence of a sort is seen for increasing N; certainly the variability is greatly reduced.

3.4 Further simulations

3.4.1 Role of modal damping in improved convergence

See Fig. 3.12. The ball-beam motion during contact $(y_b, \dot{y}_b, z_b, \dot{z}_b)$ are plotted for $\zeta = 0$ and $\zeta = 0.02$, for 40 modes and $b = 0.618034$.

The uppermost subplot shows displacements against time of the ball as well as the beam's contact point, for both ζ values; recall that the $\zeta = 0$ case is expected to resemble the results presented in Fig. 3.3 above. It is seen that the net restitution is significantly different for the two cases, $\zeta = 0$ and $\zeta = 0.02$. In this specific example, the final sub-impacts differ dramatically for the damped and undamped cases.

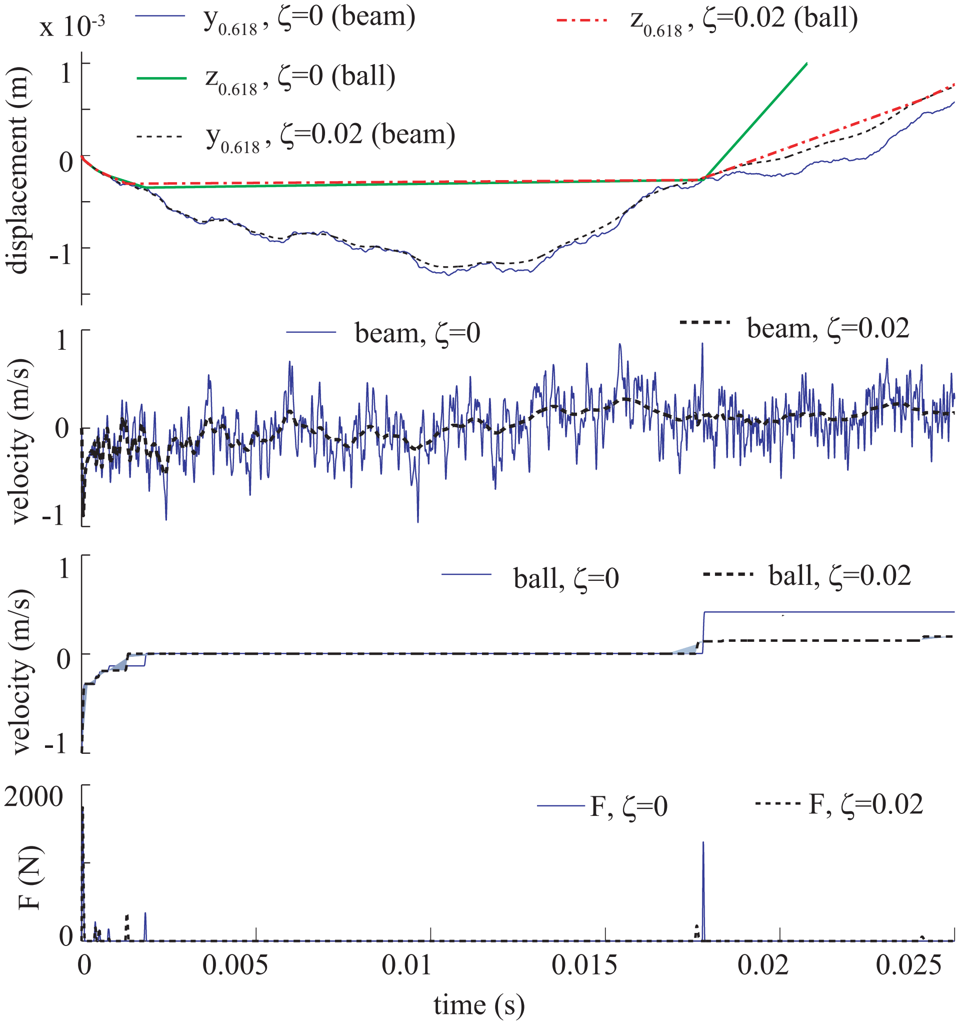

Figure 3.12: Ball-beam motion with $N = 40$ during impact at $b = (\sqrt{5}-1)/2$ for damping ratios $\zeta = 0$ and $\zeta = 0.02$. In these two particular simulations, the final sub-impacts differ dramatically; other pairs of simulations show differences in details, but the qualitative effect of light modal damping is the same.

The next subplot shows the velocity of the contact point on the beam, and here the role of modal damping is clearly seen. There is enough time in the net impact interaction for the higher mode responses to decay to negligible magnitudes, even for a small damping ratio of $\zeta = 0.02$. However, for $\zeta = 0$, the higher mode oscillations persist indefinitely, and it is clear that a random-like effect on restitution might arise in such cases. This issue can also be clearly seen in a plot of modal energies for a damped versus undamped beam. The higher modes damp out quickly for the damped beam leading to less scattered results. For example, see Fig. A.2 in Appendix A.3. Note that the pure impulse response of undamped Euler-Bernoulli beams is known to be complex [63], and the high modal content in the undamped response just reflects that complex behavior. With viscous and hysteretic contact dissipations too, the rapid beam oscillations persist.

The third subplot shows the velocity of the ball for the two cases, and it is seen as expected that there are quick transitions followed by relatively long phases of free flight, all within one single macroscopic impact.

Finally, the lowermost subplot shows the contact force histories for the two cases.

Overall, the qualitative picture which emerges is that, with several brief sub-impacts spread over a relatively long period, the higher mode responses decay quickly between sub-impacts and lead to better convergence (or at least, less variability) with increasing N.

3.4.2 Some other parameter values

It remains to check that the qualitative behavior observed persists for some reasonable (not too small) range of parameter values. To this end, we now vary two of the parameters, namely the ball impact velocity $\dot{z}_b$ and the ball diameter, in a few final simulations.

Figure 3.13 shows results for different impact velocities, namely 0.5, 0.25 and 0.1 m/s, with and without modal damping, and $b = 0.618034$, and all other parameters unchanged. The ball diameter is kept as earlier (3 cm), $\zeta = 0.02$ and the beam parameters are unchanged. We see that the restitution shows distinctly less variation against N with modal damping present as opposed to absent, although for the 0.25 m/s case the convergence appears relatively a little slower. There is no doubt that the presence of small modal damping regularizes the impact outcome significantly.

Figure 3.14 shows results for impacts at a velocity of 1 m/s, with balls of diameters 4 cm and 2 cm (and the Hertz contact stiffness adjusted appropriately), for $\zeta = 0$ and $\zeta = 0.02$, and $b = 0.618034\cdots$. Interestingly, for the ball diameter of 4 cm, the behavior is qualitatively similar to the 3 cm case except that the convergence is more convincing. In contrast, for a ball diameter of 2 cm, there is just one single impact both with and without

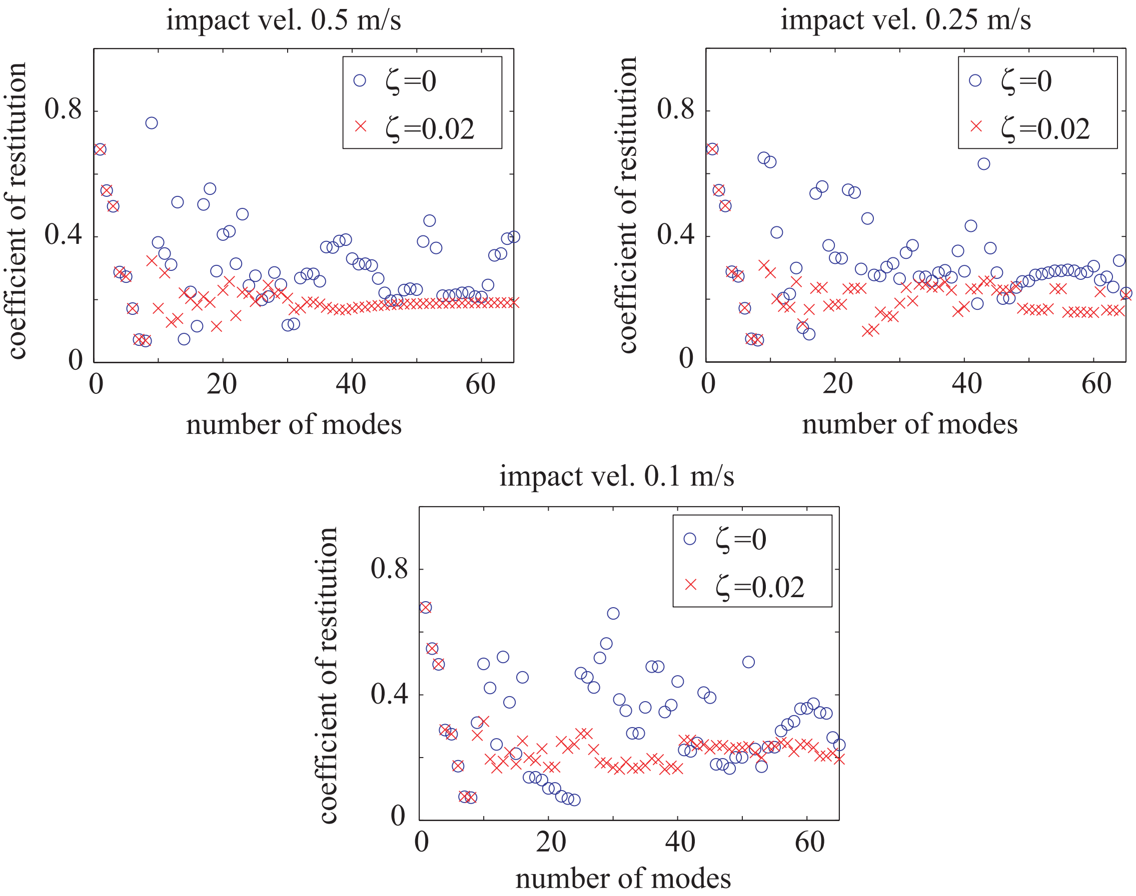

Figure 3.13: Restitution against N for different impact velocities, with $b = (\sqrt{5} - 1)/2$, for $\zeta = 0.02$ (red crosses) and $\zeta = 0$ (blue circles).

damping, results are regular in both cases, and the modal damping essentially plays no role at all. In other simulations with the 4 cm ball we have observed that the converged value of the restitution changes visibly (though not dramatically) with contact location b. A numerical study of this variation in restitution for b between 0.6 m and 0.62 m is given in Fig. 3.15 for completeness.

Qualitatively, for the smaller ball (2 cm diameter), there is only one impact and the behavior is regular. For extremely massive balls, the beam would begin to behave like a massless spring, and again the behavior would be regular. In an intermediate regime as seen for the 3 cm and 4 cm balls, it is possible to have many sub-impacts, and in this regime light modal damping has a strong regularizing influence.

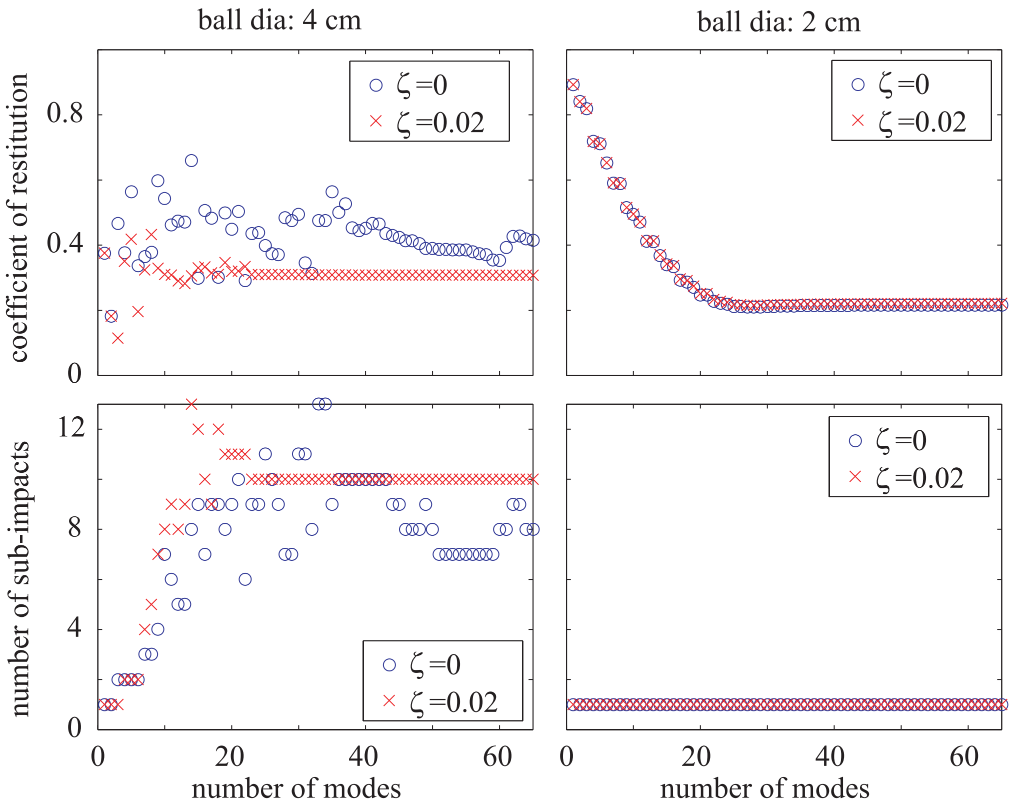

Figure 3.14: Impacts with ball diameters, of 4 cm and 2 cm at $b = (\sqrt{5} - 1)/2$, for $\zeta = 0.02$ (red crosses) and $\zeta = 0$ (blue circles). Top: restitution, and bottom: number of sub-impacts, against N.

3.5 Concluding remarks

The dynamics of impact between a chunky object like a ball and a slender object like a beam can involve several sub-impacts within each macroscopic impact due to vibrations in the beam. In a dynamic simulation of such impact, retention of insufficiently many modes in the model may lead to highly inaccurate predictions. For example, with dissipation-free Hertzian contact as seen in Fig. 3.4, as we vary the number of modes retained between 30 and 40, the computed coefficient of restitution can vary by a factor of 6, between about 0.1 and 0.6. Such uncertainty (caused by unsuitable modal truncation) in the outcome of an otherwise deterministic calculation is clearly undesirable.

In this context, in the present chapter we have studied the interplay between dissipation and modal truncation in such ball-beam impacts. In particular, we have found that

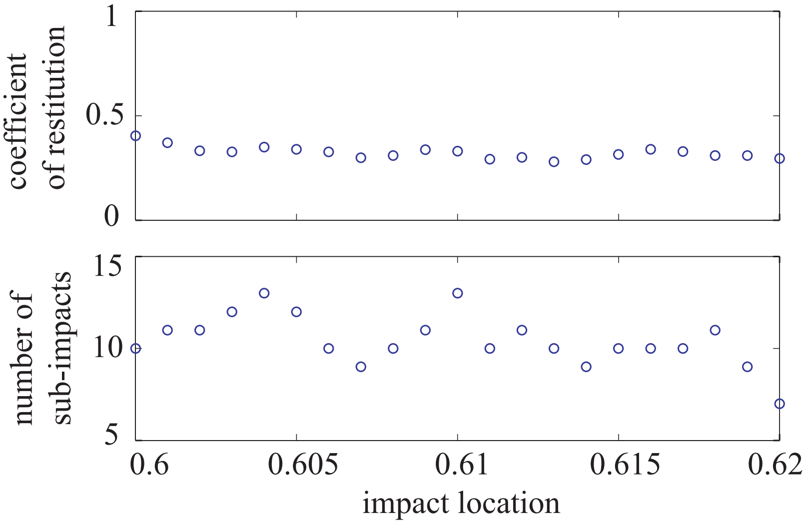

Figure 3.15: See section 3.4.2. Impacts with a ball diameter of 4 cm, for different contact locations b, with $\zeta = 0.02$ and $N = 40$. Top: restitution, and bottom: number of sub-impacts, against b.

introduction of contact dissipation (whether viscous or hysteretic) has little effect on the observed variability of computed outcomes against number of modes retained. In sharp contrast, we have found through detailed simulations that introduction of even rather light (2 percent) modal damping makes the variability much smaller, and leads to convergence of a sort (though not precise mathematical convergence within the numbers studied) with increasing numbers of modes retained. In particular, the computed restitution settles down to a variability within several percent (as opposed to a factor of 6) with 2 percent modal damping and more than about 25 modes retained, for the ball size and impact velocities studied. The results remain qualitatively the same for some significant range of parameter values, such as steel balls with diameters from 3-4 cm, and impact velocities from 0.1-1.0 m/s, for a simply supported steel beam of length 1 m and mass about 1 Kg. For significantly smaller balls, such as diameter 2 cm, results are inherently less variable, and the modal damping plays no significant additional role.

The key physical phenomenon responsible for the regularization of impact outcomes with even light modal damping is the rapid decay of higher-mode oscillations during periods of free flight, between subsequent sub-impacts, as shown in Figs. 3.12. In fact, the main qualitative understanding obtained in this chapter is summarized nicely by that one figures. We believe that this insight is generally relevant to vibration-dominated impacts between one compact and one slender body. However, the quantitative details of convergence, like precise number of modes needed, will change from system to system.

We close this chapter with comments on two modeling issues.

The first comment is on the adoption of the Euler-Bernoulli beam model. The Euler-Bernoulli beam neglects rotary inertia and deformation due transverse shear. We retain about 30 to 40 modes in the simulations. For a beam under impact and with many modes retained, rotary inertia and shear may play a role for very high modes. However, there are many studies on the behavior of an Euler-Bernoulli beam under impact (see [37]), and in these studies some lower frequency aspects of the solution are expected to remain valid. Also, we emphasize that the use of a large number of modes should be looked upon as a solution method, after the governing PDE has *already been adopted*. In other words, when we have already decided to neglect rotary inertia and shear, we have arrived at a PDE, which is called the "Euler-Bernoulli beam". Solutions of that PDE may use a large number of modes, and there is in principle no contradiction.

The second comment is on the number of modes required. For ease of a reader who may want to estimate the number of modes required for an acceptable solution, we suggest the following steps. For our considered ball-beam impact problem, we can hold the beam immobile (zero modes, just Hertz contact), and calculate the contact duration. We can then clearly cut off all beam modes whose time periods (inverse of natural frequencies) are smaller than the contact duration obtained with zero modes. However, by this approach that number turns out to be very large, (about 70). With this large number, i.e. 70, as an approximate guideline we may estimate that the first 30 to 40 modes may be sufficient in the presence of small damping. We acknowledge that giving a general prescription for all kinds of systems may be difficult as the variety of systems is large, and the prescription given here applies to slender beam like bodies impacted by chunky or compact bodies.

Chapter 4

Finite-beam impact: Detailed simulations and restitution values

The aim of this chapter is to present detailed numerical simulations of vibration-dominated impacts between solid Hertzian spheres and finite beams.

We will consider both uniform and stepped, simply-supported and cantilever beams. There is no dissipation at the contact and the beams are lightly damped, following the observations of chapter 3.

It is well recognized that the coefficient of restitution is not a fundamental property of a pair of materials or even a pair of objects. Restitution is a useful parameter in impact models, and yet also one that is not fully understood, that shows variation depending on impact configuration or colliding body type, and that deserves further case studies so that clearer insights into its nature and variability can be obtained.

We distinguish here between the restitution as a ratio of separation to approach velocities at the end of the contact phase while the bodies are *still vibrating*, as examined in [6, 13, 37, 38], as opposed to a similar ratio considering only the rigid-body motions (i.e., after vibrations have decayed to negligible levels, or when large enough overall motions are examined such that small superimposed vibrational displacements are not important [19]). The latter ratio may be called the *net restitution*, and is of primary interest in simulations of large overall motions of stiff bodies that vibrate briefly after impact.

We now discuss a few relevant articles on vibration-dominated impact models from a net-impulse or net-restitution viewpoint, which also include those where modal decomposition was used. The early articles [6, 37] and several other similar ones discuss a generalized momentum balance method for intermittent motion in flexible multibody systems. Therein, the authors show that, on incorporating sufficiently many assumed beam modes and a coefficient of restitution, and using a matrix formulation, it is possible to describe a single impulsive interaction in flexible body impacts. Note that, since the single contact may lead to subsequent subimpacts, the impact simulation may not end with one computed impulse. Various studies have presented experimental validation with the aforementioned approach [23], and considered plastic deformation and an equivalent restitution [13, 26]. The recent article [81] presents further developments along the same line of thought.

The most important general paper that discusses impact outcomes for a flexible body, that we know of in this area, is [26]. In that paper, three asymptotically limiting regimes are used to identify important nondimensional parameters that govern the net outcome of impacts of a compact body on an extended flexible body. These limiting regimes are (i) an extremely light impactor, such that the flexible body behaves like a half space, (ii) an extremely heavy impactor, such that the flexible body acts like a massless spring, and (iii) a short time impact on a large flexible structure, such that the flexible structure (typically a beam or a plate) acts like an infinitely large object, with no waves reflected back. In regimes that are in between these asymptotic limits, a moderate amount of additional variability exists in the outcome, but enough is known to serve, e.g., design needs. Predictions and validations for net restitution levels are, however, not shown in [26].

Another key paper in the area of modeling and predicting the net restitution in a vibration dominated impact is [19], where an analysis based on energy partitioning is developed to explain and match the experimental results for a tilted rod falling on a massive object [14]. Finally in simulations of ball-beam impacts [78], it was noted that while there are other effects close to boundaries, the restitution level for some mass ranges is roughly constant for impact locations far from the boundaries.

However, a systematic, quantitative and detailed study as in this chapter, although straightforward, is not available in the literature as far as I know. In subsequent chapters these numerical results will be used to develop and validate a novel modeling approach.

Here we consider solid spheres of six different sizes, colliding at 25 impact locations, on each of four different beam geometries with different boundary conditions. Similar to chapter 3, we use modal expansion for the beam and a Hertzian spring for the contact interaction. We compute detailed solutions of the ODEs and primarily report net restitution values.

4.1 Physical model and equations of motion

The equations of motion are similar to those used in chapter 3. However, details like actual mode shapes differ. To make the chapter self-contained, the equations are briefly presented afresh. Readers familiar with such equations may move to section 4.2.

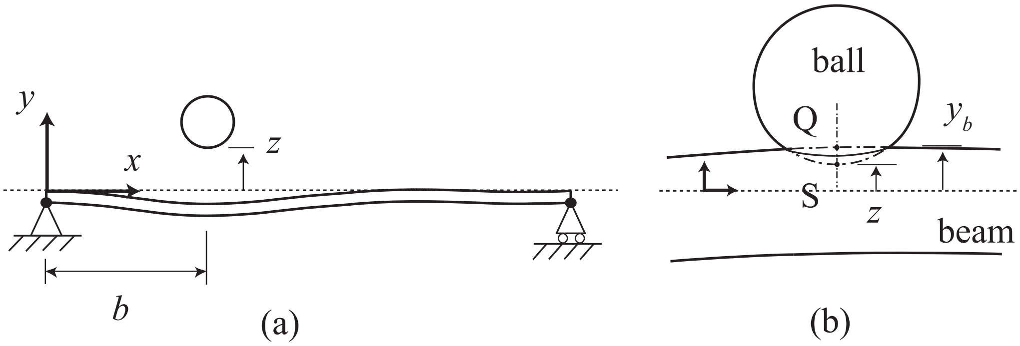

Figure 4.1: (a) Lateral impact of a compact body on an Euler-Bernoulli beam at $x = b$. The displacements of the beam and ball are $y(x,t)$ and $z(t)$ respectively, positive upwards. (b) The ball-beam contact. Solid lines show the actual configuration at contact. S and Q are the notional contact points on the undeformed ball and beam respectively. A contact force exists only if $y_b - z > 0$.

See Fig. 4.1. We consider the transverse impact of a ball on an initially stationary Euler-Bernoulli beam. The beam may have various boundary conditions (cantilever/built-in/fixed, pinned, free, or some other). The beam is lightly damped, and vibrates during and after impact. All displacements during impact are small. Contact between the ball and beam is Hertzian, and occurs at $x = b$. We neglect (i) gravity, (ii) vibrations in the sphere, and (iii) friction at the contact. There is no dissipation in the Hertzian compliance model. It may be noted that introduction of contact dissipation may not change results much, going by chapter 4.

In Fig. 4.1, the dotted line along the beam's undeformed surface denotes our reference line. The displacement (upwards) of the beam from the reference line is taken as $y(x, t)$. The distance (upwards) of the notional point of contact of the ball from the reference line is taken as $z(t)$. Contact occurs when $y(b, t) - z(t) \geq 0$.

The impacting ball has mass m and is taken for simplicity to be a solid uniform sphere of radius r. It will be clear below that we actually only use the total mass m and the Hertz contact stiffness k_H, so the ball is notional. Other impacting body shapes are not really excluded.

The beam has a length l and density ρ; its cross-sectional area is A and mass per unit length is $\overline{m}$, both of which we assume for simplicity are piecewise constant. The beam cross-section's area moment of inertia is I, which we also assume for simplicity is piecewise constant (e.g., we consider stepped beams). We assume that both the bodies have the same elastic modulus E, but only for computing the Hertz contact stiffness k_H. Our assumption that $\overline{m}$, A and I are piecewise constant is merely to allow us to easily compute a large number of natural frequencies and mode shapes; in principle spatially variable $\overline{m}$, A and I could be included as well.

The ball hits the beam at $x = b$ with a vertical velocity $\dot{z}(t)$ or $v_{\mathrm{i}} < 0$. We take $v_{\mathrm{i}} = -1$, and study a parameter range where the dependence of restitution on impact velocity is small[1]. The beam vibrates upon impact. After one or more contact interactions, the body rebounds with a velocity of $v_{\mathrm{f}} > 0$, never to collide again. This final rebound velocity is the effective or actual coefficient of restitution, since $v_{\mathrm{i}} = -1$.

The equation of motion of an undamped beam with a concentrated arbitrary downward

---

[1] We have separately verified that for a range of sphere masses, changing the impact velocity up or down by a factor of 15 has only a small effect on the restitution, see Fig. 4.3.

force F at $x = b$ is

$$(EIy'')'' + \rho A\ddot{y} = -\delta(x-b)\,F, \tag{4.1}$$

where primes and dots denote partial derivatives with respect to position x and time t respectively.

For our impact problem, F is a time-varying contact force. We will be interested in $\int_0^{\mathrm{tc}} F dt = P$, where P is the net-impulse, and "tc" is the contact duration. For the colliding sphere, on which the contact force acts upwards,

$$m\ddot{z} = F. \tag{4.2}$$

Initial conditions are $y(x,0) = 0$, $\dot{y}(x,0) = 0$, $z(0) = 0$ and $\dot{z}(0) = -1$. Regardless of the possibly complex vibrational dynamics with one or more subimpacts that determine the temporal details of $F(t)$, direct integration of Eq. (4.2) gives[2] $m(\dot{z}_f - \dot{z}(0)) = P$.

We will tackle Eq. (4.1) using modal expansion and direct numerical integration after introducing a small amount of modal damping. To this end, we write

$$y(x,t) \approx \sum_{i}^{N} a_i(t)\phi_i(x), \quad i = 1..N, \tag{4.3}$$

where $a_i(t)$ is the modal coordinate corresponding to the i^{th} mode $\phi_i(x)$, N is the number of modes to be retained, and the determination of the mode shapes and corresponding natural frequencies is a routine calculation and not described here in detail[3]. The modes $\phi_i(x)$ are mass-normalized, i.e., they satisfy

$$\int_0^L \rho A\phi_i(x)\phi_j(x)dx = \delta_{ij}, \tag{4.4}$$

---

[2] This is a simple special case of the idea that, even in the presence of vibrations, the effect on the rigid body motion can be computed using the net impulse, and rigid body impact models remain useful.

[3] Two procedural points are noted: (i) For computing eigenvectors, stepped beams require three continuity and one jump conditions at the step. (ii) For higher modes and their natural frequencies, there can be exponentially large terms that almost cancel out, and some asymptotic approximations are useful to avoid catastrophic cancellation of significant digits. We used high-precision Maple calculations to cross-check our simplified expressions used in Matlab.

where $\rho A = \overline{m}$ (piecewise constant) denotes the mass per unit length of the beam; and where δ_{ij} is the Kronecker delta, equal to one if $i = j$ and equal to 0 otherwise. The velocity of any point on the beam is

$$\dot{y}(x,t) = \sum_{i}^{N} \dot{a}_i(t)\phi_i(x), \quad i = 1..N.$$

We now proceed to write Lagrange's equations. The kinetic energy (KE) of the vibrating structure is $KE = \frac{1}{2}\sum_{i}^{N} \dot{a}_i(t)^2$ due to use of the normal modes. The potential energy is known to be of the form $PE = \frac{1}{2}\sum_{i}^{N} \omega_i^2 a_i(t)^2$, where ω_i is the natural frequency of the i^{th} mode. The equations of motion for the modal coordinates $a_i(t)$, in the absence of damping, are

$$\ddot{a}_i + \omega_i^2 a_i = -\phi_i(b)F, \quad i = 1 \ldots N. \tag{4.5}$$

Introducing uniform light modal damping, we write

$$\ddot{a}_i + 2\zeta\omega_i\dot{a}_i + \omega_i^2 a_i = -\phi_i(b)F, \quad i = 1 \ldots N, \tag{4.6}$$

where we have used $\zeta = 0.02$ in our study uniformly (see [56] for motivation and discussion). Equation (4.6) will be solved along with Eq. (4.2) for the impacting body, wherein the contact force F will be taken as Hertzian,

$$F = k_H \xi^{3/2}, \quad \xi = \begin{cases} y(b,t) - z(t), & y(b,t) > z(t), \\ 0 \quad \text{otherwise.} \end{cases} \tag{4.7}$$

Finally, in Eq. (4.7), k_H is given by [1]

$$k_H = \frac{2E\sqrt{r}}{3\left(1-\nu^2\right)}, \tag{4.8}$$

where r is the local radius of the impacting body, the beam's contacting surface is flat, the impactor and beam are of the same material, E is Young's modulus and ν is Poisson's ratio. k_H, in principle, can be a free parameter. In that case, as the contact stiffness k_H varies, the number of modes actively participating in the impact will change.

4.2 Numerical simulations

In our simulations below, material parameters match steel. In SI units, $E = 2 \times 10^{11}$, $\nu = 0.3$, $\rho = 7800$. A ball mass of $m = 0.0638$ Kg or 0.025 m diameter gives, e.g., $k_H = 1.638 \times 10^{10}$ $\mathrm{Nm}^{-3/2}$ by Eq. (4.8).

Four different beams are considered, as shown in figure 4.2.

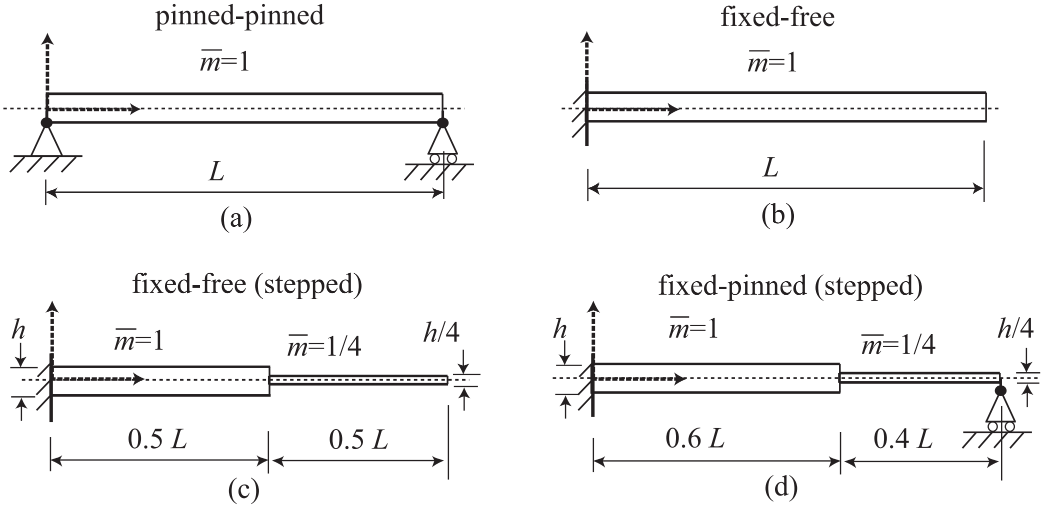

Figure 4.2: Four beams considered. Where $\overline{m} = 1$, the beam cross section is square. In slimmer portions with $\overline{m} < 1$, the width is kept the same and the thickness is lowered.

We numerically integrate $N + 1$ equations of motion (see Eqs. (4.6), (4.2) and (4.7)) using Matlab's stiff ode solver "ode15s". Variation of rebound with impact velocity is shown in Fig. 4.3. We have chosen $N = 40$ and $\zeta = 0.02$ after some initial convergence studies: see Fig. 4.4, which shows one such. As the contact stiffness k_H varies, the number of modes actively participating in the impact will change. It is noteworthy (as in Fig. 4.4, bottom right) that near the free end of the beam the number of impacts can be quite large, but even a small modal damping regularizes the interaction and produces a more rapidly convergent modal expansion. The number of subimpacts may change a lot while the net restitution

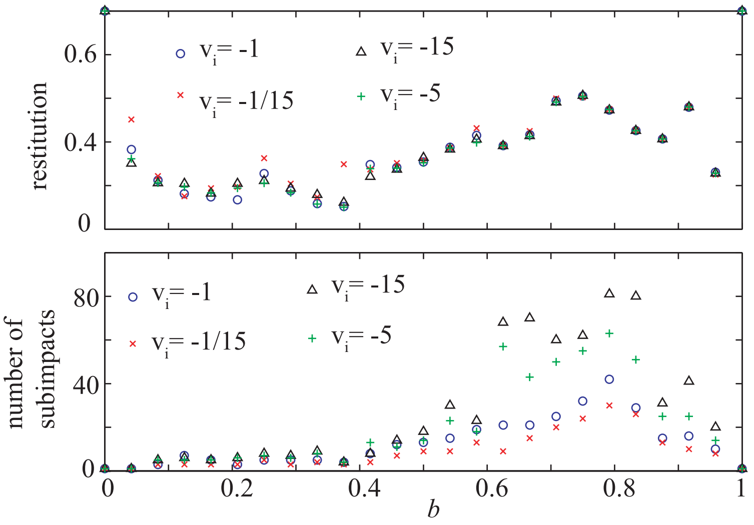

Figure 4.3: Variation of restitution (top) and number of subimpacts (bottom) against v_i at several impact locations on the stepped cantilever beam, with sphere mass $m = 0.147$ Kg. $N = 40$.

does not change much. This is because many of the subimpacts are very gentle. A large number of gentle subimpacts is dynamically well approximated by a sustained contact.

While convergence is not perfect for $N = 40$, it is reasonably good (see also [56]). Retaining even higher modes leads to high natural frequencies and correspondingly slower and more challenging numerical simulation (for example, for a simply supported uniform beam, the 40th natural frequency is 1600 times higher than the first one). Additionally, if we retain extremely high modes, with extremely small modal amplitudes, then their contribution may become comparable to other neglected effects like contact imperfections and asperities, plastic yielding at the contact location, shear effects and other deviations from Euler-Bernoulli beam theory near the contact location, and imperfections in boundary conditions. For these reasons, we proceed with $N = 40$.

See Fig. 4.5 for some representative results. Numerically obtained solutions are shown for a fixed-pinned, stepped beam, impacted independently at four locations, $b = 0.375$, 0.583, 0.75, and 0.917. Multiple sub-impacts are seen. High frequencies are excited, and contact events are complicated.

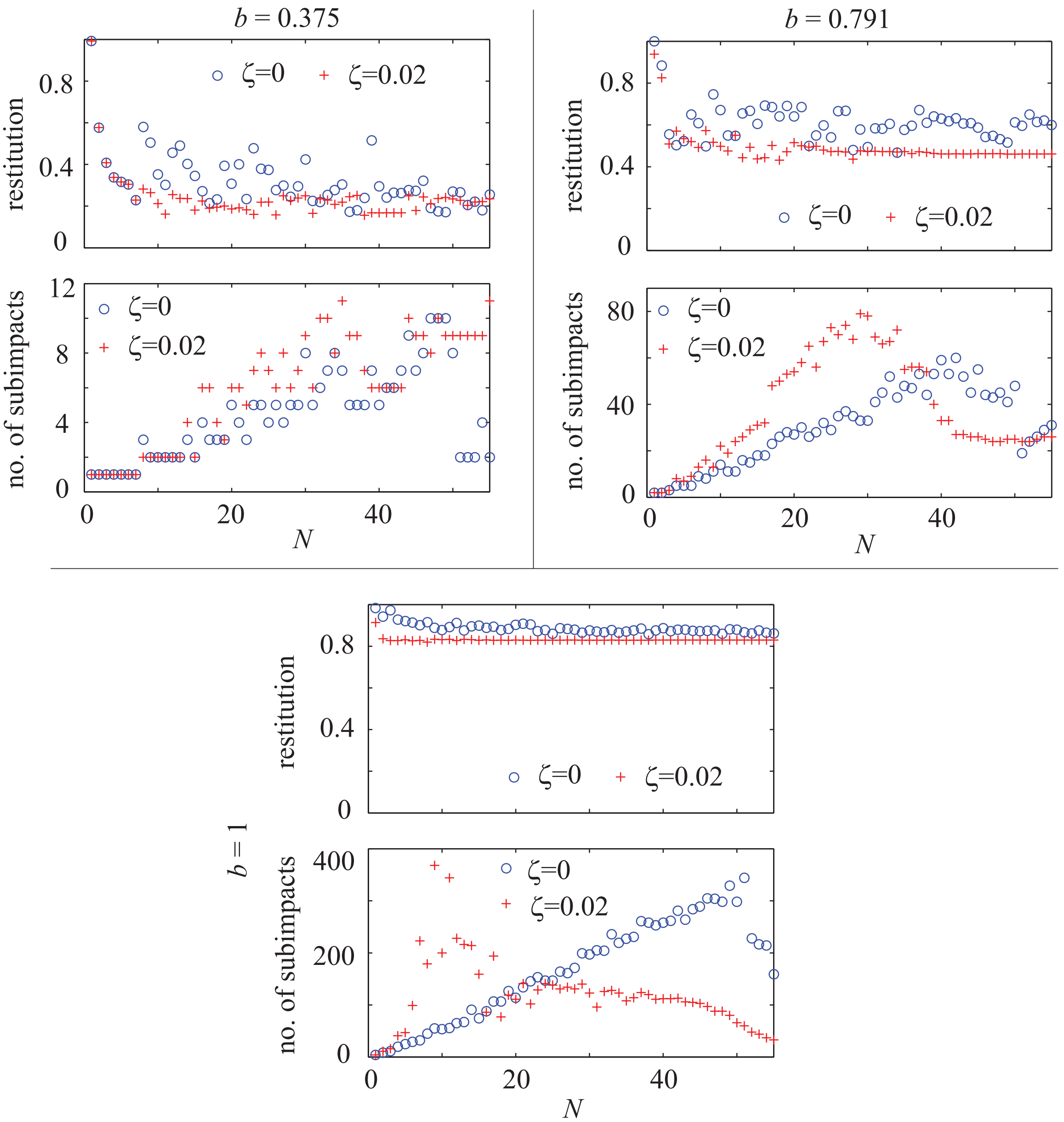

Figure 4.4: Variation of restitution and number of subimpacts against N at three b's on the stepped cantilever beam, with sphere mass $m = 0.147$ Kg. Compare results for $\zeta = 0$ (blue circles) and $\zeta = 0.02$ (red pluses). Convergence is more rapid where restitution is higher, because small changes in energy can cause large relative changes in small restitution values. Reasonable convergence is achieved for $N \approx 40$.

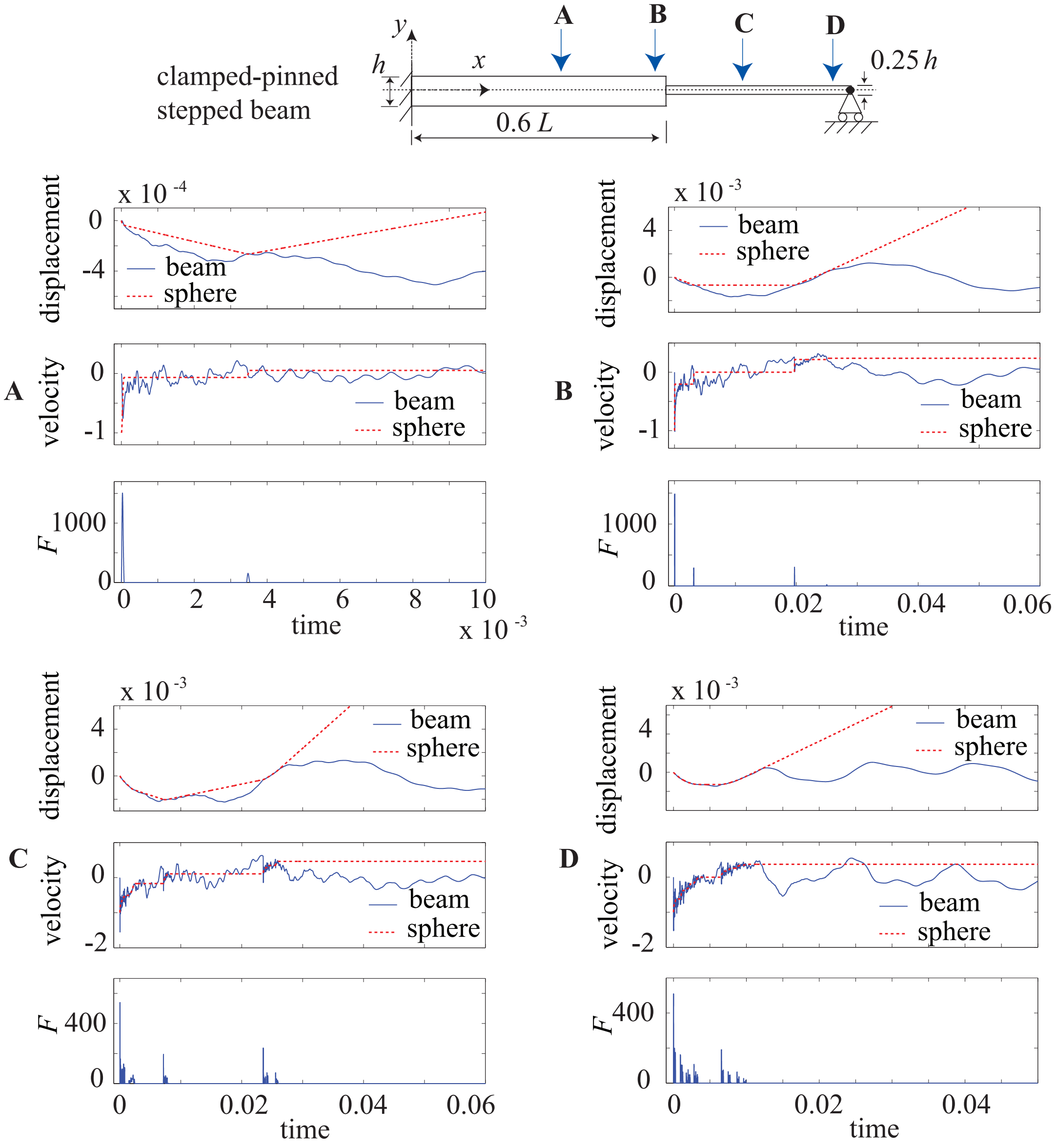

Figure 4.5: Numerical simulations. A sphere ($m = 0.0638$) strikes a stepped beam ($L = 1$) at $b = 0.375$ (A), $b = 0.583$ (B), $b = 0.75$ (C), and $b = 0.917$ (D), as shown in the schematic at the top. For each case A, B, C and D, there are three subplots as follows. Top: displacements $y(b)$ and z against t. Intersection of the blue (beam) and the red (sphere) lines indicates contact. Middle: velocities $\dot{y}(b)$ and $\dot{z}$ against t. When there is no contact, $\dot{z}$ is constant. The final $\dot{z} = v_\mathrm{f}$ equals the restitution. Bottom: F against t. Multiple sub-impacts are seen.

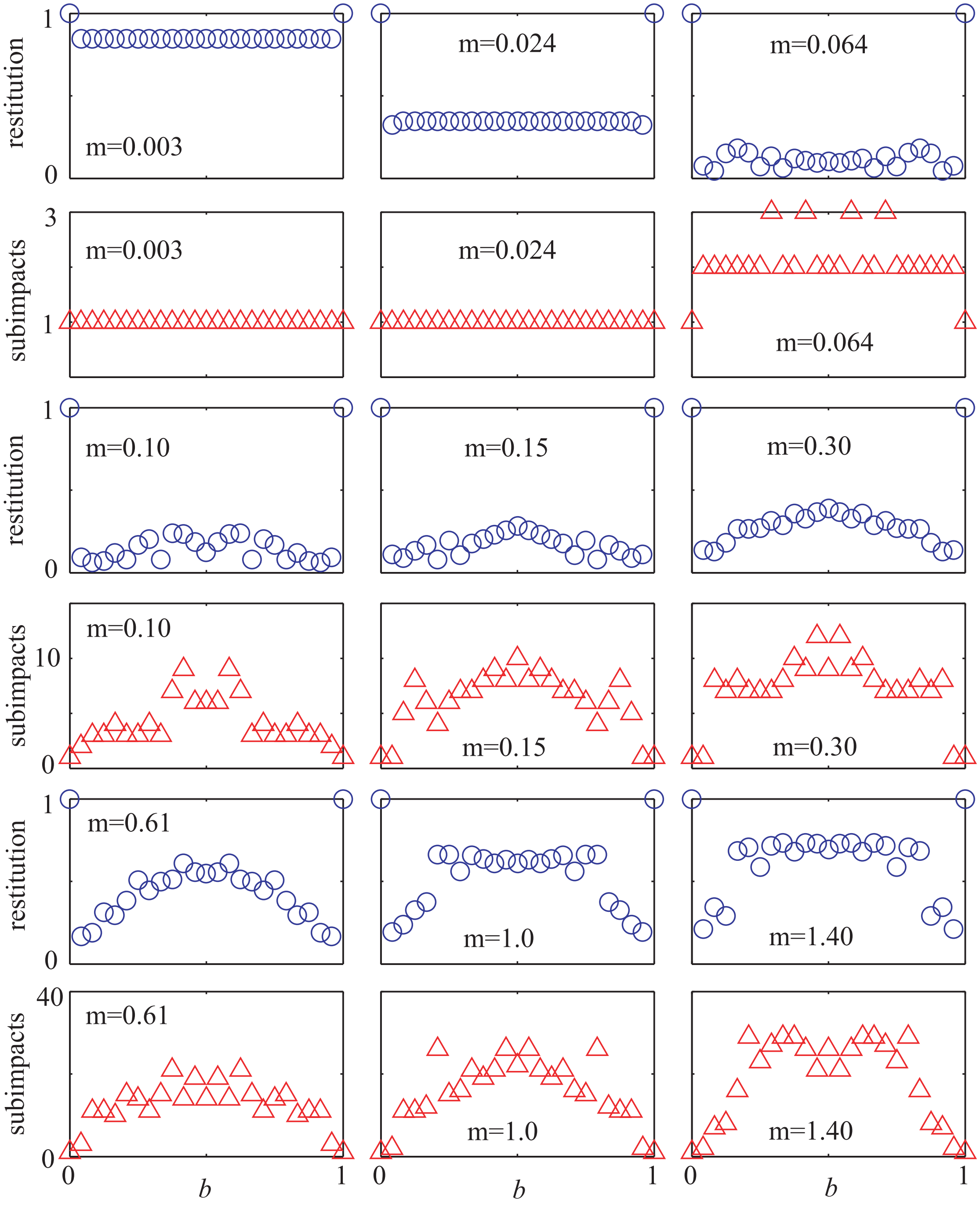

Figure 4.6: Restitution and number of contacts for impacts on uniform pinned-pinned beam (see Fig. 4.2 a), for different m and b.

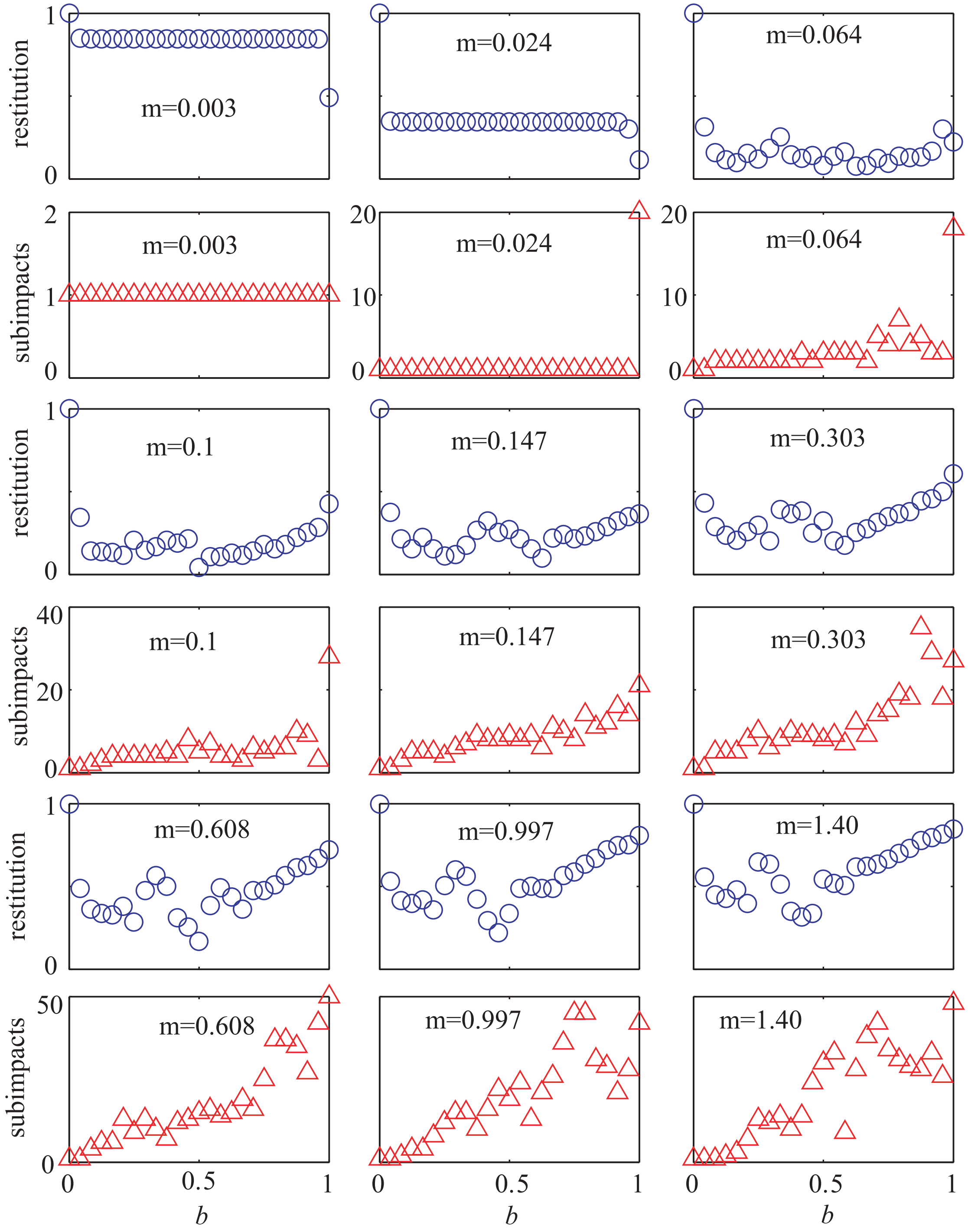

Figure 4.7: Restitution and number of contacts for impacts on uniform fixed-free beam (see Fig. 4.2 b), for different m and b.

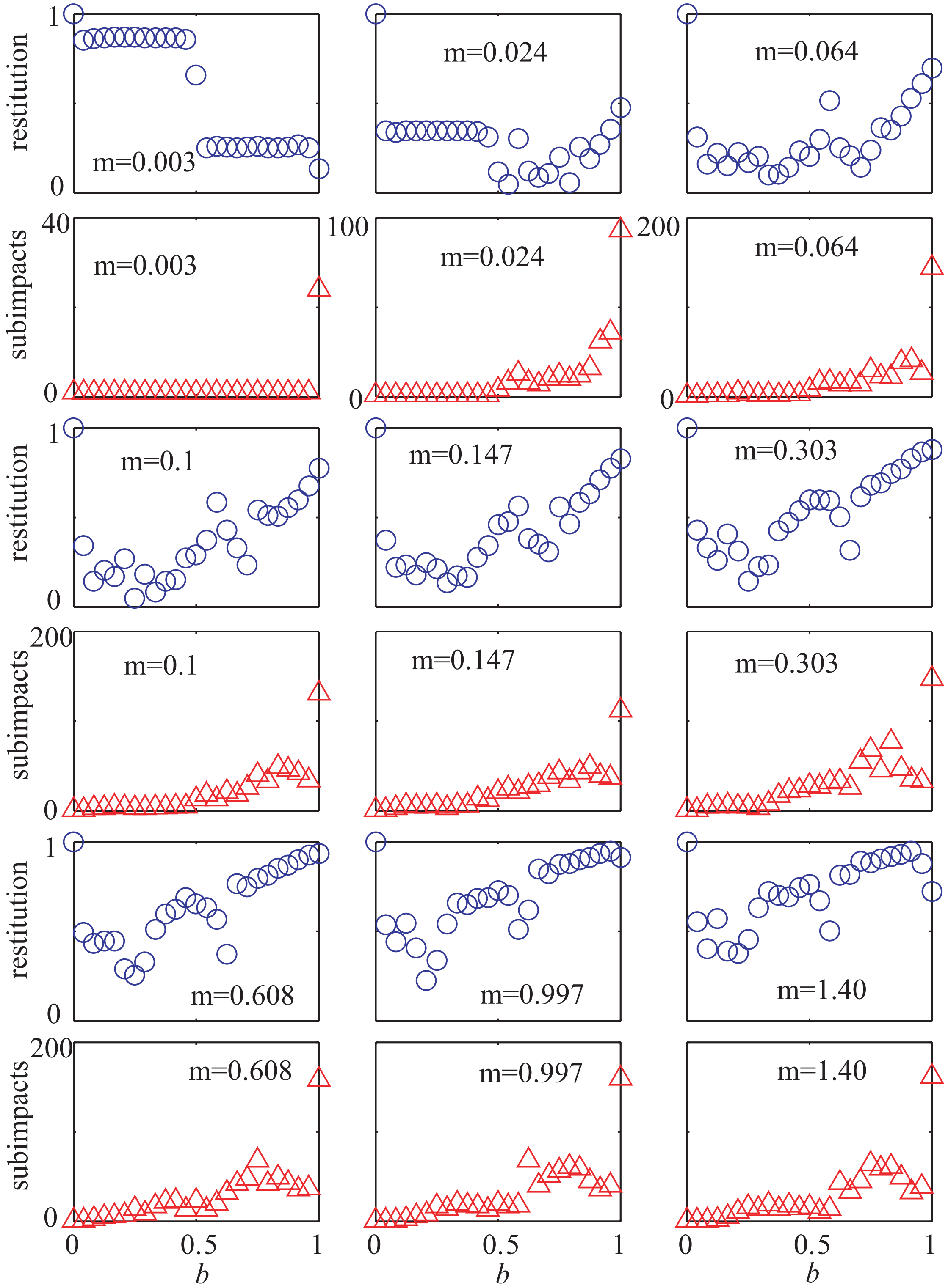

Figure 4.8: Restitution and number of contacts for impacts on stepped fixed-free beam (see Fig. 4.2 c), for different m and b.

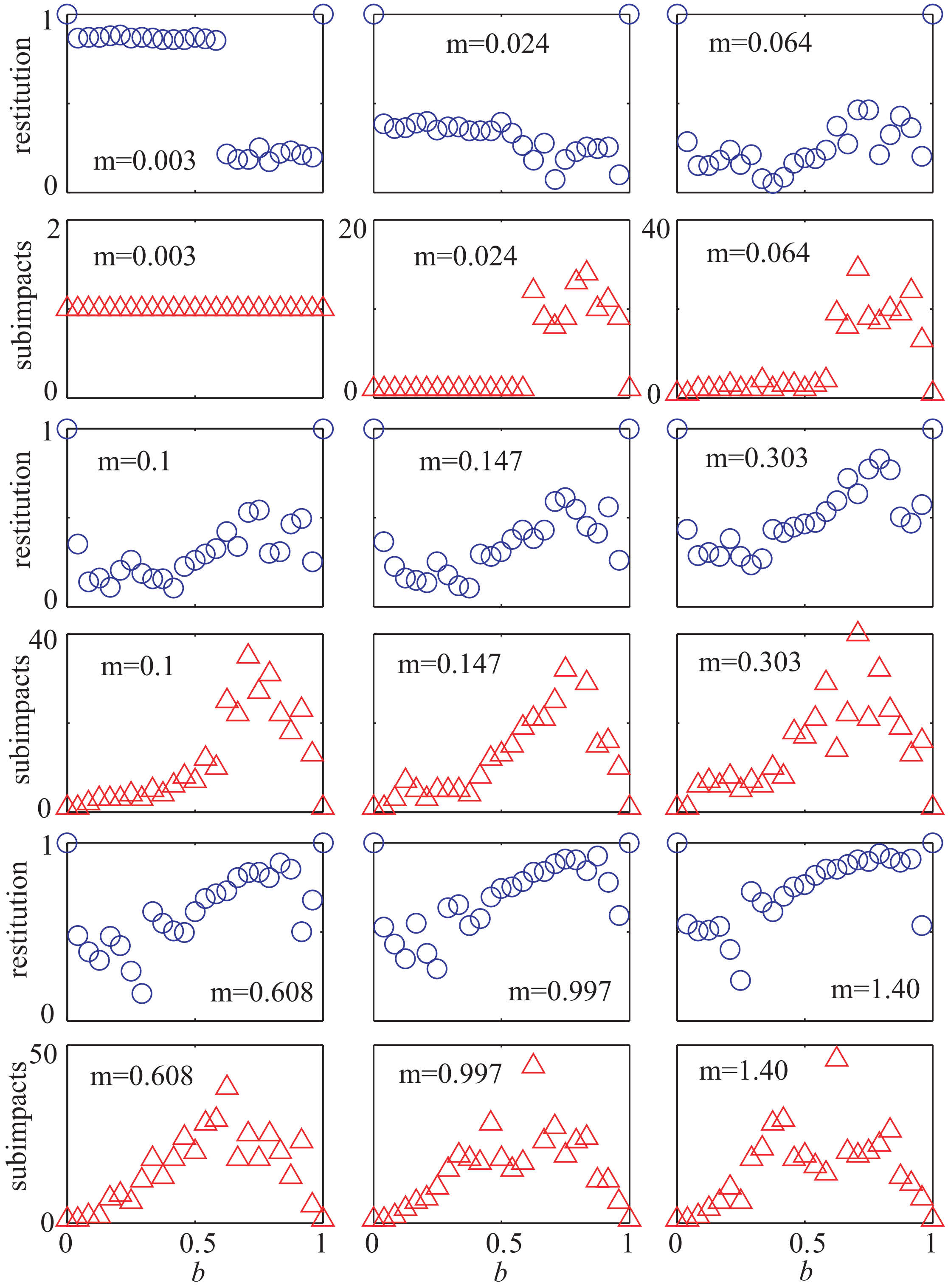

Figure 4.9: Restitution and number of contacts for impacts on stepped fixed-pinned beam (see Fig. 4.2 d), for different m and b.

Detailed restitution and number of subimpacts plots are given for the four beams, in Figs. 4.6, 4.7, 4.8 and 4.9.

A few general trends are observed. For very small m, v_{f} is high and there is a single contact event. For slightly higher m, the number of sub-impacts increases (indicating significant beam vibrations), the dynamics is richer, there is more variability, and v_{f} is low. As m increases further, v_{f} increases again. This is because energy comes back to the sphere through subsequent impacts, and also the beam begins to behave somewhat like a spring. For stepped beams, since the compliance of the thinner portion is higher, greater rebound is seen from those locations (the impacting mass is, relatively speaking, larger). Near free ends, a general rising trend in v_{f} is seen. There is a sudden rise in restitution very close to pinned or fixed ends.

It may be noted in the modal expansion that there is a singularity at $b = 0$ in that no modes are excited there. But if the contact is at $b = \epsilon$, where ϵ is a small positive number, then essentially every mode is excited. In reality it is not exactly a discontinuity but a region of rapid change in behavior. However, in order to avoid complexities of such a rapid change, we do not take b extremely small and have restricted ourselves to 25 equally spaced impact locations. Therefore the smallest nonzero value of b is $0.04166\ldots$.

We now comment briefly on the correctness of our simulation results. For comparison and better understanding, we have also simulated the ball-beam impact for a uniform cantilever beam using the Finite Element Method (FEM). We have compared the rebounds obtained using modal analysis and FEM. For uniformity (in number of modes present), we discretized the beam into 20 beam elements (40 dof). A very good match is observed: see Fig. A.3 in Appendix A.4.

Having satisfied ourselves that our results are accurate, the rather significant variation of restitution values with b is still surprising for some readers. The reason for this variation, especially for the cantilever beams, can be seen in Figs. 4.10 and 4.11. The subfigures show the simulated ball and beam displacements with time. The compliances of the beams increase as we move away from the fixed end, more so when the beams' cross-section are reduced at the step. Very coarsely, we see that for the larger b's, the magnitudes of the displacements of the beam-contact-point increase, the impactor's rebound velocities after the first overall contact event decrease, and as such (more than one) subsequent impacts occur. We see that a large number of grazing bifurcations and associated complications may occur (see, e.g, [35, 36]). The variability in restitution is therefore inherent to the system.

Another point worth mentioning here is that the percentage variation in the restitution value is significantly larger when the restitution itself is smaller. This is because of physical reasons, e.g., if the restitution is 0.1 or 0.2 it may seem like a 100% variation, but in the first case the ball retains 1% of its original energy and in the second case it retains 4% of its original energy. Very small changes in the physical conditions may lead to such changes in the energy retained in the ball. It is for this reason that small values of restitution are particularly sensitive to details of the model, system parameters, and solution method.

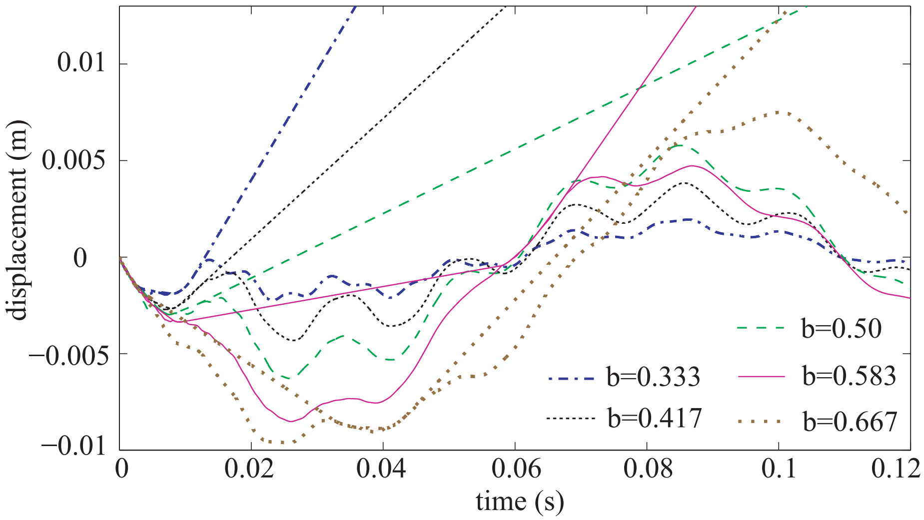

Figure 4.10: Ball and beam displacements against time for different b for the uniform fixed-free beam with $m = 0.608$. The straight lines are the ball's motion, the undulating lines are the beam-contact-point's displacement.

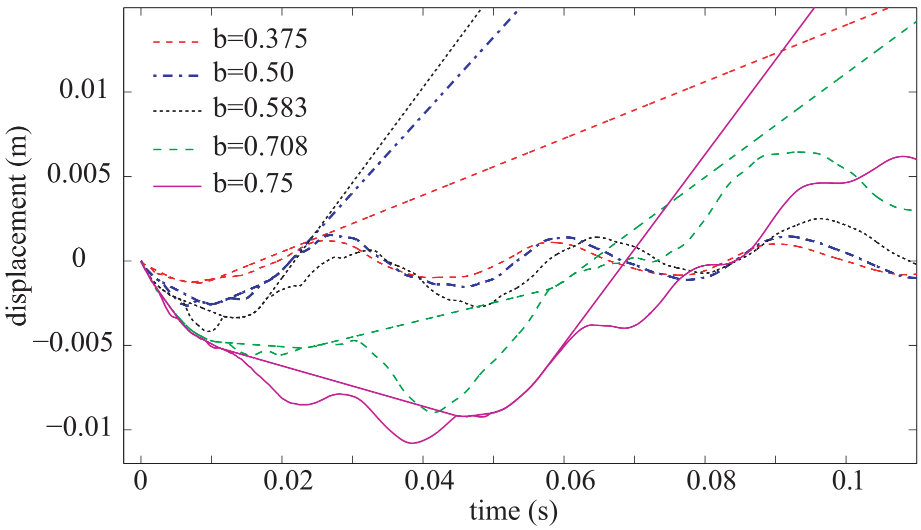

Figure 4.11: Ball and beam displacements against time for different b for the stepped fixed-free beam with $m = 0.147$. The straight lines are the ball's motion, the undulating lines are the beam-contact-point's displacement.

4.3 Concluding remarks

In this chapter, we have numerically studied vibration dominated impacts between a Hertzian ball and an Euler-Bernoulli beam. Through direct and detailed dynamic simulation, we have studied how the interaction varies with boundary conditions, impact location, and ball mass. These ball-beam restitution observations are used in the following chapters to guide a simple net-impulse model for vibroimpact problem.

Chapter 5

Algebraic models, contact inequalities and “outward” inequality

In chapters 3 and 4, we examined in some detail the impact between a Hertzian sphere and an Euler-Bernoulli beam. We will now try to capture same impact outcomes (obtained by solving ODEs) with more approximate net-restitution models in the spirit of algebraic or impulse-based collision models (without solving ODEs). There are various impulse-based models for single- and multiple-point impulsive contacts without accounting for vibrations. However, we have not seen explicit net-impulse based algebraic restitution modeling that accounts for impact induced vibration and multiple subimpacts in the way developed in this thesis.

Here, we begin with a general discussion of algebraic modeling of impacts, and then introduce the quadratic program based approach for impacts. Chapter 6 presents the model for vibration dominated impacts. Chapter 7 presents a possible model parameterization and fitting results.

5.1 Introduction

Incremental or continuous impact models consider a finite duration force and use differential equations to describe the evolving dynamics of the system during contact. They require detailed information like material model, geometry, contact characteristics etc. which may not be available or involve high computational cost. On the other hand, algebraic models consider the impulse as instantaneous and use some simple rules with a few fitted parameters, are approximate, yet have utility in fast dynamics simulations, like physically based animations, robotics, games, movies, and granular flows. Contact models based on the Linear Complimentary Problem (LCP) or based on quadratic programming are algebraic models as well, but have mostly been used in rigid body impacts [8, 16, 79, 80, 18].

Here, similar to some "rigid body" approaches (see e.g., [1, 3, 4, 5]), we assume that the overall contact interaction is brief though it may include multiple vibration-induced separations; motions during the impact interaction are small; contact and constraint forces are large compared with existing bounded forces like weight; velocity-squared acceleration terms can be neglected during the impact interaction; deformations during post-impact large motions are negligible; and the net effect of the contact impulses on those large "rigid body" or overall post-impact motions of the colliding objects is described accurately using rigid body impulse-momentum relations.

In such impacts, in spite of the above simplifying assumptions, the contact impulses remain indeterminate, and must be modeled using separate constitutive modeling or impact laws. In physical reality, the very short time impulsive opposing contact force depends on the localized deformation. However, in net-impulse modeling we predict the net change in overall motion quantities using rigid body dynamics and as such additional modeling assumptions are required. For example, for a two dimensional frictionless collision between two rigid bodies, we might specify a scalar coefficient of restitution.

The early articles [6, 37] and several other similar ones discuss a generalized momentum balance method for intermittent motion in flexible multibody systems. Therein, the authors show that, on incorporating sufficiently many assumed beam modes and a coefficient of restitution, and using a matrix formulation, it is possible to describe a single impulsive interaction in flexible body impacts. Note that, since the single contact may lead to subsequent subimpacts, the impact simulation may not end with one computed impulse.

Various studies have presented experimental validation with the aforementioned approach [23], considered plastic deformation and an equivalent restitution [13, 26], and the recent article [81] presents further developments along the same line of thought.

In an altogether different approach, experiments with a tilted rod falling on a massive object [19] were described using a detailed mechanically motivated modeling effort in [14]. Energy losses due to friction, local deformation, and transfer to vibration modes are separately modeled and accounted for in [14].

In a recent article [82], a two dimensional impulse based approach is presented for repeated impacts of a ball on a beam under gravity wherein change in impact location due to beam bending is accounted for. In contrast, we consider a single macroscopic impact with no gravity.

Our modeling approach, that significantly extends [18], includes a combination of basic contact constraints, kinetic energy minimization, and the introduction of key new inequality constraints which we refer to as *outward constraints*. We now discuss these background ideas that underline our approach.

5.2 General observations

We start with net impulse modeling of rigid body impacts. If two notionally rigid bodies collide at a point, then the impulse vector from one body to another, say $\mathbf{P}$, is related to the change in the relative velocity at the contact point, namely $\mathbf{v}_\mathrm{C}$, by

$$\mathbf{P} = \mathbf{M}_\mathrm{C} \Delta \mathbf{v}_\mathrm{C}, \tag{5.1}$$

where $\mathbf{M}_\mathrm{C}$ is a rank 2 tensor, has units of mass, and can be thought of as a local anisotropic contact inertia [79, 4]. In three dimensions, Eq. 5.1 presents three equations in six unknowns. Further modeling assumptions are thus needed. If the frictional impulse (consisting of two components) is zero, then only one unknown remains; historically, for such frictionless impacts, we define a (kinematic) coefficient of restitution $0 \le e \le 1$, introduced by Newton. Other definitions for restitution include the Poisson restitution (impulse-based) and energetic restitution [3] (normal-direction-work-based). The coefficient of restitution has been used for impacts with friction as well, e.g. [3, 10]. The Poisson and energetic restitution assume an absence of strong vibration effects; the Newtonian definition makes no such assumption. Readers looking for more exhaustive discussion of rigid-body impacts can see [1, 3, 2, 4, 5].

5.2.1 Restitution modeling using inequalities

Figure 5.1 depicts a well known problem with usual Newtonian restitution in simultaneous multiple impact.

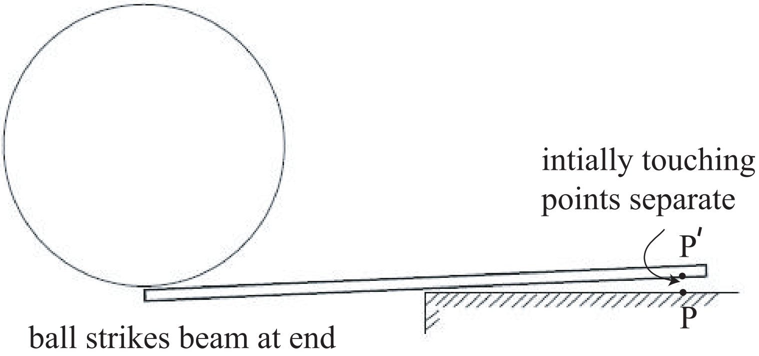

Figure 5.1: Usual kinematic (Newtonian) restitution is problematic here.

For single point impacts, the normal component of separation velocity is taken to be some modeled restitution coefficient e times the normal component of approach velocity,

$$v_{f,n} = -e v_{i,n},$$

where the subscript n denotes "normal" and the subscripts f and i denote final and initial respectively. The minus sign is because the approach and separation velocities have different senses. In Fig. 5.1, the dropping ball on the left end of the rod causes new separation to occur at a pre-existing stationary contact between the table and the right end of the rod. In this case, since $v_{i,n} = 0$, no finite e can model the impact. It is commonly understood, e.g.

[4, 2], that a good way to model restitution in simultaneous impact is to use an inequality constraint of the form

$$v_{f,n} \geq -ev_{i,n}, \quad \text{or} \quad v_{f,n} + ev_{i,n} \geq 0. \tag{5.2}$$

The next modeling step is to make the restitution amount definite. A commonly adopted approach is to use the linear complementarity conditions (LCP) on separation velocity and normal impulse P_n as follows:

$$v_{f,n} + ev_{i,n} \geq 0, \quad P_n \geq 0, \quad \text{and} \quad (v_{f,n} + ev_{i,n})\ P_n = 0.$$

However, we will make the impulse definite using a different approach which has some advantages over the LCP, see [79, 18].

5.2.2 Further restrictions

We observe that the contact interaction can never violate some fundamental physical relations, which can be described using several inequalities that either are linear or can be approximated as linear:

1. At any contact location, the normal component of the contact impulse is nonnegative (assuming no adhesion). This is a linear inequality constraint.
2. The normal component of the post-impact relative velocity at the contact point is nonnegative (since, otherwise, the bodies interpenetrate). This is a linear inequality constraint.
3. If we consider Coulomb friction at the contact, then in planar interactions, the friction inequality is effectively two linear inequalities. In three dimension, the friction inequality cone can be approximated using a set of m linear ones, where larger m makes the approximation better [16, 70]. These are linear inequality constraints.

4. Post-impact rigid body velocities are linear (technically, affine) functions of the contact impulses, given pre-impact velocities. These impulse-momentum relations are linear *equality* constraints.

Finally, kinetic energy, a quadratic function of velocities, is a quadratic function of the set of contact impulses. The predicted post-impact kinetic energy should not exceed the pre-impact kinetic energy. However, instead of treating this as a quadratic inequality, we will use minimization subject to additional constraints, as described next.

5.3 Towards a quadratic programming formulation: New outward inequalities

A significant conceptual departure from the net-impulse impact models referred to earlier was made by Todorov [80], who used a quadratic program to model impacts, wherein post-impact kinetic energy was minimized subject to friction and non-interpenetration constraints. This approach, while very interesting, often predicts impact outcomes with unrealistically low restitution or rebound. We do highly appreciate Todorov's idea, wherein post-impact kinetic energy is minimized subject to the linear inequality and equality constraints listed above. The only drawback of that approach is that collision outcomes have low rebounds.

This is where a key contribution of [18], and of this thesis, lies. In a fundamental extension of Todorov's idea, an additional "outward" or rebound-enhancing inequality was introduced for simultaneous multiple impacts of rigid bodies in [18], where it was found that predicted restitution outcomes were superior in several cases to outcomes predicted by the popular linear complementarity formulation (LCP).

To explain the idea of an outward inequality, consider a vertically dropped ball. Friction plays no role, and impulse-momentum relations are trivial. If we adopt Eq. 5.2, with $v_{i,n} < 0$ to ensure an impact and $0 \leq e \leq 1$, then nonnegative normal impulse and separation inequalities are automatically obeyed. If we now minimize the post-impact kinetic energy for the dropped ball, we obtain $v_{f,n} = -ev_{i,n}$, which is a satisfactory outcome. Here, Eq. 5.2 serves as a rebound-enhancing inequality. If it was not enforced, then minimization of kinetic energy would lead to a prediction of $v_{f,n} = 0$, which is the minimum possible level of rebound.

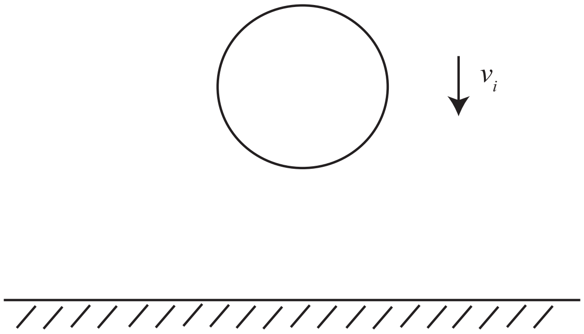

Figure 5.2: Ball falls on a rigid surface. Equation 5.2 ensures a minimum nonzero rebound.

The same idea, of an outward or rebound-enhancing inequality along with energy minimization, is formulated for vibroimpact in this thesis.

It is emphasized that the choices of two such inequalities used here are the main novel elements of the present work. No restitution inequalities like them have been similarly used in the vibroimact literature. The proposed quadratic program approach is guaranteed to never predict impossibilities (interpenetration, energy increases).

Subsequently, solution of the impact model equations is fairly straightforward using readily available routines in Matlab. We adopt *quadratic programming*, which fits our needs well:

1. the linear inequality constraints are incorporated easily;
2. the quadratic nature of the KE, which we minimize, is convenient;
3. there is scope for adding general new inequality or “outward” constraints; and
4. we have found possible model parameterizations within this framework that match detailed simulations well (see chapter 7).

Our quadratic program approach, which will be described in the next chapter, never violates the fundamental physical restrictions outlined above, gives a reasonable restitution value that is between 0 and 1, considers separately local energy losses and energy transmitted to beam vibration modes, and considers possible subimpacts. This approach, which we call Energy Minimization under Outward Constraints (EMOC), is novel. No similar and comparable modeling attempt exists in the literature.

Chapter 6

Energy Minimization with Outward Constraints (EMOC)

In this chapter, we develop a new modeling approach to restitution modeling for vibration-dominated impacts between a compact body and a flexible body. We refer to this model as Energy Minimization with Outward Constraints (or EMOC). The modeling approach minimizes post-impact kinetic energy subject to various basic impact restrictions and one or more additional "outward" or rebound enhancing inequality constraints. Such system-specific, non-unique, and to-be-found "outward" inequalities constitute the primary novelty of the approach.

Recall that a quadratic program with linear inequality constraints seeks to minimize, with respect to a column matrix of unknowns q, an objective function of the form

$$\frac{q^T Q q}{2} + c^T q,$$

subject to inequality constraints of the form

$$Aq \leq b,$$

where Q is a symmetric positive semidefinite matrix and c is a column matrix of appropriate size; and where A is a rectangular matrix with each row representing one constraint, and b is a column matrix of consistent size. In the special case where Q is positive definite and the feasible set is nonempty, there is a unique solution (see, e.g., [83], section 4.2.2).

We first present our EMOC model. The constraints therein are nonlinear. So we construct an equivalent quadratic formulation with linear constraints. Parameterization of the model is presented later in chapters 7 and 8 for two rather different problems.

6.1 Fundamental constraint on modal response amplitudes

The model incorporates a basic inequality as follows. The *instantaneous*-impulse response of a single mode a_i satisfies

$$\ddot{a}_i + \omega_i^2 a_i = \delta(t)\phi_i(b), \quad a_i(0) = 0,\ \dot{a}_i(0^-) = 0, \tag{6.1}$$

where $\delta(t)$ is the Dirac delta function and $\phi_i(b) \geq 0$. By elementary methods,

$$\dot{a}_i(t) = \cos(\omega_i t)\, \phi_i(b).$$

With an arbitrary time-varying downward force $-f(t)$, where $f(t) \geq 0$, the modal velocity satisfies

$$\dot{a}_i(t) = -\phi_i(b) \int_0^t \cos(\omega_i (t - \tau))\ f(\tau)\, d\tau \tag{6.2}$$

whence, in terms of the net impulse

$$P = \int_0^t f(\tau) d\tau > 0,$$

it follows easily that

$$|\dot{a}_i(t)| \leq \phi_i(b) P. \tag{6.3}$$

The above ensures that if impact occurs near a nodal location of a certain mode, then that mode cannot absorb much energy during the impact. Equation 6.3 represents N inequalities, which must be retained as constraint equations.

6.2 EMOC impact model

For our impact model, the known or specified quantities are:

1. the pre-impact velocity $v_{\mathrm{i}} < 0$,
2. a nominal restitution value e (we will use $e = 1$ unless otherwise stated),
3. the number of active modes, namely N[1], and
4. N mass-normalized mode shape values $\phi_i(b) \geq 0$.

It is understood that the beam velocities in modal coordinates, i.e., the $\dot{a}_i$, are all zero at the start of the interaction.

Our unknowns are the impacting body's post-impact velocity v_{f}, and the modal velocities $\dot{a}_i$. Of these, the modal velocities will presumably damp out quickly after the impact and are not of primary interest. The main quantity of interest is v_{f}. The post-impact kinetic energy of the system is simply

$$KE_{\mathrm{final}} = \frac{1}{2}\left(m v_{\mathrm{f}}^2 + \sum_{i=1}^{N} \dot{a}_i^2\right). \tag{6.4}$$

The model is now stated as follows:

1. Impulse-momentum for the impacting mass is $P = m(v_{\mathrm{f}} - v_{\mathrm{i}})$. The above implies, by Eq. 6.3,

$$|\dot{a}_i| \leq \phi_i(b) m (v_{\mathrm{f}} - v_{\mathrm{i}}),\ i = 1 \ldots N. \tag{6.5}$$

---

[1] In general it may be difficult to know a priori the number of active modes.

2. Our basic restitution inequality is

$$v_{\mathrm{f}} - \sum_{i=1}^{N} \dot{a}_i \phi_i(b) \geq -\bar{e} v_{\mathrm{i}}. \tag{6.6}$$

   In the above, although $\phi_i(b) \geq 0$, $\dot{a}_i$ is allowed to be negative. Also, $\bar{e}$ may be less than the specified e, based on model parameterization choices.

3. Higher mode oscillations, their participation in sub-impacts, and slow lower-mode dynamics are all included approximately in the following additional outward inequality, which is a key part of the proposed model:

$$v_{\mathrm{f}} - \beta_0 \sum_{i=1}^{N} |\dot{a}_{\mathrm{i}}| \phi_i(b) \geq -\beta_1 \bar{e}\, v_{\mathrm{i}}. \tag{6.7}$$

   Here, $\phi_i(b) \geq 0$, $\beta_0 \geq 0$, $0 \leq \beta_1 \leq 1$, $0 \leq \bar{e} \leq 1$. We draw the reader's attention to the absolute value used in $|\dot{a}_i|$, which is prompted by the fact that an away-going oscillatory velocity component can reverse itself to cause a fresh subimpact.

   Equation 6.7 is our key "outward" or rebound-enhancing inequality, and an essential part of our model. Since $v_i < 0$, the right hand side is positive; and since $\phi_i(b) \geq 0$, the second term on the left represents subtraction of a positive quantity; and therefore v_f is guaranteed to be positive if $\bar{e} \geq 0$, which is crucial for separation.

4. All our inequalities, including the "outward" inequality, are now in place: Eqs. 6.5, 6.6 and 6.7. The model minimizes post-impact kinetic energy, Eq. 6.4, subject to these inequalities. As discussed above, $v_f \geq 0$ is assured. It remains to demonstrate that kinetic energy increases are not predicted. To this end, we note that $\dot{a}_i = 0$ for all i, and $v_f = -\bar{e} v_{\mathrm{i}}$, satisfy all constraints *and* predict a reduction in net kinetic energy. This shows that there is a feasible point with nonnegative energy dissipation. The minimized kinetic energy is guaranteed to be at least as small. and possibly smaller. Thus, KE increases will never be predicted. It may be noted that Eqs. 6.6 and 6.7 are not unique and are modeling choices only. In general, the main feature that all

appropriate inequalities must share is that at least one point must be retained in the feasible set where is there is non-negative energy dissipation.

6.3 Equivalent model: Quadratic program

To easily solve the optimization problem posed in the previous section, we can write an equivalent quadratic program which can be solved using a built-in function in Matlab.

We introduce new variables c_i, and the new set of unknowns now is v_f, $\dot{a}_i$, and c_i, $i = 1 \ldots N$. The new quadratic function to be minimized is

$$\frac{1}{2}\left(mv_\mathrm{f}^2 + \frac{1}{2}\sum_{i=1}^{N}\dot{a}_i^2 + \frac{1}{2}\sum_{i=1}^{N}c_i^2\right), \tag{6.8}$$

subject to

$$\begin{aligned}
v_\mathrm{f} - \sum_{i=1}^{N}\dot{a}_i\phi_i(b) &\geq -\bar{e}v_\mathrm{i}, && (6.9)\\
v_\mathrm{f} - \beta_0\sum_{i=1}^{N}c_i\phi_i(b) &\geq -\beta_1\bar{e}v_\mathrm{i}, && (6.10)\\
\dot{a}_i &\leq c_i, \quad i = 1, 2, \cdots, N, && (6.11)\\
-\dot{a}_i &\leq c_i, \quad i = 1, 2, \cdots, N, && (6.12)\\
c_i &\leq \phi_i(b)m\left(v_\mathrm{f} - v_\mathrm{i}\right), \quad i = 1, 2, \cdots, N. && (6.13)
\end{aligned}$$

6.4 Proof of equivalence and uniqueness

Let the original impact model (minimize Eq. 6.4 subject to Eqs. 6.5, 6.6 and 6.7), be named problem P_0, and the obtained minimum value of Eq. 6.4 be called k_0. Let the new problem, namely minimize Eq. 6.8 subject to Eqs. 6.9 through 6.13, be named problem P_1, and the obtained minimum value of Eq. 6.8 be called k_1. It is easy to prove that P_0 and P_1 are equivalent.

First suppose P_0 has been solved. If we take its solution (which contains v_f and $\dot{a}_i$), and additionally let $c_i = |\dot{a}_i|$, then we obtain a feasible point of P_1 with same value of the objective function. In other words, P_1's minimum is not higher than that of P_0. That is,

$$k_1 \leq k_0.$$

Next suppose it is P_1 that has been solved. Then the c_i of P_1 must necessarily be equal to its $|\dot{a}_i|$ for each i; for otherwise the c_i could be reduced to equal $|\dot{a}_i|$ without violating any constraints, and the objective function could be lowered further, giving a contradiction. But if the c_i are equal to $|\dot{a}_i|$, then the same $\dot{a}_i$ and v_f provide a feasible point of P_0 and yield the same value of the objective function. In other words, P_0's minimum is not higher than that of P_1. That is,

$$k_0 \leq k_1.$$

Combining the above two paragraphs, we find that the two problems P_0 and P_1 must give the same minimum value, i.e, $k_0 = k_1$. Naturally, P_1 is preferred because it can be solved using standard software.

It remains to check if the minimizing values of the variables are unique. Since P_1 satisfies the conditions mentioned at the start of the chapter, its solution is unique (see [84], section 2.3.2). To prove that the solution of P_0 is unique, we can directly tackle the $|\dot{a}_i|$ in that problem statement. To this end, note that any inequality of the form

$$|A_1| + |A_2| + \cdots |A_N| \leq B \tag{6.14}$$

is equivalent to the set of 2^N linear inequalities

$$\pm A_1 \pm A_2 \cdots \pm A_N \leq B.$$

By the above simple trick, problem P_0 is actually equivalent to a quadratic program in the same variables, albeit with a large number of linear inequality constraints; it therefore has a unique solution as well. Problem P_1 is preferred because it is both equivalent and has fewer constraints.

6.5 Concluding remarks

Our EMOC approach minimizes the post-impact net kinetic energy subject to several inequalities. These linear inequalities express various constraints on the mechanics and the motion, and include an outward or rebound enhancing linear inequality constraint. The outward inequality cannot really be derived from mechanics or physics, and must be proposed based on intuition and approximation.

We now validate the model for two cases: (a) the ball-beam impacts outcomes presented in chapter 4, and (b) a tilted beam dropped on an immovable surface. We take up these two problems in chapters 7 and 8.

Chapter 7

Ball-beam impact: formulation and fitting results

We first make a few modeling simplifications using which we describe the model parameters $\bar{e}$, β_0 and β_1. Later we fit the EMOC model to the obtained numerical restitution values in chapter 4.

7.1 Dimensionless numbers, and functions thereof

We first look at the available variables and identify a few relevant nondimensional quantities. Simple functions of these dimensionless quantities are then chosen to characterize some aspects of the considered vibroimpact problem.

The available or specified variables are:

1. colliding mass,
2. impact velocity,
3. notional restitution e (without vibratory effects and no dissipation),
4. Hertzian contact stiffness,
5. beam natural frequencies,

6. beam mode shapes at contact location, mass-normalized (i.e., not $\phi(x)$ entirely, but only $\phi(b)$), and
7. the number of active vibration modes.

We list these same quantities using symbols below, assuming without loss of generality that $\phi_i(b) \geq 0$ because mass normalized mode shapes have indeterminate sign:

$$m,\ v_{\mathrm{i}} < 0,\ e,\ k_H,\ \omega_i,\ \phi_i(b) \geq 0,\ N. \tag{7.1}$$

We now make the following modeling assumptions and simplifications:

1. Natural frequencies:

   We drop ω_i from our list (Eq. 7.1) because we will not model the temporal structure of the impact. Our aim is an algebraic or net-impulse model.

2. Contact stiffness:

   k_H affects the duration of each separate contact or sub-impact. However, we will not model those in detail. Yet, if we treat k_H as infinite, then an infinite number of modes should get excited. In this way, we think of k_H as approximately determining the number of active modes N; and we drop k_H but retain N. Another way to say it is that the role of the contact stiffness is approximately retained through the presence of N in the model.

3. Dissipation:

   Our model is for a lightly damped beam, where vibrations are significant but very high modes damp out during the relatively extended impact interaction. Beyond choice of finite N, this is not incorporated explicitly.

4. Modes $\phi_i(b)$ and impacting mass m:

We assign a special role to two simple quantities:

$$\phi_1(b) \quad \text{and} \quad \sum_{i=1}^{N} \phi_i^2(b).$$

The first of the above two quantities is related to the low frequency response (which is usually dominated by the first few modes). The second quantity provides a simple measure of the richness or intensity of the modal response to an impulse at location b; it will also be directly relevant to kinetic energy considerations later on.

For later nondimensionalization, we note that mass-normalization of the modes means

$$\int_0^L \rho A \phi_i(x)^2 \, dx = 1, \qquad \text{where} \qquad \int_0^L \rho A \, dx = \text{ mass of the beam.}$$

It follows that $\phi_i^2(b)$ is of the order of the reciprocal of the beam mass. The quantity $m\phi_i(b)^2$, where m is the mass of the impacting sphere, is *dimensionless*.

More formally, consider the ratio of the velocity change of the beam-contact-point to the velocity change of the colliding sphere under equal and opposite impulses P. Integrating dissipationless beam-modal equation over the infinitesimal contact duration ϵ, we obtain the jump discontinuity for the modal velocity under instantaneous P as

$$\int_0^{\epsilon} \ddot{a}_i dt + \int_0^{\epsilon} \omega_i^2 a_i dt = -\int_0^{\epsilon} F\phi_i(b) dt \Rightarrow \dot{a}_i^+ = -P\phi_i(b). \tag{7.2}$$

The above induces a contact point velocity (as contributed by the i^{th} mode) of $-P\phi_i^2(b)$. For the colliding mass, the change in velocity is P/m. The ratio of the two has magnitude

$$Z = -\frac{\Delta v(b)_{\text{beam}}}{\Delta v_{\text{sphere}}} = m \sum_{i=1}^{N} \phi_i(b)^2, \tag{7.3}$$

which is dimensionless. Noting that Z of Eq. 7.3 is a mass ratio that is affected by mode shape magnitudes, we refer to it informally as a moderated mass ratio.

The system parameter Z will be useful in our modeling efforts. For small Z (small m;

or small $\sum \phi_i(b)^2$, which occurs near fixed points of the structure), we have observed that v_{f} is relatively high (closer to unity). For large Z (large m or high contact compliance), v_{f} is high again. For intermediate Z, v_{f} is low. We will use these observations later.

5. Multiple sub-impacts:

Qualitatively, we can think of the beam modes as lower modes and higher modes (admittedly, the boundary between them is blurred). The lower modes cause large deflections and slow subsequent returns of the beam into a fresh contact event; and the higher modes cause rapid oscillations, loosely reminiscent of a disordered buzzing, influencing the velocity of the beam contact point. We try to model the above in an average sense.

The separation between the two types of modes is enhanced and simplified by considering the *first* mode as representing slow modes and *all* modes together as an overall collection of fast modes.

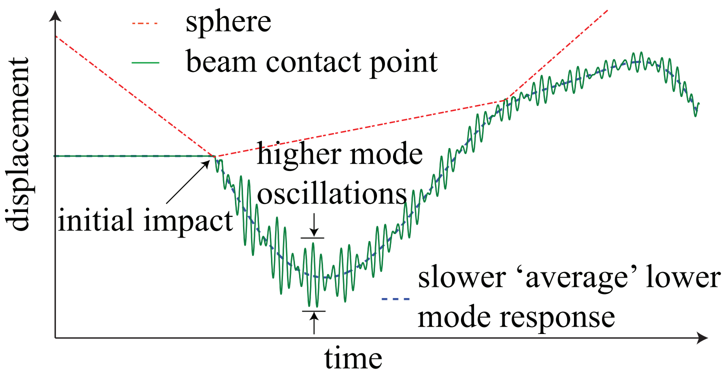

Figure 7.1: Schematic showing lower mode dynamics causing a return to fresh contact, and higher mode dynamics influencing rebound levels therefrom. Oscillatory displacement amplitudes are exaggerated for illustration.

The qualitative idea is shown schematically in Fig. 7.1, where oscillations in beam displacement are exaggerated. The beam's contact point velocity plot depicts significant high frequency oscillations (recall Fig. 4.5). With this view, we will use two terms: one involving all modes, to represent all higher modes; and one involving only the first mode, to approximate the lower-mode responses.

6. Vibration-incorporating restitution:

   Recall item 4 above. We need a function of Z that is close to unity for both small and large values of Z, and has a minimum for an intermediate value. To this end, we consider

   $$\frac{\mu_0^2 Z^2 + 1}{\mu_0^2 Z^2 + \mu_0 Z + 1}, \tag{7.4}$$

   where our first fitted parameter $\mu_0 > 0$ is thought of as a moderated mass ratio coefficient. The above function value is unity for $Z = 0$ and $Z \to \infty$; and it has a minimum of 2/3 at $Z = 1/\mu_0$.

   In the impact model below, for a given notional restitution value $0 \leq e \leq 1$, we will use a vibration-incorporating restitution

   $$\bar{e} = \frac{\mu_0^2 Z^2 + 1}{\mu_0^2 Z^2 + \mu_0 Z + 1}\, e. \tag{7.5}$$

   Clearly, other choices could have been adopted. Our choice is based on its simplicity and a wish to keep the number of fitted parameters low. Note that Eq. 7.5 incorporates information about the ratio of masses (ball and beam), as also the collective modal response at the beam contact point.

7. Average modal richness parameter:

   An average value over all active modes, which we have found useful for modeling multiple sub-impacts, is

   $$S_0 = \frac{Z}{N}, \qquad \text{whence we define,} \qquad \beta_0 = \frac{\alpha_0 S_0}{1 + \alpha_0 S_0} = \frac{\alpha_0 Z}{N + \alpha_0 Z}, \tag{7.6}$$

   where in turn $\alpha_0 > 0$ is our second fitted parameter, referred to as a modal richness coefficient. β_0 is given in terms of α_0 and the system parameters Z and N, and is guaranteed to lie between 0 and 1 in this restricted parameterization although in chapter 6 we noted that $\beta_0 \geq 0$ is sufficient for physical reasonableness.

8. Pseudostatic response:

   For incorporating low-frequency or pseudostatic responses, we will use only the first mode. Along the lines of item 7, we define

   $$S_1 = m\phi_1(b)^2, \quad \text{and} \quad \beta_1 = \frac{\alpha_1 S_1}{1 + \alpha_1 S_1}, \tag{7.7}$$

   where $\alpha_1 > 0$ is our third and final fitted parameter, referred to as a slow response coefficient. β_1, also, is guaranteed to lie between 0 and 1.

We observe that the dimensionless quantities defined above, namely $\bar{e}$, β_0 and β_1, are all between 0 and 1; and that the parameters μ_0, α_0 and α_1 are positive but otherwise unrestricted. The notional restitution e is assumed given, and in the present study is taken as $e = 1$ because there is no contact dissipation. Thus, our collision model has only three fitted parameters.

7.2 Model parameter fitting results

We now validate our EMOC model, which minimizes Eq. 6.8 subject to Eqs. 6.9 through 6.13, for the four beams given in Fig. 7.2 (same as in Fig. 4.2, repeated here for completeness).

For each beam, we had numerically found the rebounds v_{f} (with $v_{\mathrm{i}} = -1$) for varying sphere mass m (12 values) and impact location b (25 locations) with $N = 40$, see chapter 4. For each beam separately, for the full set of 12×25 data points, we use Matlab's "fminunc" optimization routine to fit v_{f}s in a least squares sense using three positive parameters μ_0, α_0 and α_1. It may be noted that for quadratic programming for EMOC model we use Matlab's "quadprog" sub-routine[1].

---

[1] Matlab's ("R2013a") "quadprog" sub-routine has different options. The default method is the "trust-

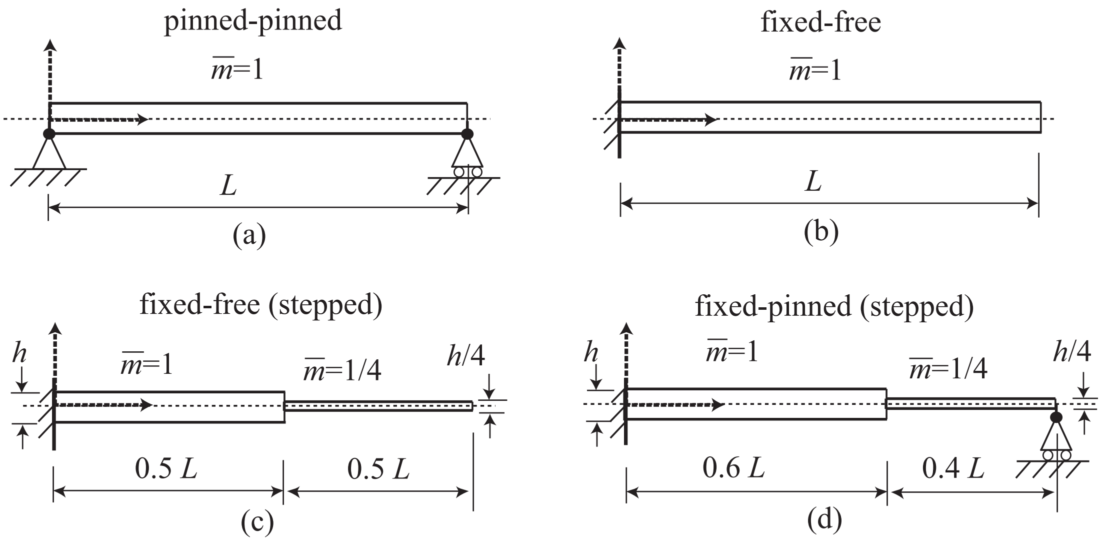

Figure 7.2: Four beams considered. Where $\overline{m} = 1$, the beam cross section is square. In slimmer portions with $\overline{m} < 1$, the width is kept the same and the thickness is lowered.

In particular, the overall calculation is done as follows. A Matlab program is written which will take an input parameters μ_0, α_0 and α_1. It then generates the other parameters. Then it predicts the model's impact outcomes, subtract the true restitution, square all of these predicted errors, add them up and return that scalar value. Finally, Matlab's "fmincon" subroutine was used to minimize that scalar value as a function of μ_0, α_0 and α_1.

For a single beam (12 m's, 25 b's), the full numerical simulation (using modal analysis) takes about 10 hours on an ordinary desktop computer. For a single beam, optimization for the EMOC model takes about ten minutes (100 to 200 function evaluations).

For the EMOC model the number of active modes N is a free parameter as discussed in item 2 in section 7.1. For fitting the quadratic program model we have used $N = 50$ because in principle we should not know the number of modes retained in the full dynamic solution. In fact, results do not change much between $N = 40$ and 50, see Fig. 7.7. The fitting results are shown in Figs. 7.3, 7.4, 7.5, and 7.6. It is emphasized that each of these

---

region-reflective", and other available options are the "interior-point-convex" and "active-set". For 50 modes and our somewhat complex calculations, the "interior-point-convex" was seen to be more reliable. That later option was used uniformly for all calculations in the thesis.

figures, with 25×12 data points, corresponds to *one* fitted set of μ_0, α_0 and α_1 as mentioned therein. In the figures, red plus signs mark results obtained using by solving ODEs, and blue circles mark results using the quadratic program based algebraic model.

For each beam, our model captures reasonably well the variation of v_{f} with m, and captures correctly the rising trend near the beam's free end in both relevant cases. The model also captures correctly the variations seen near the beam's steps in geometry, in both relevant cases; the variation is downward for very small masses, upward for intermediate masses, and shrinks for larger masses; these trends are all captured. At fixed or pinned ends, rebound is perfect, and captured by our model. The model is, however, unable to capture details of the somewhat irregular variation in rebound velocity with changing impact location; in these regimes, the average behavior is reasonably captured.

To comment on the mismatch, it may be noted that our model has some ad hoc components. In particular, the outward constraints that are adopted are based on guesswork and successful parameterization, so that the average behavior is captured. There is no a priori reason to be sure that the adopted outward inequalities are in fact physically accurate. Only the final fit demonstrates that they are useful. Similarly the inequalities on the modal velocity amplitudes as a function of net-impulse are loose inequalities, e.g.. if several subimpacts occur at different phases then the sum would have a significantly smaller magnitude than the inequality bound. In the presence of all these inaccuracies, which seem to be unavoidable in our algebraic approach, a detailed match with the entire range of behaviors has not been obtained. Please note however that our model presents significant progress; nothing comparable has been presented in earlier studies of this topic.

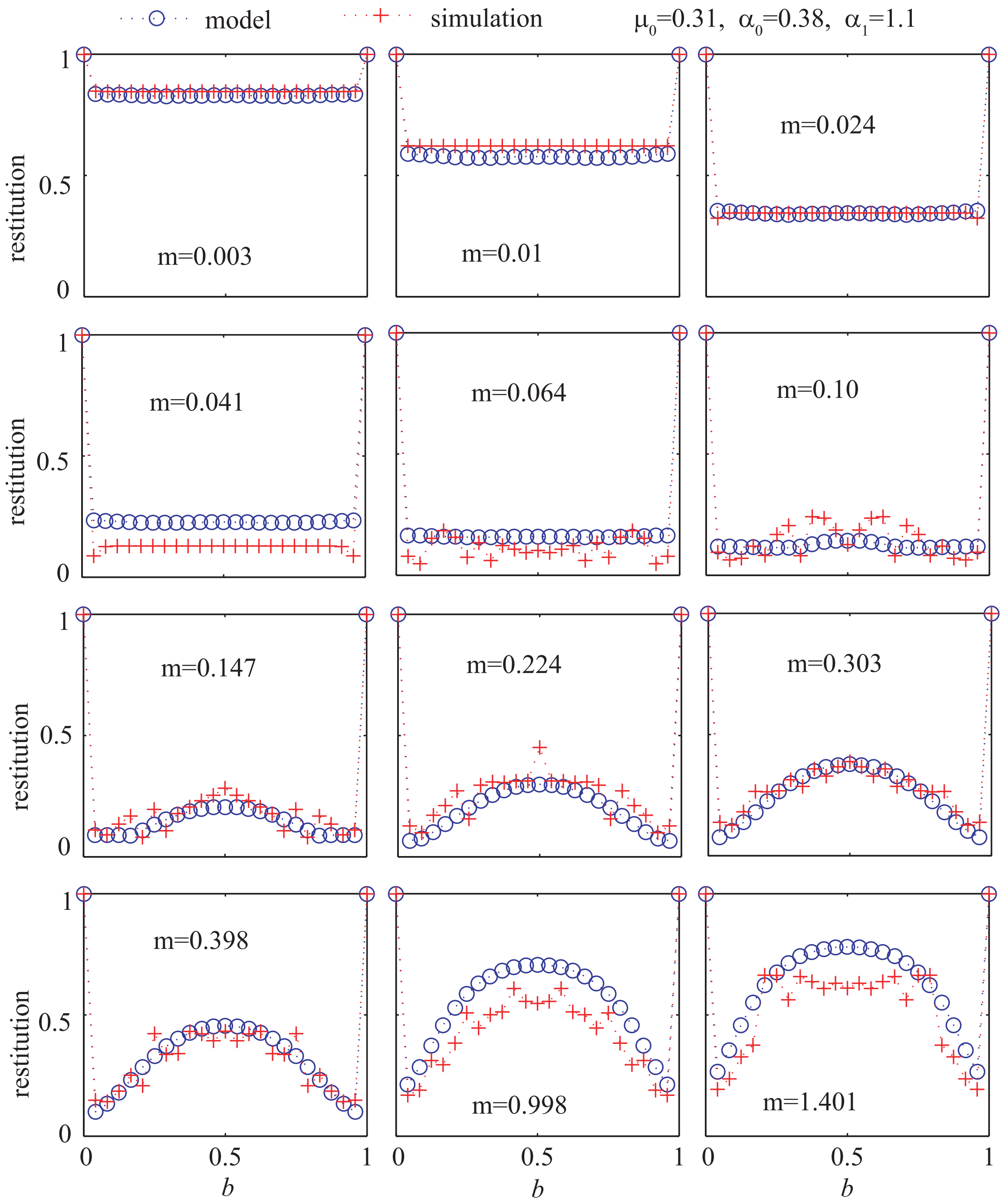

Figure 7.3: Pinned-pinned uniform beam.

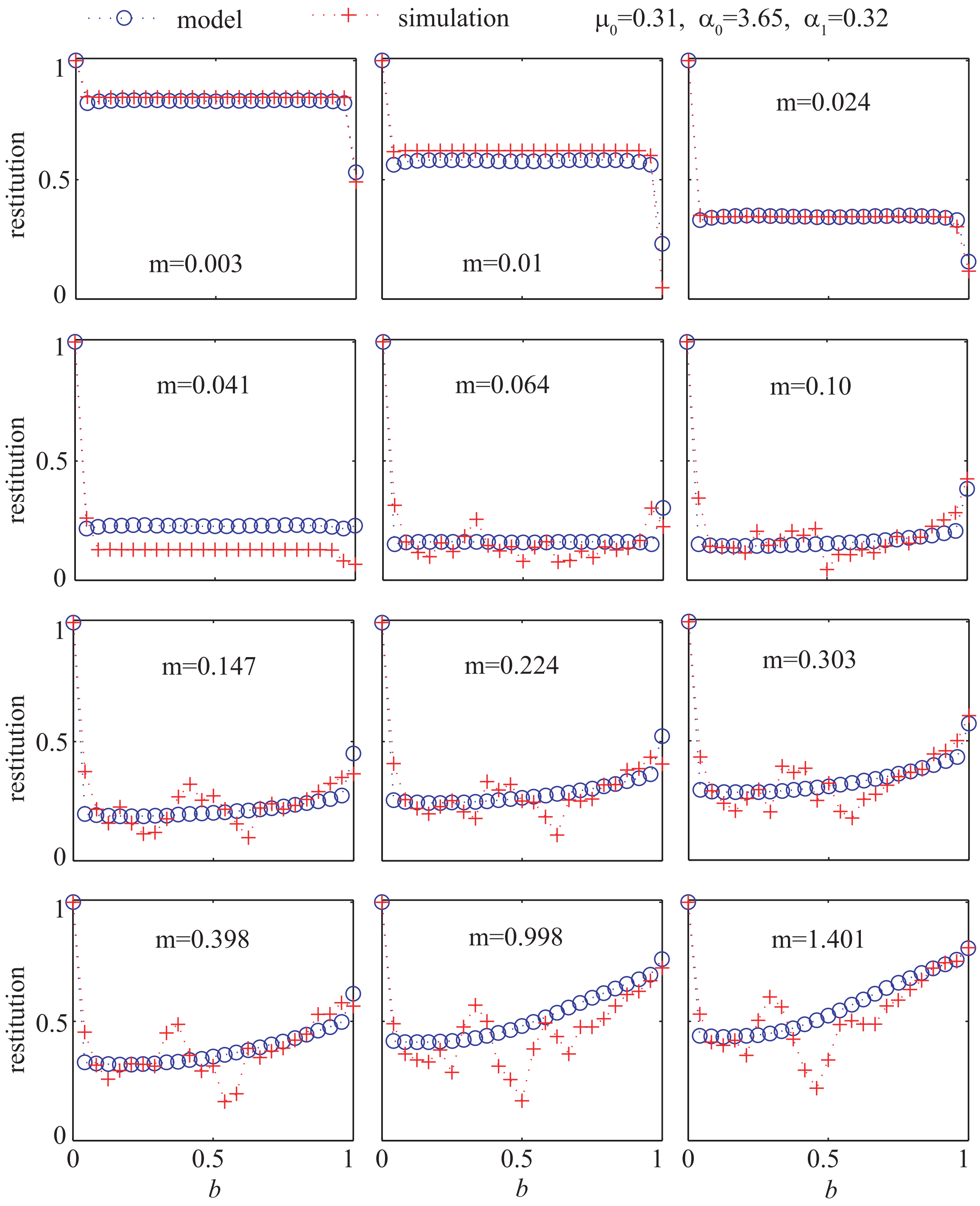

Figure 7.4: Fixed-free uniform beam.

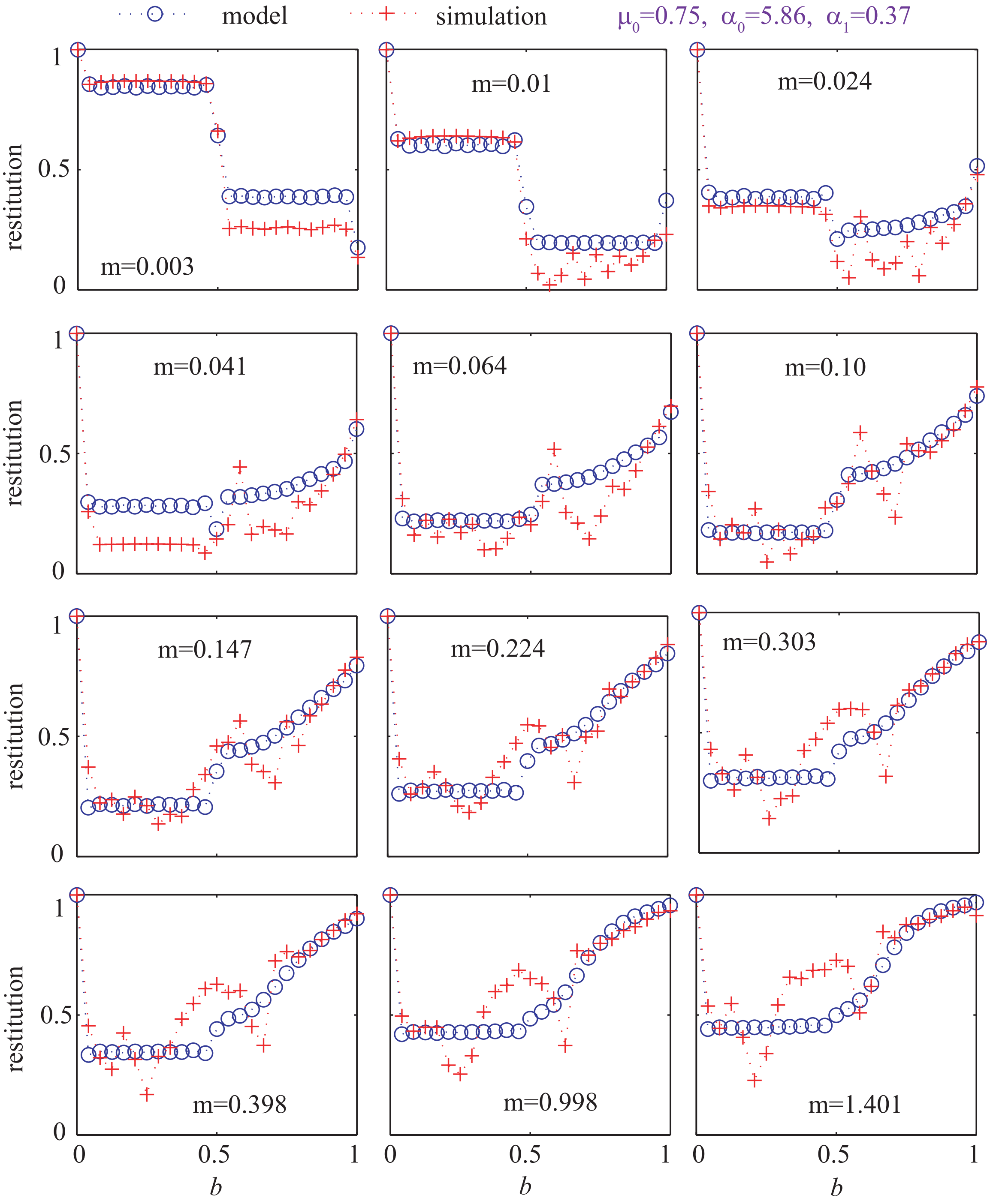

Figure 7.5: Fixed-free stepped beam.

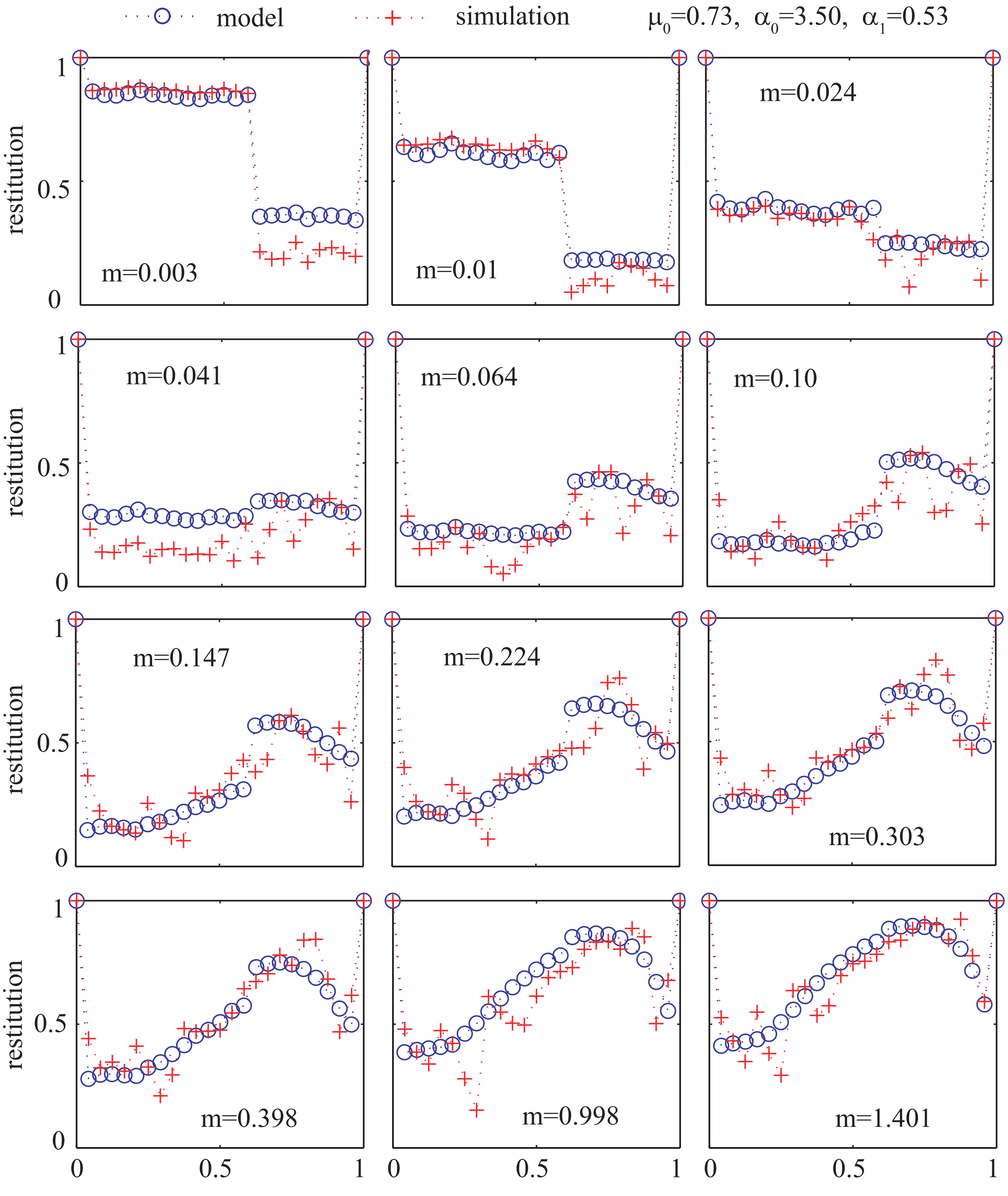

Figure 7.6: Fixed-pinned stepped beam.

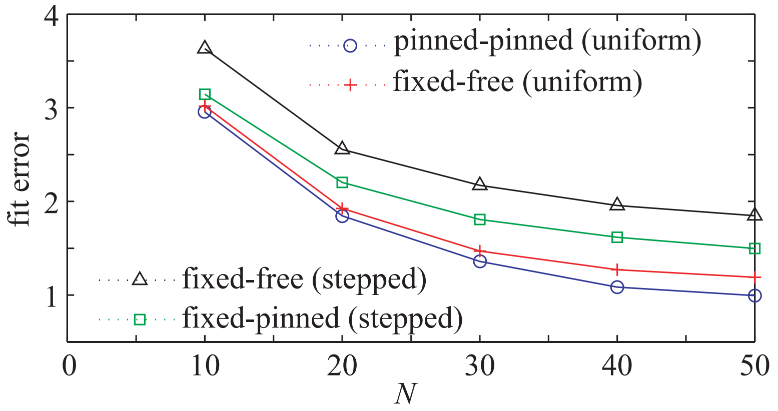

Figure 7.7: Fitting error of the algebraic model with different N for the four beam types studied. In the main text, we used $N = 50$. It is seen that the difference beyond $N = 40$ is small.

7.3 Concluding remarks

The proposed model has three fitted parameters for a given beam. Since even linear regression with two variables, of the form $q_0 + q_1 m + q_2 b$, would have three fitted coefficients, the number of fitted parameters should be viewed as small. In the same context, the overall performance of the model is good.

It is emphasized that, even with guessed μ_0, α_0 and α_1 (e.g., with all of them set to 1), the model will in any case predict physically feasible solutions, even if they may not match detailed dynamic simulation. The approach presented can also be used for other vibroimpact situations, e.g., impacts between compact bodies and thin plates or other flexible, lightly damped barriers. As such, the present algebraic model can be used with confidence for quick simulations in movies, virtual reality, computer graphics, and early stage design studies, e.g., granular flows or robotics.

Chapter 8

Dropped tilted rod: formulation and fitting results

We finally try to fit the EMOC model to a type of impact for which it was *not designed*. The reason for this attempt is a similarity in governing equations as will be seen below, although the physical interpretations are different.

Stoianovici and Hurmuzlu [19] experimentally obtained restitution values for slender bars dropped on a rigid surface at different angles of inclination. We now model their experimental outcomes using our EMOC approach.

In [19], the authors studied the 2D motions of freely dropped bars rebounding from a rigid immovable surface. The rods (hardened steel, $\rho = 7876.74$ Kg/m^3, $E = 2.1 \times 10^{11}$ Kg/m^2) had circular cross-sections with hemispherical ends. Several experiments were carried out, with different dropping heights, angles of inclination at impact, and bar lengths. The post-collision rigid body motion variables were measured using a high-speed camera. The number of collisions within each impact was measured as well, using electrical contact detection.

Subsequently, a simulation was developed that used several discrete rigid segments with interconnecting springs and dash-pots. A good match was reported. Here, we only use the experimental results, and match them approximately using our EMOC approach.

We first formulate the equations of motion. Later, we present the fitting results and discussion.

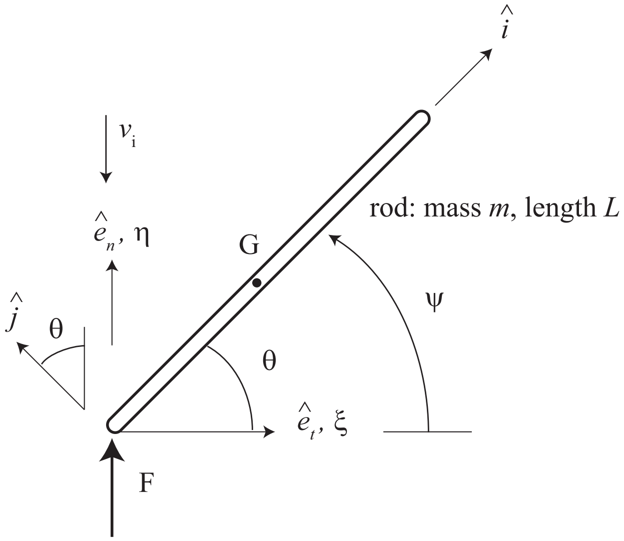

Figure 8.1: Free body diagram of a rod striking a surface at a configuration of θ. The rigid body mode rotational degree of freedom is ψ. θ is a parameter and ψ varies dynamically, but $\psi(t) \approx \theta$ at all times during the collision.

8.1 Equations of motion

See Fig. 8.1. A bar (mass m, length L) strikes an immovable surface at an orientation angle of θ measured from the horizontal. The unit vectors $\hat{e}_t$ and $\hat{e}_n$ are along the horizontal and vertical axes respectively, while $\hat{\imath}$ and $\hat{\jmath}$ are along, and normal to, the rod respectively. η and ξ denote the post-impact rigid body displacements of the rod center of gravity G, whereas ψ denotes the rod's rotation. The freely dropped rod has a downward velocity of $v_{\mathrm{i}} < 0$ at impact. F denotes the force at contact that is normal to the surface. Friction is neglected. The bar vibrates upon impact (both lateral and axial modes), while the stuck surface shows no macroscopic motion whatsoever.

The lateral and axial vibrational displacement of the bar is expressed in terms of the *normal* modes, as discussed in chapter 4, here written as

$$\sum_{k=1}^{N_l} q_{l_k}(t)\phi_{l_k}(x)\hat{j} + \sum_{j=1}^{N_a} q_{a_j}(t)\phi_{a_j}(x)\hat{i},$$

where lateral and axial vibrations are written separately, subscripts 'l' and 'a' denote lateral and axial vibration respectively, the q's denote generalized coordinates and the ϕ's denote the mode shapes. The coordinate x is along the $\hat{i}$ direction. N_l (or N_a) denotes the number of modes to be retained.

Considering free-free boundary conditions on the bar, we first obtain its normal modes and the corresponding natural frequencies. For a bar of length l, the mass-normalized modal displacement at the bar's end is $\phi_{l_k}(0) = \dfrac{2}{\sqrt{L}}$ and $\phi_{a_j}(0) = \dfrac{\sqrt{2}}{\sqrt{L}}$ for all k and j respectively.

We use the Lagrangian formulation to determine the equations of motion during collisional contact, i.e. for non-zero F but with neglected weight.

The kinetic energy of the system is

$$T = \frac{m}{2}\left(\dot{\xi}^2 + \dot{\eta}^2 + \frac{L^2}{12}\dot{\psi}^2\right) + \frac{1}{2}\sum_{k=1}^{N_l} \dot{q}_{l_k}^2 + \frac{1}{2}\sum_{j=1}^{N_a} \dot{q}_{a_k}^2. \tag{8.1}$$

The potential energy of the system is

$$V = \frac{1}{2}\sum_{k=1}^{N_l} \omega_{l_k}^2 q_{l_k}^2 + \frac{1}{2}\sum_{j=1}^{N_a} \omega_{a_k}^2 q_{a_k}^2. \tag{8.2}$$

We neglect friction. The various generalized forces are

$$Q_\xi = 0, \quad Q_\eta = F, \quad Q_\psi = \frac{FL}{2}\cos(\theta), \quad Q_{q_{l_k}} = F\phi_{t_k}(0)\cos(\theta) \quad Q_{q_{a_j}} = F\phi_{a_j}(0)\sin(\theta). \tag{8.3}$$

The equations of motion are

$$m\ddot{\xi} = 0, \qquad m\ddot{\eta} = F, \qquad \frac{mL^2}{12}\ddot{\psi} = \frac{FL}{2}\cos(\theta), \tag{8.4}$$

and

$$\ddot{q}_{l_k} + \omega_{l_k}^2 q_{l_k}^2 = F\phi_{l_k}(0)\cos(\theta),\ k = 1\dots N_l, \tag{8.5}$$

and

$$\ddot{q}_{a_j} + \omega_{a_j}^2 q_{a_j}^2 = F\phi_{a_j}(0)\sin(\theta),\ j = 1\dots N_a. \tag{8.6}$$

It is now important to note that ξ, η and ψ contribute indistinguishably to the rigid body part of the normal component of the contact point's displacement, which is

$$Z_{RB} = \eta + \frac{L}{2}\psi\cos(\theta). \tag{8.7}$$

Differentiating twice, we obtain

$$\ddot{Z}_{RB} = \ddot{\eta} + \frac{L}{2}\ddot{\psi}\cos(\theta) = \frac{F}{m} + \frac{L\cos(\theta)}{2}\frac{6F\cos(\theta)}{mL} = \frac{F}{m}\left(1 + 3\cos^2(\theta)\right). \tag{8.8}$$

Seeking an equation of the form

$$m_{\mathrm{RB}}\ddot{Z}_{\mathrm{RB}} = F,$$

to match Eq. 4.2, we find that we must use

$$m_{\mathrm{RB}} = \frac{m}{1 + 3\cos^2(\theta)}. \tag{8.9}$$

Recall that, our EMOC model minimizes the post-impact kinetic energy of the system subject to several linear constraints. We are interested only in restitution in the normal direction. As such, we need to represent all dynamic variables in the constraint equations in the $\hat{e}_n$ direction. As in chapter 7, here too we use vibration modes, modal displacements, and an effective mass m_{RB} as above. However, there are differences from chapter 7. There a compact mass strikes a stationary beam that vibrates. Here the dropped beam vibrates and has rigid body motions as well. Also, here the impact location is the same for all cases, but the beam angle varies.

Consider $a_k(t)\phi_{k_{\mathrm{eff}}}(x)$ as the *vertical component of* displacement of the contact point due to vibrations (both axial and transverse). For the transverse modes, this means $a_k \phi_{k_{\text{eff}}} = q_{l_k} \phi_{l_k} \cos(\theta)$. We denote $a_k = q_k$, $\phi_{k_{\text{eff}}} = \phi_{l_k} \cos(\theta)$, the vibrational kinetic energy remains $\sum \frac{1}{2} \dot{q}_k^2$, and we only need to replace the earlier $\phi(b)$ (in Eqs. 6.5, 6.6 and 6.7) with the

$$\phi_{k_{\text{eff}}} = \frac{2}{\sqrt{L}} \cos(\theta), \quad \text{if lateral mode.}$$

By nearly identical arguments, we find

$$\phi_{k_{\text{eff}}} = \frac{\sqrt{2}}{\sqrt{L}} \sin(\theta), \quad \text{if axial mode.}$$

Therefore, we have essentially the same mathematical structure as for the ball-beam impact of chapter 7. The physical details are quite different, however. It is interesting to see how well EMOC works for these tilted rod impacts.

The notable points in adapting EMOC to this system are

- Instead of m, we will use the effective mass m_{RB} in Eq. 8.9 that relates the vertical acceleration at contact point to the contact force F,
- We will use modal displacements in the vertical direction as the new effective displacement (see above),

The model parameters to be fitted are μ_0, β_0 and β_1.

Using the effective mass in Eq. 8.4, the total kinetic energy to be minimized is

$$KE = \frac{1}{2} m_{\text{RB}} v_{\text{f}}^2 + \frac{1}{2} \sum_N \dot{a}_k^2 = \frac{1}{2} \left(\frac{m}{1 + 3\cos^2(\theta)} \right) v_{\text{f}}^2 + \frac{1}{2} \sum_N \dot{a}_k^2, \tag{8.10}$$

where $v_{\text{f}} = \dot{Z}_{\text{RB}}$ is post-impact velocity of the rod's end point in the vertical direction. The above includes both transverse and axial modes.

The constraints are

$$|\dot{a}_k| \le \phi_{k_{\mathrm{eff}}} m_{\mathrm{RB}}(v_{\mathrm{f}} - v_{\mathrm{i}}),\ \ k = 1 \ldots N, \tag{8.11}$$

$$v_{\mathrm{f}} - \sum_{N} \dot{a}_k \phi_{k_{\mathrm{eff}}} \ge -\bar{e}\, v_{\mathrm{i}}, \tag{8.12}$$

$$v_{\mathrm{f}} - \beta_0 \sum_{N} |\dot{a}_k| \phi_{k_{\mathrm{eff}}} \ge -\beta_1\, \bar{e}\, v_{\mathrm{i}}. \tag{8.13}$$

We reemphasize, $\dot{a}_k = \dot{q}_k$ are the modal velocities, $\phi_{k_{\mathrm{eff}}}$ is the modal displacement in the $\hat{e}_n$ direction. All the constraints above include variables resolved in the vertical direction. As done earlier, we use the previously given equivalent quadratic program (see section 6.3) which we solve using Matlab.

8.2 Fitting results and discussion

We will now fit the EMOC model to the data of Stoianovici and Hurmuzlu [19] (see also Appendix A.5). We note that they have presented data for five (5) different rod lengths. For each rod length, they have presented data for many different rod inclinations.

Using a web-based tool, we extract restitution values approximately at 60 different angles of inclination for each rod length. Using our three parameter model, we will try to choose one set of three parameters that will match all the data reasonably well.

8.2.1 Problem caused by axial modes

When fitting the data, we realize that there is a difficulty when we include the axial modes of the rod. This is because all the natural frequencies of axial vibrations of the rods are commensurate[1]. In fact, a perfectly vertically dropped rod on a rigid surface according to 1D rod theory has perfect normal restitution $e = 1$, and leaves the impacted surface with no vibrational effects, see [1, 46]. Specifically, if two rod rods having identical mass per

---

[1] for free-free beam, the axial natural frequencies are $\omega_n = \frac{n\pi}{L}\sqrt{\frac{E}{\rho}}$ with $n = 1, 2, \ldots$.

unit length and density but having lengths L_1 and L_2 collide normally (along their axes), the restitution is $e = \frac{L_1}{L_2}$. In the special case when $L_1 = L_2$, it is like one rod colliding with a rigid surface, and the restitution is $e = 1$. This remarkable behavior affects the collision outcome even when the rod is nearly vertical, and we have found that the EMOC approach fails to accurately capture the data when axial modes are retained, because the EMOC model predicts that energy goes into the axial modes, lowering overall restitution.

Interestingly, in the present problem, when the rod is nearly horizontal the axial modes are not excited and the bending (lateral) modes dominate. When the rod is nearly vertical, bending modes are not excited strongly. It can be be seen in [19] (see also appendix A.5) that for nearly vertical impacts, there occurs a single contact event.

The net consequence is that if we retain axial modes then the EMOC model underpredicts the restitution for this problem.

8.2.2 Better results with only lateral modes

By coincidence an interesting improvement in the fit occurs when the axial modes are left out of the model. The reason is that the lateral modes do *not* get excited when the rod is nearly vertical. Qualitatively, this is like the problem of chapter 7 where impact occurs near a support point and restitution increases because vibrations do not get excited. In the same way, if we do not retain the axial modes and include only the lateral modes, then the impact restitution increases for the nearly vertical rod case, which matches experiments. In reality, the axial modes may participate briefly and the restitution is still high, but the EMOC model does not capture that dynamics.

Since we do not want to include axial modes, it appears inconsistent to include lateral vibration modes whose frequencies exceed that of the first axial mode. For this reason, for every rod, we calculate the first several lateral mode frequencies and retain only those modes whose frequencies are smaller than the first axial mode frequency.

The number of lateral modes retained for the rods of different lengths are: (a) 7 modes (600 mm), (b) 5 modes (400 mm), (c) 4 modes (300 mm), (d) 3 modes (200 mm) and (e)

2 modes (100 mm).

We emphasize that we will use the same parameter values μ_0, α_0 and α_1 to fit the experimental results for all rods. The results of fitting can be seen in Fig. 8.2. A good match is obtained. The match is considered good because the EMOC model is fully algebraic, has no ODE solution, uses no detailed frequency information, and still captures trends qualitatively with just three parameters.

Figure 8.3 shows the fit only for the 600 mm rod when we include one axial mode, with all fitted parameters the same as in Fig. 8.2. It is seen that the fit worsens when an axial mode is included and the rod is near vertical. The fit worsens upon retaining more axial modes.

8.3 Concluding remarks

In this chapter, we have applied the EMOC model to the experimentally obtained restitution values for rods dropped on an immovable surface, at different angles of inclination, as presented in [19]. We formulated the equations of motion and showed the necessary changes to be made to the EMOC formulation for this tilted rod problem. On fitting, we observed that our model is inappropriate for near vertical impacts where axial modes dominate, because the longitudinal impact of a slender uniform rod has special restitution properties [46]. The axial natural frequencies are commensurate, and there is an unexpectedly high restitution which the EMOC cannot capture. Thus, we retained only the first few lateral modes and obtained a good fit.

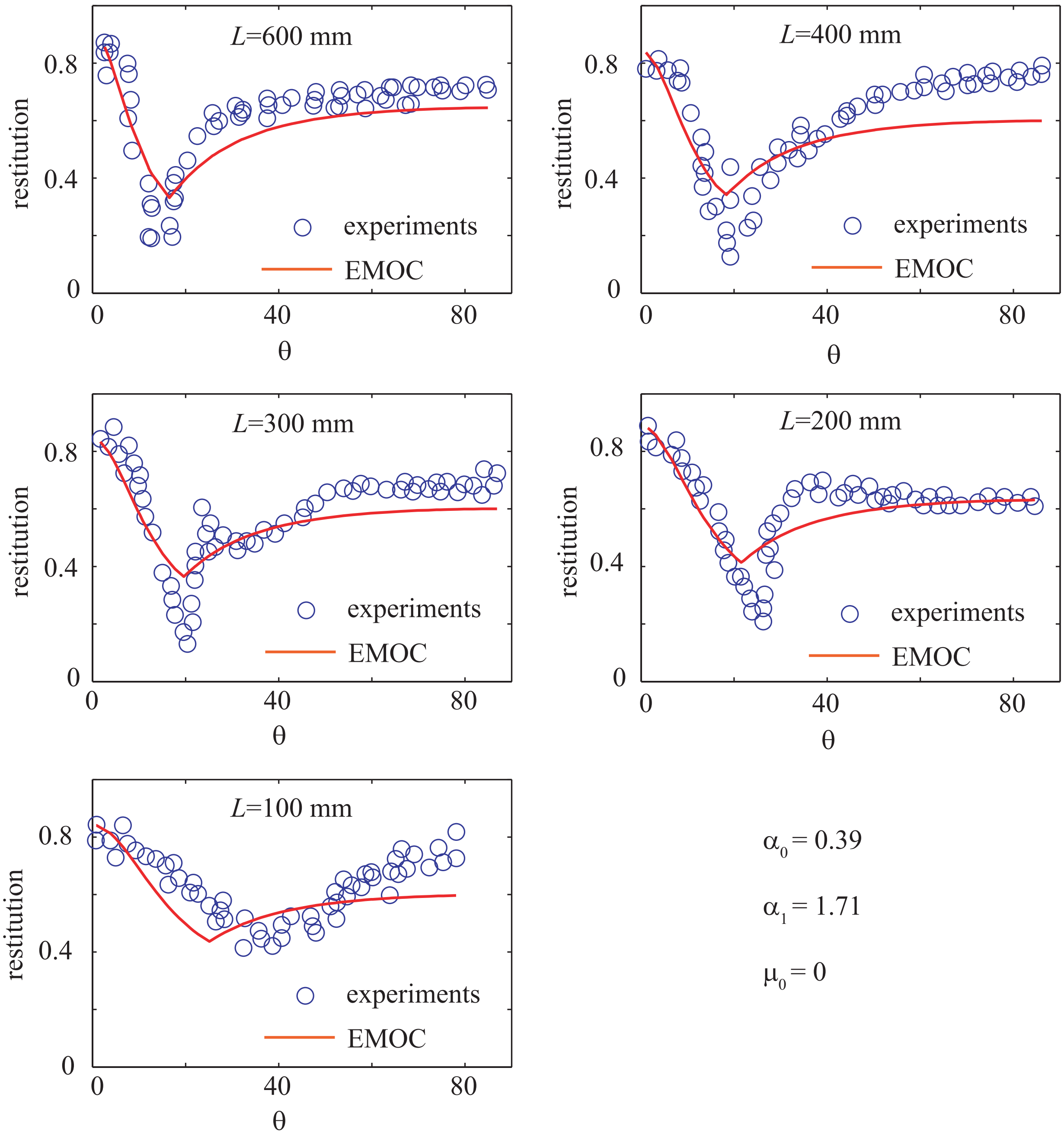

Figure 8.2: The achieved fit for restitution for different angle of inclinations and for different rod lengths. N_l used in the simulations: subplots (i) 7 (ii) 5 (iii) 4 (iv) 3 (v) 2.

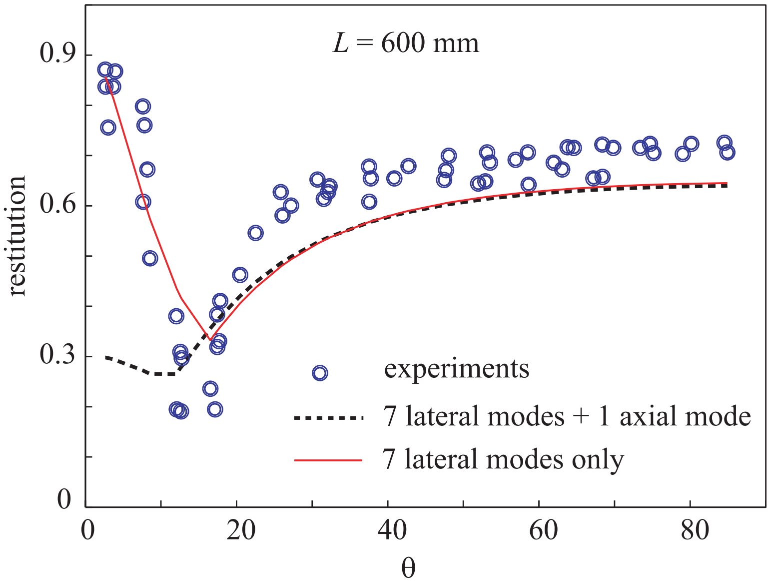

Figure 8.3: The fit for different angles of inclination for rod length 600 mm. Only one axial mode lowers the predicted restitution value. Recall subsection 8.2.1. This is why axial modes were dropped.

Chapter 9

Conclusions

This thesis has examined, and presented new approximations, for vibration-dominated impacts between a compact body and a flexible vibrating beam. A novel restitution modeling approach developed in this thesis has also been tested on experimental data for tilted rods dropped on an immovable surface, from Stoianovici and Hurmuzlu [19].

The first problem studied in the thesis (chapter 2) is the idealized limiting case of a Hertzian sphere striking an infinitely long Euler-Bernoulli beam initially at rest. In this problem, waves radiate away from the point of contact but no waves ever get reflected back. A modal expansion solution is not possible. The impulse response at a point of an infinite beam is known to be proportional to the square root of time. So, the governing equation for the interaction can be written using a nonlinear ODE with a fractional derivative term. Using existing routines, we solve the governing equations. The dynamic behavior of the contact-impact problem is completely characterized by using a single nondimensional number S. It was demonstrated that high S need not imply high severity of contact stress. When S is sufficiently low there is just one contact phase followed by separation. Beyond $S \approx 1.56$ the eventual fate is sustained contact, but multiple separation events can occur. For sufficiently large S, no separation occurs and sustained contact occurs with decaying oscillations. A complete numerical characterization of the entire behavior is given. In addition, a semi-analytical solution for the first contact phase is given. Finally, an asymptotic description of the motion of the impactor (or the contact point) for large time is given for such situations where the final state is sustained contact. That final asymptotic description is independent of the number of intervening separations. These foregoing results for the ball and infinite beam impact-contact are new.

After the infinite beam problem, impact with a finite beam is taken up. Since the beam is finite, a modal expansion solution can be attempted and is implemented. It is found numerically that the restitution value converges very slowly for impacts of reasonable sphere sizes, even though the Hertz contact means that the contact is technically “soft”. A detailed numerical study in chapter 3 demonstrates that a small amount of modal damping regularizes the impact, and the number of modes required to obtain a reasonably accurate value of restitution decreases from more than 60 to around 25, for a simply-supported beam. Additionally, it is seen that contact dissipation plays almost no role, and modal damping helps only when there are multiple subimpacts. For single-contact impacts, small damping plays a negligible role in all cases.

Having established that light modal damping can regularize the impact, a detailed numerical study is taken up of restitution for many different ball sizes, at many different contact locations, for four different beams with different boundary conditions. Those numerical results are presented in chapter 4. These results serve as a data set for the subsequent modeling effort in this thesis.

Over chapters 5 and 6, we present the main academic contribution of the thesis, which is a new way of approximately modeling restitution in such vibration-dominated impacts. This approach has been named Energy Minimization under Outward Constraints (EMOC), and is a new modeling philosophy for such modeling impacts. The idea is that since the impact is complicated and there are multiple impacts, simple yet accurate models are not likely to be found. However, some fundamental constraints on the impact outcome are known (noninterpenetration, nonnegative normal impulse). Those constraints are either linear equality constraints or linear inequality constraints. There is one other physical quantity of interest, namely the final kinetic energy of the system, which is a quadratic function of the unknowns. This quadratic function should not be allowed to increase in the predicted impact outcome because that violates physical principles. A modeling approach that therefore suggests itself is to minimize this kinetic energy subject to the constraints that are available as mentioned above. Such an approach can be easily implemented using quadratic programming. Consequently, the model will also be easy to implement using existing routines, e.g., in Matlab. However, if such an approach is implemented directly the impact will turn out to have very poor rebound. Extending the work of Rakshit and Chatterjee [18] for rigid body simultaneous multiple impacts, here two new and additional outward constraints are posed and incorporated. The form of the outward constraint is a modeling exercise and a successful proposal for the same has been presented in this thesis. In summary, a principle of energy minimization subject to fundamental physical constraints and the *new* outward constraints leads to a novel quadratic program based model, the solution of which gives a candidate impact outcome.

The EMOC model is parameterized using three free parameters described in chapter 7. For any choice of those parameters, a physically reasonable outcome will always be predicted. Impossibilities are never predicted. Moreover, when we fit the model to the earlier numerically obtained data for ball and beam impacts, a good overall fit is obtained. Three parameters are fitted for each beam, for a variety of ball sizes and impact locations.

In chapter 8, a completely different problem is taken up, and the EMOC approach is tested on this problem. Now, the experiments of Stoianovici and Hurmuzlu [19] are considered, where tilted rods were dropped on a rigid immovable surface. A detailed mechanistic model was presented by those authors and a system specific restitution model was developed in [14]. However, here we wish to take our less-mechanistic algebraic impact model and see how it can be applied to their physical problem. On writing the equations of motion, it is seen that the structure of the equations is similar to that of the ball-beam impacts. Thus, we are able to test the EMOC model on these impacts.

It is found that incorporation or activation of the axial beam modes makes the EMOC model inappropriate for the falling rod problem, because for a rod in axial vibration all the natural frequencies are commensurate and on rebound, the rods retain no vibration effects. Observing this difficulty, as an ad hoc criterion, only lateral modes were retained. It was ensured that the natural frequency of the highest lateral mode retained was lower than the frequency of the first axial mode of the rod. Subsequently, for three parameters fitted globally, a reasonable fit was obtained for the impact outcomes for the rods of five different lengths and all the inclinations.

Before we conclude, we remark on two aspects of the EMOC model that can be envisaged in future work.

One is the application of the EMOC model to real and complicated structures. In such cases, instead of a theoretical or computational modal analysis, experimental modal tests on the structure at different locations can be done to determine the natural frequencies and the associated mode shapes. After those are found, on dropping balls at different locations, it can seen if the model makes a reasonable prediction. We believe that even if we are able to predict the restitution within ±0.1 in a range from 0 to 1, there is no comparable effort in the existing vibroimpact literature. An experimental study with modal testing at different locations is envisaged in future work.

Another comment relevant here is that, so far the EMOC model considers only transverse impact. In the case of an oblique impact, if there is no friction then there is no difference as the tangential motion of the ball does not couple with the normal motion. However, in the presence of friction, to the extent that the lateral deformation and the normal deformation of the ball or the beam may couple, or to the extent that the presence of tangential tractions may excite vibrations of the beam, there may be a difference. If the coefficient of friction is very high, then there may be a strong tangential impulse and if the slope of the beam is significantly different from zero during the application of the tangential impulse, there will actually be a net downward component. Such nonlinear interactions may be taken up in future work.

In summary, in this thesis, three fundamentally different types of impacts have been studied and new approximations have been presented for them. The first is a Hertzian sphere on an infinite beam, the second is a Hertzian sphere on finite beams with different boundary conditions, and the third is a tilted rod falling on an immovable surface. The latter two problems were modeled using the new EMOC approach with good results. It is hoped that the EMOC modeling approach will be found interesting both for its academic novelty as well as its possible utility in multi-body dynamic environments, games, and multi-physics simulations where a quick solution is required in the presence of complicated dynamics.

Appendix A

Appendix

A.1 Numerical recipe for fractional DE

This appendix is relevant to chapter 2.

The numerical recipe of [69] extends the work of [67], which was independently developed but rather similar to [66]. A brief introduction to the recipe follows for completeness.

We denote fractional derivatives as $\mathrm{D}^\alpha y$ where $n-1 < \alpha < n$, and n is a positive integer. Two common definitions of the fractional derivative are: Riemann-Liouville definition

$$\mathrm{D}^\alpha x(t) = \frac{1}{\Gamma(n-\alpha)} \left(\frac{\mathrm{d}}{\mathrm{d}t}\right)^n \int_{t_o}^{t} \frac{x(\tau)}{(t-\tau)^{(\alpha-n+1)}} \mathrm{d}\tau,$$

and Caputo definition

$$\mathrm{D}^\alpha x(t) = \frac{1}{\Gamma(n-\alpha)} \int_{t_o}^{t} \frac{x^{(n)}(\tau)}{(t-\tau)^{(\alpha-n+1)}} \mathrm{d}\tau,$$

and we usually assign $t_0 = 0$. In our problem, we assume zero initial conditions, for which the above two definitions are equivalent.

This numerical recipe uses three α dependent matrices $\mathbf{A}_{N\times N}$, $\mathbf{B}_{N\times N}$ and $\mathbf{c}_{N\times 1}$, where N represents the number of internal states used to approximate the fractional derivative. In what follows, we will drop the size-denoting subscripts and simply write $\mathbf{A}$, $\mathbf{B}$ and $\mathbf{c}$.

Matlab code from [69] is used to compute these matrices given α, N and a frequency range of interest (controlled using two parameters β_1 and β_2 in the Matlab code of [69]).

Given these matrices, if we solve the system of ODEs

$$\mathbf{A}\dot{\mathbf{a}} + \mathbf{B}\mathbf{a} = \mathbf{c}\frac{\mathrm{d}^n x}{\mathrm{d}t^n}, \quad \text{with initial conditions} \quad \mathbf{a}(0) = 0, \tag{A.1}$$

then, to an excellent numerical approximation,

$$\mathbf{c}^T\mathbf{a} \approx \mathrm{D}^\alpha x,$$

where x is the primary variable of interest and $\mathbf{a}_N$ is a vector of internal variables used to approximate the fractional derivative (for related discussion, see [85]).

We have used $\mathbf{A}$, $\mathbf{B}$ and $\mathbf{c}$ for $\alpha = 0.5$ and $N = 50$. The equations that are numerically solved are

$$\begin{aligned} \mathbf{A}\dot{\mathbf{a}} + \mathbf{B}\mathbf{a} &= \mathbf{c}\ddot{y}, \\ \epsilon\ddot{y} + \mathbf{c}^T\mathbf{a} &= -\frac{\sqrt{\pi}}{2}\overline{C}\, f, \\ \ddot{z} &= \frac{F}{m}, \end{aligned} \tag{A.2}$$

where

$$F = k_H \left\langle y - z \right\rangle^{\frac{3}{2}},$$

and where ϵ is a small regularization parameter (see [69]). We have used $\epsilon = 1 \times 10^{-8}$.

The graphs of chapter 2 were generated after careful convergence checks. In simulations, the parameters and error tolerances were repeatedly adjusted for large ranges of the solution regimes, and it was ensured that every graph plotted was significantly more accurate than plotting accuracy. In particular, convergence studies were done with the number of elements used in the discretization of the fractional order derivative; convergence studies were done using “abstol” and “reltol” settings in the ODE solver in Matlab; and finally whenever solutions for a particular S were plotted next to solutions where the parameters were scaled differently by dimensional analysis, the magnitude of the mismatch was checked and it was ensured that is extremely small in all places.

Numerically, solution requires more care when multiple impacts occur (seven or more). It was seen that f decreases roughly exponentially for later subimpacts. The contact duration increases roughly exponentially as well. As such, we chose the force scaling term as about $\hat{F} = 7$ in Eq. 2.50 (number of subimpacts) and $\hat{T} = -2$ for overall shorter simulation time. We also modified the frequency range of interest parameter in the numerical recipe; we used $\beta_1 = -2.4$ and $\beta_2 = 1.2$ for all the numerical simulations, except for $1.56 \lesssim S \lesssim 2.12$, where we varied β_1 from $(-2.4, -3.5)$ and β_2 from $(1.2, 2)$ depending on the S value.

A.2 Nondimensionalization example

This appendix is relevant to chapter 2.

We consider three sets of parameters, given in Table A.1. For each set, $S = 0.528$. The scaling constants ($\hat{F}$, $\hat{T}$) for each set are also given.

We simulate the system for parameter sets 1 and 2. The dimensional contact force is plotted against the dimensional time; see Fig. A.1(a) for parameter set 1, and subplot (b) for set 2. The graph of nondimensionalized contact force versus nondimensionalized time, for both parameter sets, is the same: see subplot (c).

Table A.1: Representative system parameters for $S = 0.528$. The first two rows give the results shown in Figure A.1. The third row shows parameter values obtained from Eqs. (2.48) through (2.51) for the same S.

Set	$\overline{C}$	k_H	m	v	$\hat{F}$	$\hat{T}$	S
1.	0.0279	1.6481	97.43	0.0838	$\hat{F}_1 = 1.105$	$\hat{T}_1 = 7.389$	$S_1 = 0.528$
2.	0.30	5.0	2.0	13.9715	$\hat{F}_2 = 77.62$	$\hat{T}_2 = 0.36$	$S_2 = 0.528$
3.	0.8082	1.0	1.2372	0.8082	$\hat{F}_3 = 1$	$\hat{T}_3 = 1$	$S_3 = 0.528$

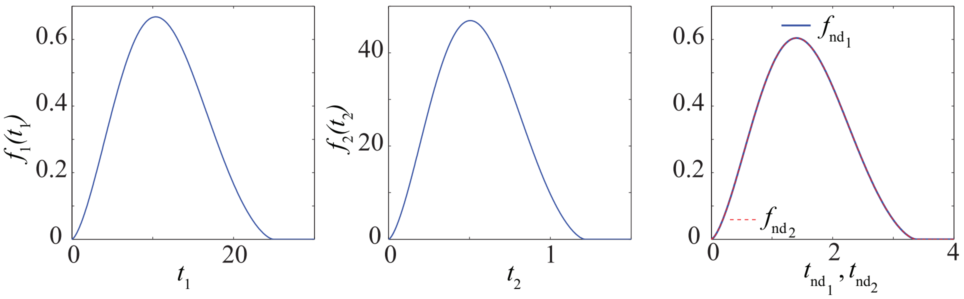

(a) (b) (c)

Figure A.1: f against t for two sets of parameters each having $S = 0.528$; see numerical values of the parameters in Table A.1. Subplot (a) dimensional $f_1(t_1)$ for parameters given in the first row. (b) dimensional $f_2(t_2)$, second row. (c) the overlapping nondimensionalized force against nondimensionalized time computed from subplots (a) and (b).

A.3 Modal energies for damped and undamped beam

Figure A.2 compares the total energy (kinetic and potential) for each mode for an undamped and a damped simply supported beam. The left hand side graphs are with no damping whereas the right hand side graphs are with $\zeta = 0.02$. Other simulation parameters are: $b = 0.618\ldots$, $m = 0.1103$ and $N = 40$. The jumps in the energies correspond the contact phases. It is seen that the higher modes damp out more quickly for the damped beam.

A.4 Simulation of ball-beam impact using the FEM

Here we simulate the ball-beam impact using the Finite Element Method (FEM). We compare the solutions obtained using earlier modal analysis in chapters 3 and 4, against those obtained now by the FEM. We use Matlab for the FEM simulation.

We consider only the uniform cantilever beam. The ball has mass $m = 0.608$. The beam is discretized into beam elements, where each node has two degrees of freedom (a transverse displacement and a rotation). We drop degrees of freedom of the first node (fixed end). For uniformity, we use 20 elements (because earlier we had used $N = 40$ modes). The discretized beam, therefore, has 21 nodes and 40 degrees of freedom.

We assume for simplicity that impact occurs exactly at a node. The contact force is then a nodal force. We assume Hertz contact as earlier. The system parameters are kept

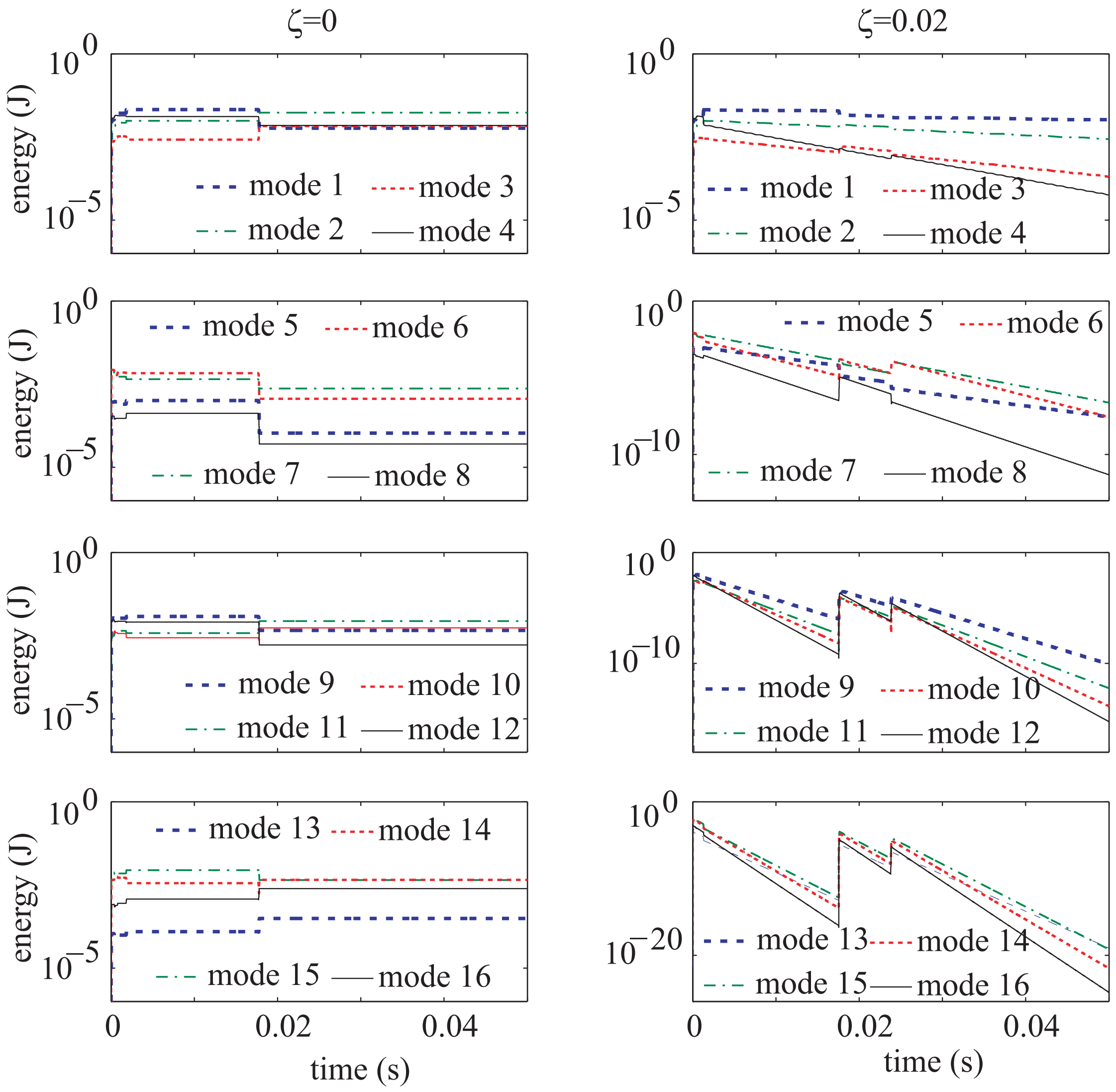

Figure A.2: Modal energies for a damped and an undamped pinned-pinned beam. $b = 0.618\ldots$. At time very close to zero, the energy goes from zero to nonzero values and on logarithmic scale there is a very rapid variation which is not shown in the graphs.

the same as earlier.

The discretization of the beam results in a system of ODEs governing evolution of the nodal degrees of freedom. We thus have 21 second-order ODEs for the ball-beam system. The initial conditions are kept the same as earlier: the nodal degrees of freedom all start with zero initial conditions, the ball starts at $z = 0$ and with $\dot{z} = -1$. Matlab's "ode15s" is used to numerically integrate the system of ODEs. We have 21 possible impact locations, spread uniformly between 0 and 1 (we ignore $b = 0$). We determine the restitution values using both FEM and modal decomposition at all these 21 impact locations.

Figure A.3 compares the restitution values obtained using modal analysis and the FEM. A good match is seen. However, it is mentioned that in other simulations when the rebound was much smaller, e.g. 0.1, the mismatch was a bit larger as discussed earlier in the main text of the thesis.

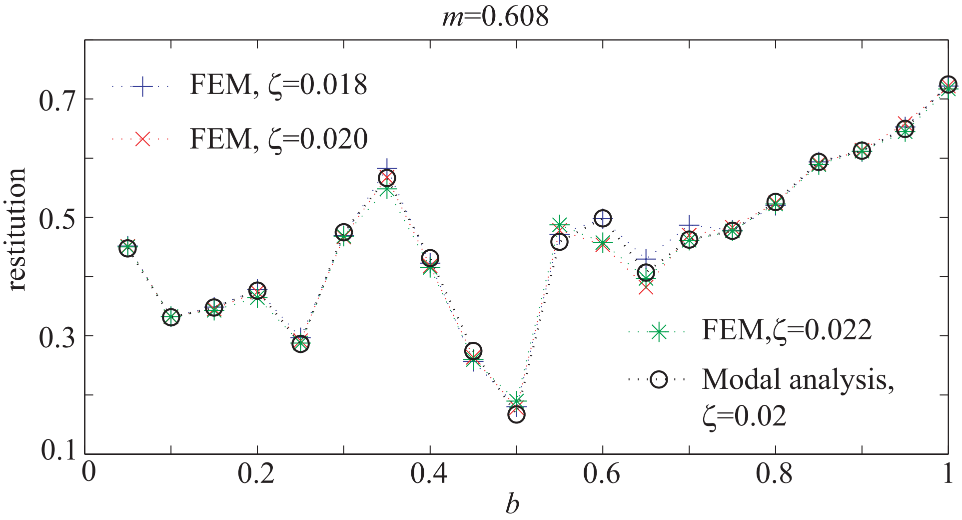

Figure A.3: Restitution values obtained using modal analysis and FEM for the cantilever beam.

A.5 Data extraction of tilted rods experiments

Data was extracted manually from an electronic version of the following graphic, Fig. A.4.

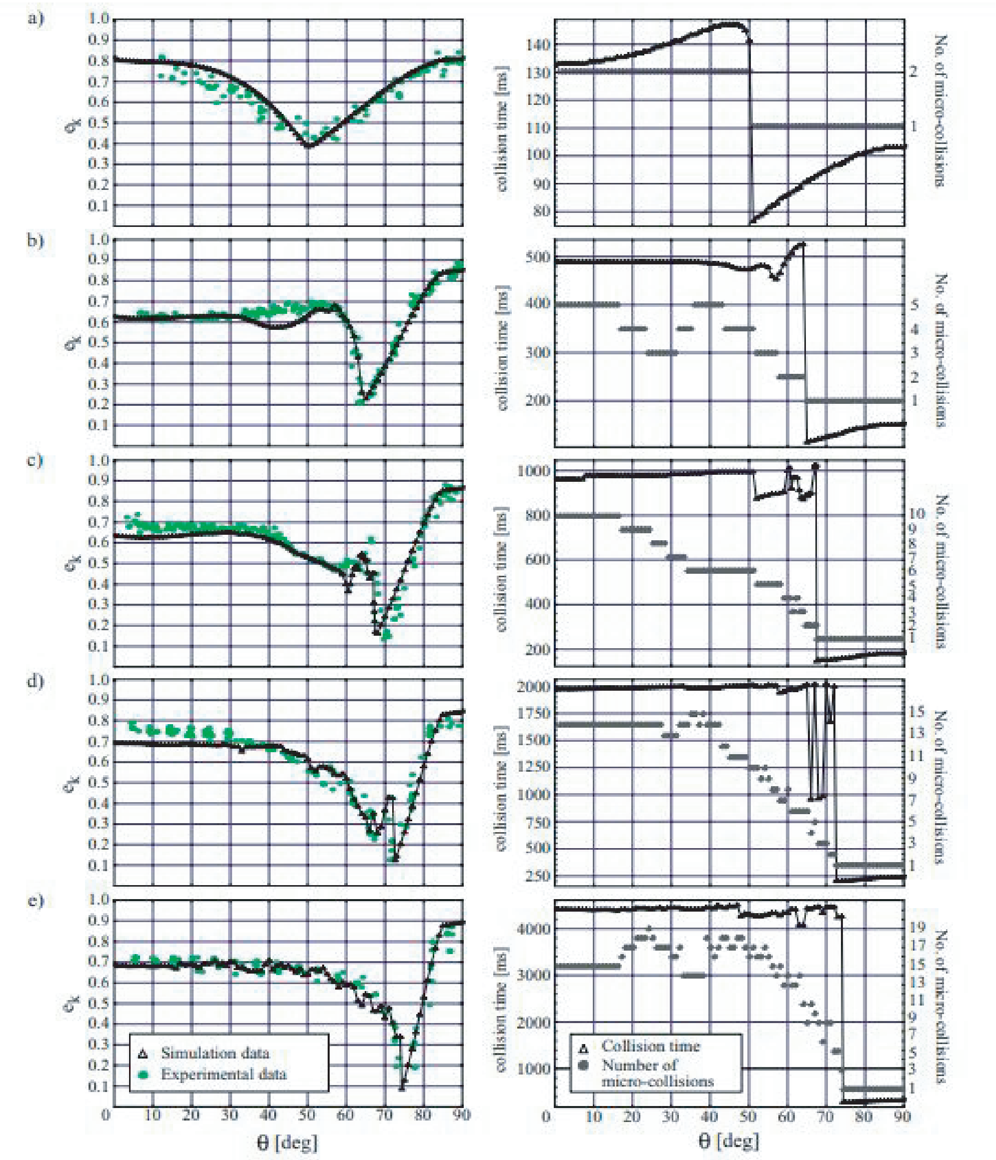

Figure A.4: Screenshot of Fig. 5 in the article by Stoianovici and Hurmuzlu, 1996 adapted/scaled slightly. These are the experimentally obtained restitution values for dropped rods of different lengths at different angles of inclination. The rod lengths are (a) 600 mm, (b) 400 mm, (c) 300 mm, (d) 200 mm and (e) 100 mm. We fit our EMOC model to these experimental outcomes, see chapter 8.

Bibliography

[1] W. Goldsmith, *Impact: The theory and physical behavior of colliding solids.* Edward Arnold, 1960.

[2] F. Pfeiffer and C. Glocker, *Multibody dynamics with unilateral contacts.* John Wiley & Sons, 1996.

[3] W. J. Stronge, *Impact mechanics.* Cambridge University Press, 2000.

[4] B. Brogliato, *Nonsmooth mechanics: Models, dynamics and control.* Springer, 2016.

[5] A. Chatterjee, *Rigid body collisions: some general considerations, new collision laws, and some experimental data.* Cornell University Ithaca, NY, 1997.

[6] Y. A. Khulief and A. A. Shabana, "Dynamic analysis of constrained system of rigid and flexible bodies with intermittent motion," *Journal of Mechanisms, Transmissions, and Automation in Design*, vol. 108, no. 1, pp. 38–45, 1986.

[7] Y. A. Khulief, "Modeling of impact in multibody systems: an overview," *Journal of Computational and Nonlinear Dynamics*, vol. 8, no. 2, p. 021012, 2013.

[8] P. Lötstedt, "Mechanical systems of rigid bodies subject to unilateral constraints," *SIAM Journal on Applied Mathematics*, vol. 42, no. 2, pp. 281–296, 1982.

[9] D. E. Stewart, "Rigid-body dynamics with friction and impact," *SIAM Review*, vol. 42, no. 1, pp. 3–39, 2000.

[10] A. Chatterjee and A. Ruina, "Two interpretations of rigidity in rigid-body collisions," *Journal of Applied Mechanics*, vol. 65, no. 4, pp. 894–900, 1998.

[11] S. Goyal, E. N. Pinson, and F. W. Sinden, "Simulation of dynamics of interacting rigid bodies including friction I: general problem and contact model," *Engineering with Computers*, vol. 10, no. 3, pp. 162–174, 1994.

[12] A. S. Yigit, A. G. Ulsoy, and R. A. Scott, "Dynamics of a radially rotating beam with impact, part 1: theoretical and computational model," *Journal of Vibration and Acoustics*, vol. 112, no. 1, pp. 65–70, 1990.

[13] A. S. Yigit and A. P. Christoforou, “The efficacy of the momentum balance method in transverse impact problems,” *Journal of Vibration and Acoustics*, vol. 120, no. 1, pp. 47–53, 1998.

[14] Y. Hurmuzlu, “An energy-based coefficient of restitution for planar impacts of slender bars with massive external surfaces,” *Journal of Applied Mechanics*, vol. 65, no. 4, pp. 952–962, 1998.

[15] A. P. Ivanov, “On multiple impact,” *Journal of Applied Mathematics and Mechanics*, vol. 59, no. 6, pp. 887–902, 1995.

[16] M. Anitescu and F. A. Potra, “Formulating dynamic multi-rigid-body contact problems with friction as solvable linear complementarity problems,” *Nonlinear Dynamics*, vol. 14, no. 3, pp. 231–247, 1997.

[17] C. Liu, Z. Zhao, and B. Brogliato, “Frictionless multiple impacts in multibody systems. I. theoretical framework,” *Proceedings of the Royal Society of London A: Mathematical, Physical and Engineering Sciences*, vol. 464, no. 2100, pp. 3193–3211, 2008.

[18] S. Rakshit and A. Chatterjee, “Scalar generalization of Newtonian restitution for simultaneous impact,” *International Journal of Mechanical Sciences*, vol. 103, pp. 141–157, 2015.

[19] D. Stoianovici and Y. Hurmuzlu, “A critical study of the applicability of rigid-body collision theory,” *Journal of Applied Mechanics*, vol. 63, no. 2, pp. 307–316, 1996.

[20] S. C. Hunter, “Energy absorbed by elastic waves during impact,” *Journal of the Mechanics and Physics of Solids*, vol. 5, no. 3, pp. 162–171, 1957.

[21] J. Reed, “Energy losses due to elastic wave propagation during an elastic impact,” *Journal of Physics D: Applied Physics*, vol. 18, no. 12, pp. 2329–2337, 1985.

[22] C. Zener, “The intrinsic inelasticity of large plates,” *Physical Review*, vol. 59, no. 8, p. 669, 1941.

[23] A. S. Yigit and A. P. Christoforou, “Impact dynamics of composite beams,” *Composite Structures*, vol. 32, no. 1-4, pp. 187–195, 1995.

[24] A. Bhattacharjee and A. Chatterjee, “Transverse impact of a Hertzian body with an infinitely long Euler-Bernoulli beam,” *Journal of Sound and Vibration*, vol. 429, pp. 147–161, 2018.

[25] K. H. Hunt and F. R. E. Crossley, “Coefficient of restitution interpreted as damping in vibroimpact,” *Journal of Applied Mechanics*, vol. 42, no. 2, pp. 440–445, 1975.

[26] A. P. Christoforou and A. S. Yigit, “Effect of flexibility on low velocity impact response,” *Journal of Sound and Vibration*, vol. 217, no. 3, pp. 563–578, 1998.

[27] Y. A. Rossikhin and M. V. Shitikova, “Two approaches for studying the impact response of viscoelastic engineering systems: an overview,” *Computers & Mathematics with Applications*, vol. 66, no. 5, pp. 755–773, 2013.

[28] H. M. Lankarani and P. E. Nikravesh, “Continuous contact force models for impact analysis in multibody systems,” *Nonlinear Dynamics*, vol. 5, no. 2, pp. 193–207, 1994.

[29] R. Seifried, W. Schiehlen, and P. Eberhard, “Numerical and experimental evaluation of the coefficient of restitution for repeated impacts,” *International Journal of Impact Engineering*, vol. 32, no. 1-4, pp. 508–524, 2005.

[30] S. J. Singh and A. Chatterjee, “Nonintrusive measurement of contact forces during vibration dominated impacts,” *Journal of Dynamic Systems, Measurement, and Control*, vol. 126, no. 3, pp. 489–497, 2004.

[31] G. C. McLaskey and S. D. Glaser, “Hertzian impact: experimental study of the force pulse and resulting stress waves,” *The Journal of the Acoustical Society of America*, vol. 128, no. 3, pp. 1087–1096, 2010.

[32] T. Belytschko and M. O. Neal, “Contact-impact by the pinball algorithm with penalty and Lagrangian methods,” *International Journal for Numerical Methods in Engineering*, vol. 31, no. 3, pp. 547–572, 1991.

[33] P. Flores and J. Ambrósio, “On the contact detection for contact-impact analysis in multibody systems,” *Multibody System Dynamics*, vol. 24, no. 1, pp. 103–122, 2010.

[34] S. Ebrahimi and P. Eberhard, “A linear complementarity formulation on position level for frictionless impact of planar deformable bodies,” *ZAMM-Journal of Applied Mathematics and Mechanics/Zeitschrift für Angewandte Mathematik und Mechanik*, vol. 86, no. 10, pp. 807–817, 2006.

[35] A. B. Nordmark, “Non-periodic motion caused by grazing incidence in an impact oscillator,” *Journal of Sound and Vibration*, vol. 145, no. 2, pp. 279–297, 1991.

[36] J. Ing, E. Pavlovskaia, M. Wiercigroch, and S. Banerjee, “Experimental study of impact oscillator with one-sided elastic constraint,” *Philosophical Transactions of the Royal Society A: Mathematical, Physical and Engineering Sciences*, vol. 366, no. 1866, pp. 679–705, 2007.

[37] H. Palas, W. C. Hsu, and A. A. Shabana, “On the use of momentum balance and the assumed modes method in transverse impact problems,” *Journal of Vibration and Acoustics*, vol. 114, no. 3, pp. 364–373, 1992.

[38] J. L. Escalona, J. R. Sany, and A. A. Shabana, “On the use of the restitution condition in flexible body dynamics,” *Nonlinear Dynamics*, vol. 30, no. 1, pp. 71–86, 2002.

[39] R. Seifried, W. Schiehlen, and P. Eberhard, “The role of the coefficient of restitution on impact problems in multi-body dynamics,” *Proceedings of the Institution of Mechanical Engineers, Part K: Journal of Multi-body Dynamics*, vol. 224, no. 3, pp. 279–306, 2010.

[40] T. K. Uchida, M. A. Sherman, and S. L. Delp, “Making a meaningful impact: modelling simultaneous frictional collisions in spatial multibody systems,” *Proceedings of the Royal Society A: Mathematical, Physical and Engineering Sciences*, vol. 471, no. 2177, p. 20140859, 2015.

[41] P. Flores, R. Leine, and C. Glocker, “Application of the nonsmooth dynamics approach to model and analysis of the contact-impact events in cam-follower systems,” *Nonlinear Dynamics*, vol. 69, no. 4, pp. 2117–2133, 2012.

[42] Y. Khulief and A. Shabana, “A continuous force model for the impact analysis of flexible multibody systems,” *Mechanism and Machine Theory*, vol. 22, no. 3, pp. 213–224, 1987.

[43] P. Flores, J. Ambrósio, J. P. Claro, and H. Lankarani, “Influence of the contact—impact force model on the dynamic response of multi-body systems,” *Proceedings of the Institution of Mechanical Engineers, Part K: Journal of Multi-body Dynamics*, vol. 220, no. 1, pp. 21–34, 2006.

[44] M. Machado, P. Moreira, P. Flores, and H. M. Lankarani, “Compliant contact force models in multibody dynamics: Evolution of the hertz contact theory,” *Mechanism and Machine Theory*, vol. 53, pp. 99–121, 2012.

[45] M. Liao, Y. Liu, J. P. Chávez, A. S. Chong, and M. Wiercigroch, “Dynamics of vibro-impact drilling with linear and nonlinear rock models,” *International Journal of Mechanical Sciences*, vol. 146, pp. 200–210, 2018.

[46] E. J. Routh, *Dynamics of a system of rigid bodies.* Dover New York, 1955.

[47] C. Liu, Z. Zhao, and B. Brogliato, “Frictionless multiple impacts in multibody systems. I. theoretical framework,” *Proceedings of the Royal Society of London A: Mathematical, Physical and Engineering Sciences*, vol. 464, no. 2100, pp. 3193–3211, 2008.

[48] J. Keller, “Impact with friction,” *Journal of applied Mechanics*, vol. 53, no. 1, pp. 1–4, 1986.

[49] J. Batlle and S. Cardona, “The jamb (self-locking) process in three-dimensional collisions,” *Journal of applied mechanics*, vol. 65, no. 2, pp. 417–423, 1998.

[50] O. K. Ajibose, M. Wiercigroch, E. Pavlovskaia, and A. R. Akisanya, "Global and local dynamics of drifting oscillator for different contact force models," *International Journal of Non-Linear Mechanics*, vol. 45, no. 9, pp. 850–858, 2010.

[51] D. W. Marhefka and D. E. Orin, "A compliant contact model with nonlinear damping for simulation of robotic systems," *IEEE Transactions on Systems, Man, and Cybernetics-Part A: Systems and Humans*, vol. 29, no. 6, pp. 566–572, 1999.

[52] P. Flores and J. Ambrósio, "Revolute joints with clearance in multibody systems," *Computers & structures*, vol. 82, no. 17-19, pp. 1359–1369, 2004.

[53] A. Chatterjee and A. Ruina, "A new algebraic rigid-body collision law based on impulse space considerations," *Journal of Applied Mechanics*, vol. 65, no. 4, pp. 939–951, 1998.

[54] D. E. Stewart and J. C. Trinkle, "An implicit time-stepping scheme for rigid body dynamics with inelastic collisions and coulomb friction," *International Journal for Numerical Methods in Engineering*, vol. 39, no. 15, pp. 2673–2691, 1996.

[55] C. E. Smith, "Predicting rebounds using rigid-body dynamics," *Journal of Applied Mechanics*, vol. 58, no. 3, pp. 754–758, 1991.

[56] A. Bhattacharjee and A. Chatterjee, "Interplay between dissipation and modal truncation in ball-beam impact," *Journal of Computational and Nonlinear Dynamics*, vol. 12, no. 6, p. 061018, 2017.

[57] C. V. Raman, "On some applications of Hertz's theory of impact," *Physical Review*, vol. 15, no. 4, p. 277, 1920.

[58] H. Schwieger, "A simple calculation of the transverse impact on beams and its experimental verification," *Experimental Mechanics*, vol. 5, no. 11, pp. 378–384, 1965.

[59] S. P. Timoshenko, "Zur frage nach der wirkung eines stosses auf einen balken," *Zeitschrift für Mathematik und Physik*, vol. 62, no. 2, pp. 198–209, 1913.

[60] H. Schwieger, "Central deflection of a transversely struck beam," *Experimental Mechanics*, vol. 10, no. 4, pp. 166–169, 1970.

[61] J. F. Doyle, "An experimental method for determining the dynamic contact law," *Experimental Mechanics*, vol. 24, no. 1, pp. 10–16, 1984.

[62] R. K. Mittal, "A closed form solution for the response of a long elastic beam to dynamic loading," *Ingenieur-Archiv*, vol. 60, no. 1, pp. 41–50, 1989.

[63] A. Chatterjee, "The short-time impulse response of Euler-Bernoulli beams," *Journal of Applied Mechanics*, vol. 71, no. 2, pp. 208–218, 2004.

[64] J. Meijaard, “Lateral impacts on flexible beams in multibody dynamics simulations,” in *IUTAM Symposium on Multiscale Problems in Multibody System Contacts*, pp. 173–182, Springer, 2007.

[65] K. L. Johnson, *Contact mechanics.* Cambridge University Press, 1987.

[66] L. Yuan and O. P. Agrawal, “A numerical scheme for dynamic systems containing fractional derivatives,” *Journal of Vibration and Acoustics*, vol. 124, no. 2, pp. 321–324, 2002.

[67] S. J. Singh and A. Chatterjee, “Galerkin projections and finite elements for fractional order derivatives,” *Nonlinear Dynamics*, vol. 45, no. 1-2, pp. 183–206, 2006.

[68] I. Podlubny, A. Chechkin, T. Skovranek, Y. Chen, and B. M. V. Jara, “Matrix approach to discrete fractional calculus II: partial fractional differential equations,” *Journal of Computational Physics*, vol. 228, no. 8, pp. 3137–3153, 2009.

[69] S. Das and A. Chatterjee, “Simple recipe for accurate solution of fractional order equations,” *Journal of Computational and Nonlinear Dynamics*, vol. 8, no. 3, p. 031007, 2013.

[70] J. Ahn and D. E. Stewart, “Existence of solutions for a class of impact problems without viscosity,” *SIAM Journal on Mathematical Analysis*, vol. 38, no. 1, pp. 37–63, 2006.

[71] A. S. Yigit, A. G. Ulsoy, and R. A. Scott, “Spring-dashpot models for the dynamics of a radially rotating beam with impact,” *Journal of Sound and Vibration*, vol. 142, no. 3, pp. 515–525, 1990.

[72] S. Pashah, M. Massenzio, and E. Jacquelin, “Prediction of structural response for low velocity impact,” *International Journal of Impact Engineering*, vol. 35, no. 2, pp. 119–132, 2008.

[73] D. J. Wagg, “A note on coefficient of restitution models including the effects of impact induced vibration,” *Journal of Sound and Vibration*, vol. 300, no. 3-5, pp. 1071–1078, 2007.

[74] B. J. Lazan, *Damping of materials and members in structural mechanics.* Pergamon Press, 1968.

[75] S. Biswas, P. Jana, and A. Chatterjee, “Hysteretic damping in an elastic body with frictional microcracks,” *International Journal of Mechanical Sciences*, vol. 108–109, pp. 61–71, 2016.

[76] X. Qi and X. Yin, "Experimental studying multi-impact phenomena exhibited during the collision of a sphere onto a steel beam," *Advances in Mechanical Engineering*, vol. 8, no. 9, pp. 1–16, 2016.

[77] "The most irrational number." `http://www.ams.org/samplings/feature-column/fcarc-irrational4`.

[78] R. Cross, "Impact of a ball with a bat or racket," *American Journal of Physics*, vol. 67, no. 8, pp. 692–702, 1999.

[79] A. Chatterjee, "On the realism of complementarity conditions in rigid body collisions," *Nonlinear Dynamics*, vol. 20, no. 2, pp. 159–168, 1999.

[80] E. Todorov, "A convex, smooth and invertible contact model for trajectory optimization," in *Robotics and Automation (ICRA), 2011 IEEE International Conference on*, pp. 1071–1076, IEEE, 2011.

[81] D. J. Segalman, A. M. Roy, and M. J. Starr, "Modal analysis to accommodate slap in linear structures," *Journal of Vibration and Acoustics*, vol. 128, no. 3, pp. 303–317, 2006.

[82] L. Demeio and S. Lenci, "Dynamic analysis of a ball bouncing on a flexible beam," *Journal of Sound and Vibration*, vol. 441, pp. 152–164, 2019.

[83] S. Boyd and L. Vandenberghe, *Convex optimization.* Cambridge University Press, 2004.

[84] Z. Dostál, *Optimal quadratic programming algorithms: with applications to variational inequalities.* Springer, 2009.

[85] A. Chatterjee, "Statistical origins of fractional derivatives in viscoelasticity," *Journal of Sound and Vibration*, vol. 284, no. 3-5, pp. 1239–1245, 2005.